

Laser Drilling of Wolfram Nozzle Plates and Characterization of Their Plasma-Generating Capabilities

Bachelorstudiengang Engineering Physics

Marvin Tammen
(Matrikel-Nr. 2280867)

January 27, 2016

Zur Erlangung des akademischen Grades

Bachelor of Engineering

Prüfer: Prof. Dr. habil. Ulrich Teubner

Zweitprüfer: Dr. Klaus Mann

Betreuer: Matthias Müller



Contents

1	Introduction	1
1.1	Motivation	1
1.2	Definition of Task	1
1.3	Outline	1
2	Theoretical Aspects	2
2.1	Laser–Target Interaction	2
2.1.1	Electron–Phonon and Electron–Electron Interaction	2
2.1.2	Localized Temperature Change	3
2.1.3	Surface Effects	4
2.2	Basics of Plasma Physics	5
2.2.1	Plasma Characteristics	5
2.2.2	Plasma Induction	7
2.2.3	Plasma Emission	8
2.3	Used Optical Methods	9
2.3.1	Schlieren Technique	9
2.3.2	Hartmann–Shack Sensor	10
3	Methods	11
3.1	Drilling	11
3.1.1	Percussion Drilling	11
3.1.2	Trepanning	13
3.2	Analysis	18
3.2.1	Topography	18
3.2.2	Schlieren Technique	19
3.2.3	Wavefront Distortion Measurement	21
3.2.4	Plasma Characteristics	22
4	Results	24
4.1	Effects of Various Parameters on Bore Geometry	25
4.1.1	Pulse Duration	25
4.1.2	Pulse Energy	26
4.1.3	Distance Between Focus and Rotational Axis	27
4.1.4	Pulse Count	29
4.1.5	Goniometer Table	32
4.2	Quality Assessment	33
4.2.1	Visual Bore Quality	33
4.2.2	Gas Flow Quality	38
4.2.3	Plasma Quality	46

5	Conclusion	48
6	Outlook	50
7	Acknowledgement	51
A	Appendix	55
A.1	Sony ICX285AL	55
A.2	Nozzle Data	56
A.3	Setup Photographs	64
A.4	Fabricated Part	68
A.5	Statement of Authorship	70

List of Figures

2.1	electron & lattice temperature dynamics	2
2.2	plasma emission spectrum	8
2.3	HARTMANN–SHACK principle	10
3.1	nozzle geometry	11
3.2	percussion drilling setup	12
3.3	dielectric mirror	13
3.4	trepanning: bore formation	13
3.5	trepanning setup	15
3.6	non-circular bore	17
3.7	beam cut-off	17
3.8	principle of confocal microscopy	18
3.9	Schlieren setup	19
3.10	Schlieren image at different knife edge positions	21
3.11	wavefront distortion measurement setup	21
3.12	plasma analysis setup	23
3.13	Ti filter transmission spectrum	23
3.14	filtered N plasma emission spectrum	24
4.1	bore crater	25
4.2	crater occurrence	26
4.3	influence of beam profile on ablation behavior	27
4.4	D vs. E	28
4.5	D vs. d	28
4.6	D vs. δ	30
4.7	bore depth vs. pulse count	32
4.8	maxium hole diameter vs. pulse count	33
4.9	percussion sample surface	34
4.10	trepanning process	35

4.11	trepanning example	36
4.12	trepanning: roundness impairment	36
4.13	cut-out cone	37
4.14	plate-cutting	38
4.15	nozzle data matrix	39
4.16	reference nozzle gas flow	41
4.17	nozzle (i) gas flow	41
4.18	nozzle (ii) gas flow	42
4.19	nozzle (iv) gas flow	43
4.20	nozzle (v) gas flow	44
4.21	nozzle (vi) gas flow	45
4.22	nozzle (vii) gas flow	46
A.1	ICX285AL data sheet	55
A.2	ICX285AL spectral sensitivity	56
A.3	nozzle (i)	57
A.4	nozzle (ii)	58
A.5	nozzle (iii)	59
A.6	nozzle (iv)	60
A.7	nozzle (v)	61
A.8	nozzle (vi)	62
A.9	nozzle (vii)	63
A.10	mounting v.1	64
A.11	trepanning setup photo	65
A.12	rotation device v.2	65
A.13	4f setup photo	66
A.14	plasma analysis setup photo	66
A.15	nozzle head	67
A.16	sketch of device for mounting the wolfram plates	69
A.17	photo of device for mounting the wolfram plates	70

List of Tables

1	reproducibility	18
2	nozzle data	40
3	relative nozzle data differences	40

Nomenclature

α	absorption coefficient
δ	distance between focus on workpiece surface and rotational axis
ϵ_0	permittivity of free space ($\approx 8.85 \cdot 10^{-12} \frac{\text{s}^4\text{A}^2}{\text{m}^3\text{kg}}$)
Γ	coupling parameter
γ	goniometer table angle
\hbar	reduced PLANCK constant ($\approx 1.05 \cdot 10^{-34} \text{ Js}$)
Λ	thermal penetration depth
λ	wavelength
λ_{De}	DEBYE length for electrons
λ_{Di}	DEBYE length for ions
$\langle \xi \rangle$	mean free path length
$\langle v \rangle$	most probable velocity, from MAXWELL–BOLTZMANN distribution
ν	frequency
ω	angular frequency
ω_p	plasma frequency
ρ	mass density
σ_i	electron–trapping cross section
τ	pulse length
θ	opening half angle
A_r	relative atomic mass
Cts	CCD counts
d	depositioning of the lens (defocus)
e	electron charge ($\approx 1.6 \cdot 10^{-19} \text{ C}$)
E_i	ion binding energy
E_{kin}	kinetic energy
E_{ph}	photon energy

f	focal length
f_{rep}	repetition rate
$FWHM$	full width half maximum
h	PLANCK constant ($\approx 6.63 \cdot 10^{-34}$ Js)
H_e	radiant fluence
I	intensity
k	thermal diffusivity
k_B	BOLTZMANN constant
l	cylinder length
M^2	beam quality factor
m_e	electron mass ($\approx 9.1 \cdot 10^{-31}$ kg)
N	pulse / plasma CCD count (depending on the context)
n	refractive index
N_e	electron number density
N_i	ion density
N_o	number of electrons in outermost shell
P_r	continuous recombination power spectrum
R	reflectivity
T	temperature
t_{exp}	exposure time
t_{rad}	time of radiation exposure
u	unified atomic mass unit
v	velocity
w	peak-to-valley wavefront distortion
w_0	initial beam waist radius
Z	atomic number
z_R	RAYLEIGH length

AOI area of interest
BS back side
FS front side
HAZ heat-affected zone
IB inverse bremsstrahlung

1 Introduction

1.1 Motivation

Transmission X-ray microscopy in the spectral range of the so-called “water window” region ($2.3 \text{ nm} < \lambda < 4.4 \text{ nm}$) is a powerful tool for the investigation of biological and mineralogical samples, as investigated in, e.g., [1] and [2]. One lab-scale implementation of a soft X-ray microscope is based on a laser-induced plasma source utilizing a pulsed gas jet [3]. When inducing plasmas in gas targets, in many cases the corresponding gas pulse shape and hence the resulting plasma emission need to be optimized such that as much soft X-ray radiation can be used for microscopy as possible. In this respect, it is of vital importance to specify the nozzle geometry that is used to form the gas pulse. Before this work, these nozzles were produced using wire erosion, supplying consistent geometries at a reasonable price. The associated problem is the inflexibility concerning different nozzle lengths, opening angles and hole diameters due to inherent geometrical limitations of the technique. This makes it desirable to enable production of said nozzles within the lab such that different geometries can be produced as required in order to obtain an enhanced particle density and thus an increased plasma brilliance.

1.2 Definition of Task

Within the scope of this work, wolfram nozzle plates are to be fabricated in a process comprising laser systems. Those nozzles are required to have defined geometries including hole diameters and opening angle (as illustrated in figure 3.4), and they should provide results comparable to those previously used. In this context, their performance is to be analyzed with appropriate measures in order to find the most suitable set of geometric parameters.

1.3 Outline

In the first part of this work, the reader is made familiar with some of the theory the later chapters build upon, including laser-target interaction, plasma basics, and optical methods. Afterwards, the processing and analytical methods used for the completion of the given task are outlined. The resulting data are presented and discussed in the subsequent section. After concluding the work and giving an outlook on what could be worked at in the future, some additional information is provided in the appendix.

2 Theoretical Aspects

The purpose of this section is to provide a theoretical background needed to understand the methods used in this work. Firstly, the interaction of laser radiation with targets is addressed, laying the foundation of laser drilling. This is followed by a short introduction to plasma physics which is necessary, since both processing itself as well as the analysis of the produced nozzles involves plasmas. Afterwards, optical methods implemented in the process are explained shortly.

2.1 Laser–Target Interaction

2.1.1 Electron–Phonon and Electron–Electron Interaction

The absorption of photons within some target is described by the MAXWELL equations and can be viewed as creating an internal energy source. In case of common laser wavelengths in the range from infrared to near ultraviolet, absorption occurs via acceleration of electrons within a time scale of about 10 fs [5]. In the special case of metal targets, the dominant process is absorption by means of *inverse bremsstrahlung* (IB). An important characteristic value of metals offering information about their optical properties is the *plasma frequency* ω_p which is described in detail in section 2.2.

As a consequence of absorption, an imbalance of the energy distribution is introduced, which returns to equilibrium state (*thermalization*) through electron–electron interactions (order of ≈ 10 fs, as follows from the DRUDE model) as well as electron–phonon interactions (\approx ps) [5]. Hence, the electron–electron transfer of energy is faster by about two orders of magnitude than in the case of electron–lattice interaction.

For pulse durations of some fs, the lattice does not have enough time to respond, and only the electron gas temperature rises significantly within the pulse duration. If, however, the pulse has a duration comparable to the lattice response time, a part of the energy can be directly coupled to it during

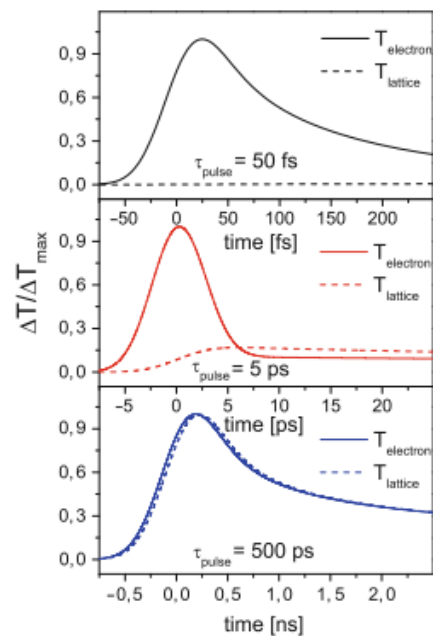


Figure 2.1: simulated time evolution of electron and lattice temperature in copper following different pulse durations, from [4]

the pulse and increase its temperature as well (see figure 2.1). This is one fundamental difference between ultrashort pulse and short pulse processing, resulting in different material responses, further discussed in section 2.1.2 [4].

If the rate at which energy is coupled to the electron system is slow compared to the thermalization rate, the coupled laser energy can be regarded as a usual heat source, termed *photothermal*. This is mostly the case for relatively long laser pulses ($\gg ns$) [5]. By doing so, numerical simulation can be restricted to solving the heat equation, which includes the temperature evolution, heat conduction and convection, immensely simplifying the calculations.

2.1.2 Localized Temperature Change

The actual absorption within some material depends on many factors such as radiation wavelength and intensity, incident angle, the material itself, as well as surface temperature and roughness. It can be assessed using the radiation intensity I and the material parameters absorption coefficient α and reflectivity R as follows [6]:

$$I_{abs}(t, z) = I(t)(1 - R)e^{-\alpha z}, \quad (2.1)$$

where z is the coordinate in the direction of laser propagation, and α originates from the well-known LAMBERT–BEER law.¹

When investigating the temperature change at the target surface and an adjacent volume, one also has to consider heat sinks, which primarily include phase transitions. This is especially important when approaching the *liquidus* temperature, as liquid material evaporates from the surface. In most cases, heat transportation can only be simulated numerically, e.g. utilizing the *finite differences* approach. One characteristic parameter in this context is the *thermal penetration depth*, which is a measure for how deeply a laser pulse affects the material, estimated by

$$\Lambda \approx \sqrt{4k\tau}, \quad (2.2)$$

where k is the thermal diffusivity and τ is the pulse length [5]. For the case of wolfram ($k \approx 68 \cdot 10^{-6} \text{ m}^2\text{s}^{-1}$ [7]) and $\tau = 9 \text{ ns}$, this leads to $\Lambda \approx 1.6 \mu\text{m}$. Utilizing ultrashort laser pulses of e.g. $\tau = 150 \text{ fs}$ yields $\Lambda \approx 6.4 \text{ nm}$.

This leads to the relation between heat-affected zone (HAZ, the *area* of affected material) and pulse length: As indicated in section 2.1.1, ultrashort pulses deposit energy too quickly for thermal relaxation to occur during the laser pulse duration. Hence, less heat will be conducted, and morphological as well as structural changes caused by heat conduction may be prevented. It

¹Note that the law is not valid for very high intensities, where saturation effects become significant, hence complicating the calculation.

is also possible to prohibit any interaction with a potential plasma, if the repetition rate is below a critical value depending on the plasma lifetime, which needs to be considered when processing substances.

In general, liquefied material has a higher reflectivity, reducing the absorbed power and thus leading to a lower surface temperature. In case of high intensities, this also has an influence on surface roughness and geometry of the target, giving rise to complex dynamics of the heating process. This renders any preceding simulation unnecessary, because the boundary conditions would need to be determined to a higher degree than possible within the scope of this work.

2.1.3 Surface Effects

The aspects discussed in section 2.1.2 cause various effects that occur on the target surface and shall be explained here.

Explosive Vaporization At sufficiently high laser power densities of a few GW/cm^2 depending on the process parameters, material below the surface reaches its vaporization temperature before the surface itself has had enough time to vaporize [8]. This causes *recoil pressure* to be formed, initially accelerating the evaporated molecules onto a trajectory normal to the target surface. However, due to their interactions with their neighbors, velocity becomes distributed (MAXWELL distribution), and the resulting vapor plume expands into all directions [9]. This includes the possibility of re-condensing material on the surface, leading to further topological changes. The region in which the transition from normal to distributed velocity occurs is called KNUDSEN layer and comprises some mean free path lengths $\langle \xi \rangle$. On the whole, however, matter from the target is ablated, and by continuing irradiation a hole may be formed.

Mass Transport The motion of material on the target surface results from a combination of various effects, primarily based on temperature- and pressure-induced phenomena. Those include convection of molten material and the aforementioned evaporation. Also, the so-called *piston mechanism* is of importance: Within the region of the laser spot, the high plasma and recoil pressure act on the liquefied target material. Since the surrounding pressure is much lower, the material is moved away from the spot center, and it forms what resembles a crater (cf. figure 4.2a). In the context of this work, this is an undesired effect, since it may impair the gas flow running through the nozzle.

2.2 Basics of Plasma Physics

Since induction of and interactions involving plasmas are of vital importance within this work, a brief theoretical background shall be given within the following sections.

2.2.1 Plasma Characteristics

In general, a plasma can be seen as a mixture of electron and ion gas, with the electrons being much lighter compared to the ions. This mixture contains neutral, positive and negative atoms and molecules, while being neutral as a whole (due to COULOMB interaction). There are several characteristic properties and parameters used to describe plasmas, which shall be presented briefly.

- Its average *degree of ionization* shows the amount of ionized particles, with a value of 0 in the case of exclusively neutral molecules [10].
- Both ion and electron gas generally may have their own temperatures T_e , T_i and number densities n_e , n_i , each influencing the specific plasma behavior. The mean temperature $\langle T \rangle$ is an expression of their respective mean energy $\langle E \rangle$, following the equation

$$\langle E \rangle = \frac{3}{2} k_B \langle T \rangle, \quad (2.3)$$

in this case with three degrees of freedom and k_B as the BOLTZMANN constant.

- The *coupling parameter* Γ describes the atomic interconnection and thus the occurring aggregate state. Typically, the gaseous state occurs for $\Gamma < 1$, the solid state for $\Gamma > 200$, and the liquid state in between. Most commonly, the plasma exists in the gaseous state; there are, however, also cases, in which it is present as a liquid or in a crystallized state.
- One property of a plasma is the so-called DEBYE *shielding*, i.e. the reduction of (external) electric fields. Because electrons and ions can move rather freely within the plasma, those fields lead to spatial distributions of the charges which weaken the impact. In this context, the DEBYE lengths λ_{De} and λ_{Di} (for electrons and ions, respectively) play an important role, as well. They describe the distance from the electronic perturbation that is needed for the shielding to be effective.
- The last aspect that shall be mentioned here is the *plasma frequency* ω_p . It gives the angular resonance frequency of the electron subsystem,

which oscillates as a collective with respect to the ion background. As such, it can be used to characterize the response time of the plasma [11] and, as a consequence, the interaction of the target with electromagnetic radiation. It is given by

$$\omega_p = \sqrt{\frac{N_e e^2}{m_e \epsilon_0}}, \quad (2.4)$$

where N_e is the metal's electron number density, m_e is the mass of an electron, e is the electron charge, and ϵ_0 is the permittivity of free space. Below this frequency, the corresponding electromagnetic field moves slowly enough for the free electrons to directly follow it, resulting in high values for reflectivity [5].

In the following, an estimate for a typical value of w_p for this work shall be calculated.

The free electron number density $N_{e,w}$ of wolfram can be estimated using its number of electrons in the outermost shell $N_o = 2$, atomic mass $A_{r,w} = 183.84$ u and mass density $\rho_w = 19.25$ g/cm³ (at room temperature [12]) as follows:

$$N_{e,w} = Z \frac{\rho_w}{A_{r,w}} \approx 1.3 \cdot 10^{23} \text{ cm}^{-3} \quad (2.5)$$

Plugging this value into equation (2.4) yields the characteristic plasma frequency of wolfram at room temperature $w_{p,w} \approx 2 \cdot 10^{16}$ Hz, which can be converted to the corresponding wavelength $\lambda_{p,w} \approx 15$ nm using the common relation

$$\nu = \frac{c}{\lambda}. \quad (2.6)$$

Consequently, there is significant reflectivity for wavelengths $\lambda > 15$ nm. At $\lambda = 525$ nm, which is close to the wavelength used in this work (see section 3), the value is $R_{525 \text{ nm}} = 0.508$ (determined at a small angle of incidence; no exact value for the angle is given in the reference) [13].

Another equivalent, very common method is to calculate the laser wavelength-dependent critical electron density N_{crit} and then to compare it to the given material characteristic N_e . Upon rearranging, and plugging in the laser frequency w for w_p , equation (2.4) becomes

$$N_{crit} = \frac{\omega^2 m_e \epsilon_0}{e^2} \quad (2.7)$$

(here only the positive solution makes physical sense). For a setup uti-

lizing a laser with $\lambda = 532$ nm, this results in $N_{crit} \approx 4 \cdot 10^{21}$ cm⁻³.

Since $N_e \gg N_{crit}$, the plasma in this work is called *over-dense*, resulting in a high reflectivity as shown above. Due to this high reflectivity, the repetition rate f_{rep} should be kept low enough such that a laser pulse does not interact with the plasma caused by the previous pulse, preventing it from reaching the target.

Since *plasma emission* is of particular importance for the justification of this work, it shall be discussed a little more closely in section 2.2.3.

2.2.2 Plasma Induction

With sufficing laser intensity, the electric field of the incoming radiation is strong enough to ionize either the vaporized target plume (see section 2.1.3) or the surrounding gas via IB. Initially, this process mainly involves collisions of electrons and neutral atoms due to the relatively small fraction of ions. With an increasing number density of ions, however, electron-ion IB starts to dominate over these collisions due to attracting long-range COULOMB forces between the said charged particles [10].

The threshold intensity to induce a plasma in gas (plasma threshold) usually is in the order of $10^9 - 10^{11}$ W/cm², while it is significantly lower in the vicinity of a metal target [14]. Consequently, a plasma is commonly formed close to the metal target surface, since the threshold is lower there. This plasma may exhibit strong absorption and thus expand towards the laser beam by converting the surrounding gas to plasma due to its thermal radiation and high pressure.² This can be seen as the plume “propagating” and is generally termed *Laser Supported Absorption Wave (LSAW)*. This energy absorption can be divided into two parts: *Resonant* absorption occurs when the photon frequency ω matches either the transition energy E_{trans} of two quantized atomic levels so that $\hbar\omega = E_{trans}$, or the plasma frequency w_p , which describes the oscillation of the charge density within a plasma. *Nonresonant* absorption, on the other hand, involves the interaction of photons and free charges within the plasma, i.e. IB.

The processes initially leading to plasma expansion later cause its decay. In many cases, plasmas are observed to be quite dense, promoting collisions between the contained atoms and molecules to be the main cause of expansion into free space and hence its return to local thermal equilibrium.

²It should be noted here that plasma absorption can be avoided by using ultrashort (< 1 ps) pulses, since plasma formation takes longer than the pulse duration then.

2.2.3 Plasma Emission

Apart from absorbing electromagnetic radiation, a plasma is capable of emitting it, as well. When a free electron of velocity v is trapped by an ion in a state with binding energy E_i , recombination radiation of the difference energy occurs:

$$E_{ph} = \hbar\omega = E_{kin} - E_i = \frac{1}{2}m_e v^2 - E_i \quad (2.8)$$

with E_{kin} and m_e as the kinetic energy and mass of the electron. Using the electron-trapping cross section σ_i , the ion and electron number densities N_i and N_e and the most probable velocity $\langle v \rangle$ (from MAXWELL velocity distribution), one can calculate the continuous recombination power spectrum P_r to be

$$P_r = \frac{N_i N_e h^2 \sigma_i(v) v}{m_e \pi^{3/2} \langle v \rangle^3} \int_{\nu=0}^{\infty} \nu \exp(-((\nu - \nu_0)/\nu_0)^2) d\nu. \quad (2.9)$$

However, in addition to this continuous spectrum, plasmas also exhibit spectral lines depending on the specific plasma species. An example of this is given in figure 2.2, which shows the emission spectrum around the water window of plasmas created with Ar targets, including several ionic Ar lines [15]. As said before, parts of this spectrum can be filtered out to yield, e.g. soft X-ray sources, which are otherwise provided only with quite some effort.

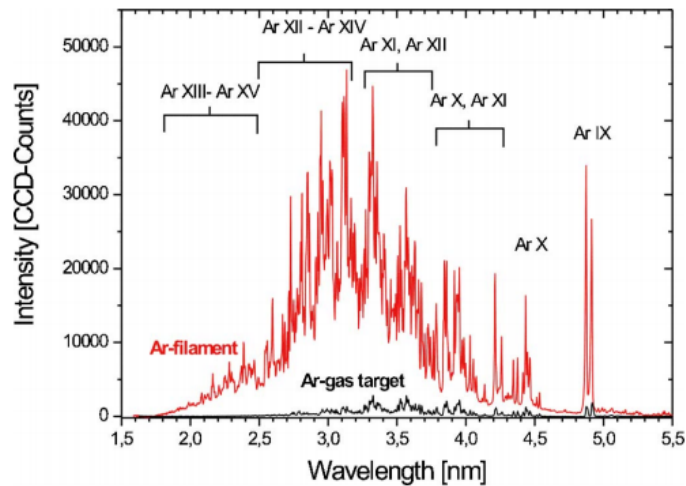


Figure 2.2: emission spectrum of laser-induced Ar target plasma (red: solid target; black: gaseous target); from [16]

2.3 Used Optical Methods

A brief explanation of the used optical methods and setups will be given within the following sections to make it understandable for the reader, why those were implemented.

2.3.1 Schlieren Technique

To be able to understand why the Schlieren technique realized in section 3.2.2 works, its basic principle shall be explained here. Firstly, some foundation involving FOURIER *optics* shall be laid.

Using the mathematics behind the FRAUNHOFER approximation, it can be shown that a lens acts as a FOURIER transformer. Specifically, the object plane $f(x, y)$ is focused on the FOURIER plane, where the transformation $\mathcal{F}(f(x, y)) := \tilde{f}(u, v)$ occurs, where u and v are the corresponding spatial frequencies that compose the object. Adding a second lens two focal lengths after the first one will recreate the image. This configuration, termed *4f-correlator*, can be seen in figure 3.9. Following the property

$$\mathcal{F}\{\mathcal{F}\{f(x, y)\}\} = \mathcal{F}^2\{f(x, y)\} = f(-x, -y), \quad (2.10)$$

the image will have inverted arguments, meaning that the sides are switched and up is down.

The benefits of this procedure are that in the FOURIER plane, changes to the spatial frequencies of the image can be made which cause the corresponding changes in the image plane, comparable to digital signal processing techniques. Those changes can, for example, be summoned by the use of apertures. While small details are represented by high spatial frequencies, the basic features of an image rely on low spatial frequencies [17].

Using suitable setups including e.g. low- or high-pass filters will *not* lead to more image details, but it might make those that are available more easily visible [18]. The *Schlieren technique* is one such setup, employing a knife edge as the filter within the FOURIER plane, blocking half of the incident light [19]. It relies on the relationship between refractive index and density of one transparent (at illumination wavelength) medium, the LORENTZ-LORENZ equation f_{LL}

$$f_{LL}(n) := \frac{n^2 - 1}{\rho(n^2 + 2)} = \text{const.} \quad (2.11)$$

with n as the refractive index and ρ as the medium density.

Expanding equation (2.11) around $n = 1$ — since in this thesis, only gases with $n \approx 1$ are of interest — and neglecting terms larger than 2nd order

$$\sum_{i=0}^1 \frac{f_{LL}^{(i)}(n_0)}{n!} (n - n_0)^i = 0 - \frac{2}{3} \frac{n - 1}{\rho} \Rightarrow \frac{n - 1}{\rho} = \text{const.}, \quad (2.12)$$

the equation simplifies to the GLADSTONE–DALE equation. Consequently, one can calculate density changes using the change in refractive index. Following SNELL’s law

$$n_1 \sin(\alpha) = n_2 \sin(\beta), \quad (2.13)$$

a light beam within a scalar refractive index field $n(\vec{r})$ will be refracted towards the higher index, bending its wavefront, which can lead to the beam passing the knife edge, even if it would usually be blocked by it. As a consequence, however, only index gradients that are orthogonal to the knife edge (in this case in x -direction) can be made visible, because only those will cause the beam to be refracted “around” it [20]. An improvement in this respect is given by utilizing the HARTMANN–SHACK technique, which is explained further in section 2.3.2.

An additional disadvantage is diffraction at the edge, producing interference patterns added to the wanted signal. However, since the Schlieren technique is used only as a qualitative means within this work, this disadvantage is insignificant.

2.3.2 Hartmann–Shack Sensor

As explained in the previous section, the scalar refractive index field causes a wave propagating through it to be bended. A wavefront measurement can be used to obtain the refractive index distribution within the region of interest, and hence, following equation (2.11), the corresponding density distribution of the medium can be calculated. A wavefront is defined as the surface of the same phase at a position z_0 . One possibility to gain knowledge of the shape of the wavefront deformation caused by some disturbance is by making use of the HARTMANN–SHACK technique, illustrated in figure 2.3 [21] [22]. The principle is based on determining the local angles β_{xy} between a reference wavefront (acquired before the experiment takes place)

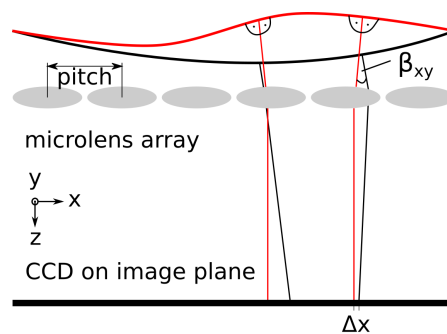


Figure 2.3: illustration of HARTMANN–SHACK principle: black: reference wavefront; red: perturbed wavefront

and the wavefront recorded at a time of interest. One type of implementation uses a microlens–array (as seen in figure 2.3) to split the wavefront into multiple beams. Thus, the lateral resolution is limited by the *pitch*, i.e. the distance between the centers of neighboring micro lenses. The corresponding foci on the image plane are measured by a CCD sensor. Comparing the spatial foci positions of reference and measurement wavefront ($\Delta x, \Delta y$ (not visible in depiction)) then allows for reconstruction of the distortions that were introduced within the region of interest. For a more detailed description of the mathematics behind the reconstruction, it shall be referred to source [23].

3 Methods

In this section, the most important methods used in the context of this work shall be presented briefly, separated into processing and analysis techniques.

3.1 Drilling

The purpose of this section is to outline the methods that are used within this work to obtain the desired bore geometries. The choice of an adequate method is based primarily on factors such as geometry specifications as well as cost and time efficiency. In figure 3.1, the vital dimensions of the desired nozzle are depicted.

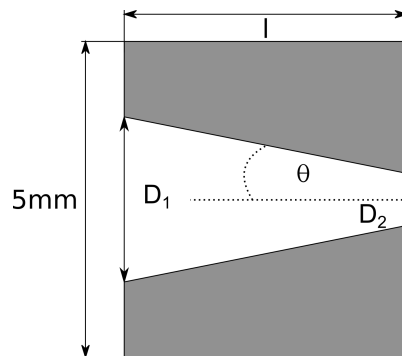


Figure 3.1: side view: geometry of nozzle plates with θ as the opening half angle, D_1 and D_2 as the front and back hole diameter, l as the nozzle length

3.1.1 Percussion Drilling

The laser–driven drilling method requiring the smallest amount of effort is undoubtedly percussion drilling, in which there is no relative motion between optical laser axis and the workpiece, both being static. In case of single pulse drilling, pulse energies need to be rather high, usually employing relatively long pulse durations of a few hundred μs . Disadvantages include the formation of a relatively large heat–affected zone due to the long pulses (cf. section 2.1.3) and the strong dependence of the hole geometry on laser pulse shape, thus causing strong variations between consecutive bores.

Allowing for multiple pulses greatly improves possible accuracy, as the bore is drilled in several, more defined steps. Additionally, one can achieve higher aspect ratios (*depth/diameter*) and bore depths. However, a strong dependence

of the bore geometry on the focus shape remains, as can be seen in figure 4.9a, which demonstrates the elliptical focus shape caused by astigmatism. The hole on the backside of the workpiece commonly is significantly smaller than the front one, which results from the bore guiding a part of the laser radiation via total reflection.

The experimental setup used to implement the method in this work is depicted in figure 3.2. An *InnoLas SpitLight DPSS OPO* provides laser radiation with a pulse duration of $\tau = 9$ ns at a wavelength $\lambda = 532$ nm at a scalable pulse energy from about 22.5 mJ to 150 mJ and repetition rates from 1 Hz to 100 Hz. Other laser parameters include a flat-top beam profile and an exit beam diameter of $D_{exit} < 6.5$ mm [24].³

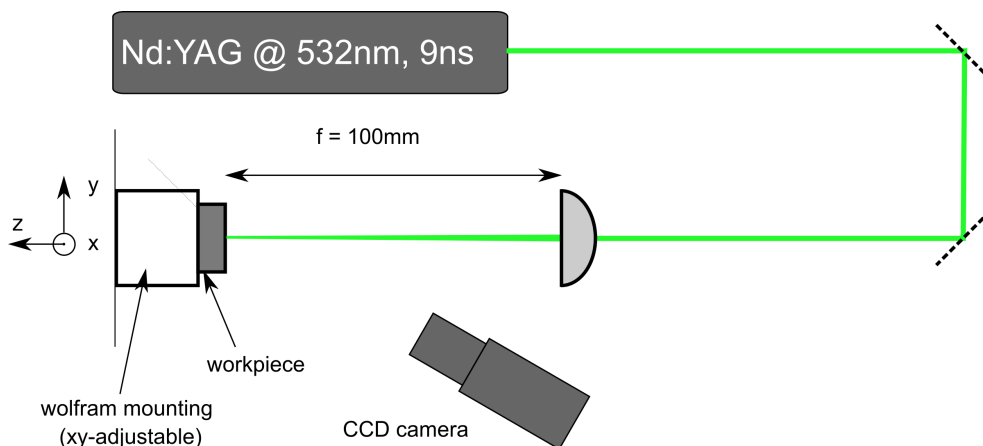


Figure 3.2: setup used for percussion drilling

To move the workpiece within the xy -plane, a combination of two *OWIS LTM 80* motorized linear stages is used, implying a positioning error of $< 25 \mu\text{m}$ per 100 mm translation and a repeatability of $< 15 \mu\text{m}$ in each direction. A CCD camera (Sony ICX285AL chip, 1360×1024 active pixels, $6.45 \mu\text{m} \times 6.45 \mu\text{m}$ pixel size, for spectral sensitivity see figure A.2) allows observation of the workpiece and aiming the laser radiation after correct adjustment. The focusing lens is positionable in z direction using an ordinary linear stage. Since the setup involves rather high optical power levels, *dielectric mirrors* are employed. This need is caused by the fact that common mirrors may not provide sufficient reflectivity, leading to significant absorption in case of high-power laser pulses, exceeding the damage threshold of the mirror. In these cases, dielectric mirrors, which exhibit highly different reflectivities and transmittances at two wavelengths, provide a solution [25].

³Note that the pulse energies stated from here on are based on the assumption that the pulse energy varies linearly with the applied Pockels cell voltage, which is a reasonable assumption within the lower energy range, although it was not measured.

Commonly, they are based on the interference of reflected light at thin films of various refractive indices n_i , as can be seen in figure 3.3, with A_i being the corresponding amplitudes. For maximum reflectivity, the reflected light at each interface needs to have the correct phase relation, requiring specific film thicknesses and making it obvious that the mirror properties depend on the light wavelength. In this respect, it has to be considered that a phase shift of π occurs at transitions with $n_i < n_{i+1}$. With increasing number of thin films and using this principle, reflectivities of up to 99.9999% have been achieved [25]. For a more detailed description, it shall be referred to source [17].

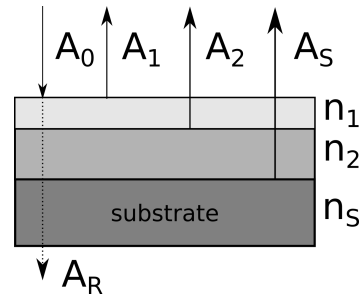


Figure 3.3: reflections at thin films and substrate of a dielectric mirror

3.1.2 Trepanning

Strictly speaking, trepanning does not represent a drilling, but much rather a cutting technique. Relative motion of the optical axis around a closed path on the workpiece leads to cutting along that path, resulting in various hole geometries. In contrast to percussion drilling, the back hole may be bigger than the front one, as depicted in figure 3.4 (provided that the irradiation time is sufficient). Note that in the sketch, the workpiece is the reference system, while in reality, usually the laser system is static and the workpiece is moved relative towards it, though there are also optical systems which accomplish the workpiece motion. In this work, rotation around z and translation in the xy -plane are implemented.

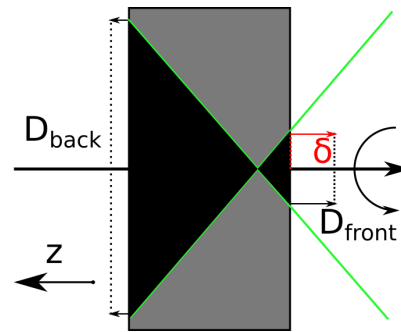


Figure 3.4: illustration of trepanning; note: in practice, the geometry is a lot more blurred (especially at the crossing) due to defocussing, heat diffusion and guidance of the laser radiation

One vital advantage over percussion drilling is the fact that due to the rotational motion, the resulting hole shape depends significantly less on the shape of the laser focus. However, this comes at the cost of a simultaneous increase in overall hole size.

The setup used for trepanning is depicted in figure 3.5, a photo can be viewed in figure A.11. To improve precision, a telescope was implemented, a common

method in optics for decreasing the minimally achievable beam waist.⁴ At a position $z' = f/[1 + (f/z_R)^2]$ after a lens with focal length f , a beam waist of initial radius w_0 is focused to a radius w'

$$w' = \frac{w_0}{\sqrt{1 + (z_R/f)^2}} \stackrel{2z_R \gg f}{\approx} \frac{f}{z_R} w_0, \quad (3.1)$$

where z_R is the Rayleigh length and $2z_R$ the depth of focus. Plugging in the RAYLEIGH length $z_R = \pi w_0^2/(M^2\lambda)$ in equation (3.1) yields

$$w' = \frac{M^2\lambda f}{\pi w_0}, \quad (3.2)$$

from which it becomes apparent that a bigger initial waist enables a smaller spot size [26]. The corresponding implementation can be seen in figure 3.5 (corresponding lenses: $f_1 = -50$ mm and $f_2 = 500$ mm, resulting in a magnification $M_{f_1, f_2} = |f_2/f_1| = 10$). With an output diameter of $w_0 \approx 6.5$ mm [24], a beam quality factor of $M^2 \approx 1.7$ [27] and including the telescope as well as a focusing lens with $f = 200$ mm, equation (3.2) yields $w' \approx 0.9$ μm . However, due to aberrations (e.g. due to the high ratio of beam diameter and lens size as well as a presumably much higher beam quality factor M^2 as given in literature), the focus size in practice rather lies in the range of 80 μm .

Assuming this value as the focus size, the corresponding depth of focus is estimated to be $2z_R \approx 22$ mm.

Motion and monitoring of the workpiece are provided similar to the previous section 3.1.1, with the addition of a goniometer table which is used to regulate the bore opening angle.

Equation (3.3) gives an estimate of typical average optical intensities $\langle I \rangle$ that are involved in the trepanning process of this work. The parameter set $\{21 \text{ mJ} < E_{pulse} < 37.5 \text{ mJ}, f_{rep} = 100 \text{ Hz}, D = 80 \mu\text{m}\}$, containing values typical of the used setup, was used for the calculations.

$$\langle I \rangle = \frac{f_{rep} \cdot E_{pulse}}{\pi(D/2)^2} \Rightarrow 41.78 \frac{\text{kW}}{\text{cm}^2} < \langle I \rangle < 74.6 \frac{\text{kW}}{\text{cm}^2} \quad (3.3)$$

To achieve a predetermined bore diameter on the front side (FS), the process is divided into three steps:

- (i) First, the optical axis needs to be carefully adjusted to the rotational axis of the workpiece. This needs to be repeated for every drilled nozzle, since the removal of the nozzle mounting introduces small changes in the setup and hence represents a jump within the parameter space.

⁴This is possible on the condition that the associated lenses were not fully illuminated beforehand. Otherwise, a telescope may be used to increase the free working distance.

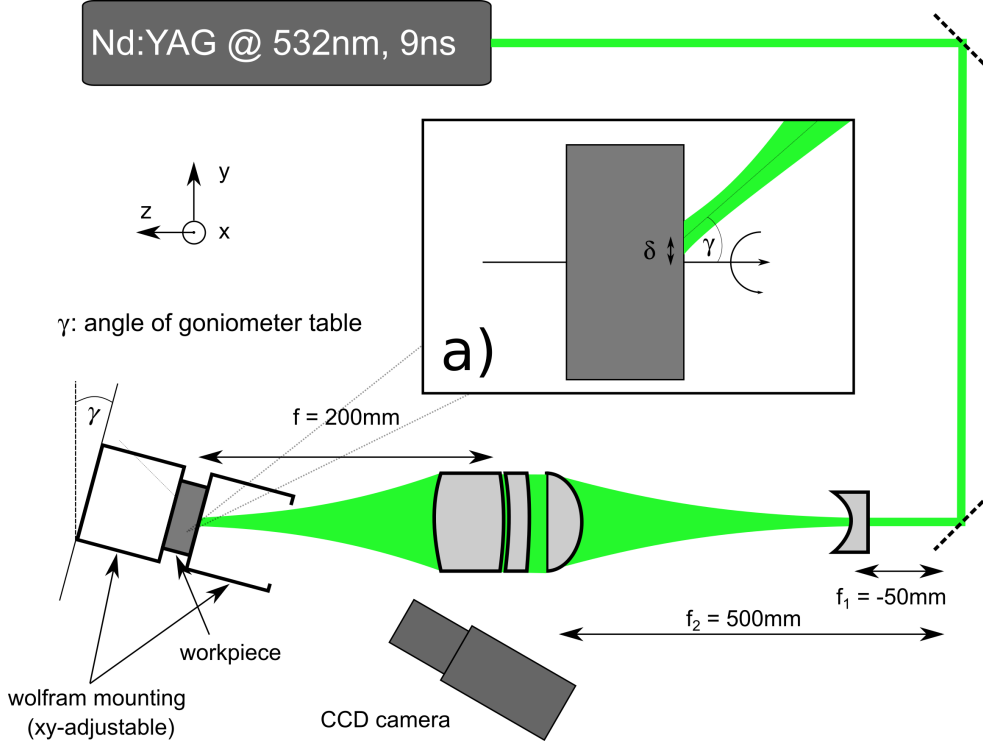


Figure 3.5: setup used for trepanning, inset a): visualization of crucial process parameters δ and γ

- (ii) Afterwards, the size of the HAZ D_{HAZ} has to be determined using the in-line observation system, representing the smallest possible FS bore diameter.
- (iii) Lastly, the required value of δ is calculated as follows, with D_{FSD} being the desired frontal hole diameter:

$$\delta = \frac{1}{2}(D_{FSD} - D_{HAZ}) \quad (3.4)$$

Obviously, the precision of this method is limited by the measurement accuracy of the observation system, as well as by fluctuations introduced by the mechanical parts.

Nozzle plates with different lengths $l = \{0.3, 0.5, 1\}$ mm were produced. However, with this setup, adequate opening angles could be achieved only with lengths $l > 0.5$ mm. As such, nozzle plates with a length lower than that are not regarded from this point onwards.

In a second part of the experiment, a Lumera HYPER RAPID ps laser system supplies the laser radiation so that the influence of pulse duration can be studied, with the rest of the setup remaining unaltered. This includes frequency-doubled radiation at $\lambda = 532\text{nm}$ as well as an average power of $\langle P \rangle = 14\text{W}$ and a pulse energy of $E_{pulse} = 14\mu\text{J}$ at $f_{rep} = 100\text{kHz}$. The

beam has an exit diameter of $D \approx 3$ mm, a polarization ratio of $\gg 100 : 1$, and a TEM₀₀ profile with $M^2 < 1.4$ [28]. However, due to the laser belonging to a different group, the laser system was available only for a short amount of time, and only superficial findings could be made (cf. section 4.1.1).

3.1.2.1 Experimental Problems

There were a few problems in the lab work that had to be faced to improve the results achieved with trepanning:

- Since holes with diameters in the order of a few 100 μm had to be fabricated, the setup cannot allow for large spatial deviations and thus reduce its precision. This includes the motion of the linear tables and the mobile lens, as well as the rotation and fixation of the specimen. In a first stage, the rotating and mounting unit looked like presented in figure A.10. Several aspects reduce the achievable bore quality: First, non-uniform motor motions are transferred from the motor to the mounting, resulting in asymmetric rotation. Secondly, the ball bearing, which is used to keep hold of the mounting, stopped running smoothly one day, resulting in non-circular bores (see figure 3.6⁵). Furthermore, deviations of the laser system itself need to be considered, including intensity fluctuations and pointing stability.
- Since it is more feasible in practice to have the wolfram plates delivered, instead of cutting them out of a wolfram sheet with a laser, a mounting system is necessary for holding the workpiece in the correct position. For a more detailed view on this system, see section A.4. It involves two disadvantages: Firstly, it has to be disassembled from the rotational device before another wolfram plate can be inserted, resulting in the need to manually readjust the setup (especially the z -position of the focus) after each replacement. Secondly, for too large goniometer table angles γ , it blocks a fraction of the incident laser radiation, resulting in a linear edge and hence even smaller circularity (cf. figure 3.7).

⁵Note that this is a rather extreme example, and that the quality of the rotation afterwards could be improved to some extent with mechanical measures.

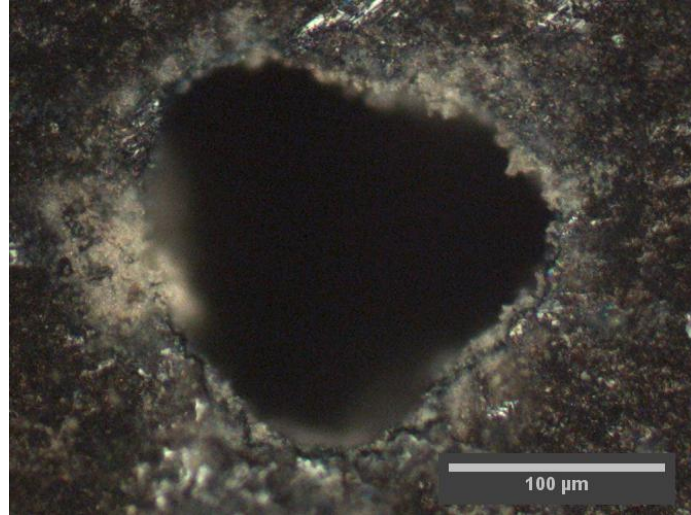


Figure 3.6: non-circularity due to ball bearing not running smoothly

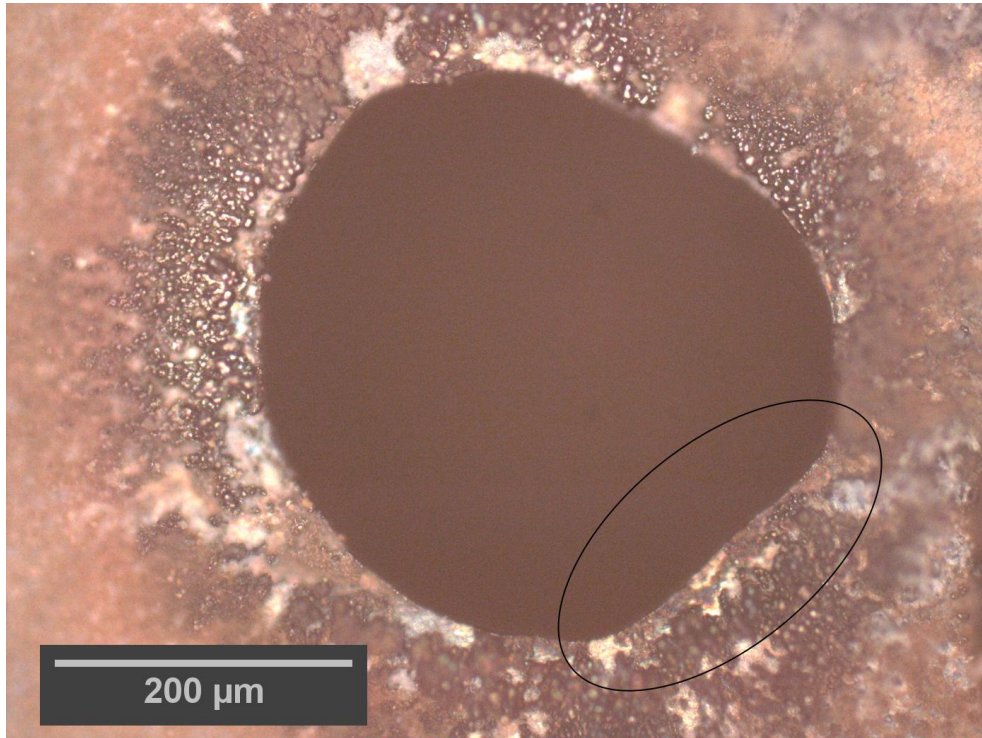


Figure 3.7: result of cut-off beam, parameters: $E_{pulse} = 30 \text{ mJ}$, $\eta \approx 3000$, $f_{rep} = 100 \text{ Hz}$, $\delta = 40 \mu\text{m}$, $t_{rad} \approx 20 \text{ min}$

A small study of repeatability is conducted to see the fluctuations inherent to the setup itself, excluding the change of plates. For this purpose, several bores using the same parameters were produced (see table 1). The resulting average values including standard deviation (relative and absolute) are

$$D_{FS} \approx (140 \pm 6) \mu\text{m}, D_{BS} \approx (350 \pm 59) \mu\text{m}, \frac{\sigma_{D_{FS}}}{140 \mu\text{m}} \approx 4.3\%, \frac{\sigma_{D_{BS}}}{350 \mu\text{m}} \approx 16.9\%$$

which demonstrate the large fluctuations, especially for the hole diameter of the BS, as explained above.

N°	$D_{FS}/\mu\text{m}$	$D_{BS}/\mu\text{m}$
1	138	368
2	143	263
3	131	405
4	149	318
5	144	394

Table 1: reproducibility, $\delta = 0 \mu\text{m}$, $f_{rep} = 100 \text{ Hz}$, $\theta = 9^\circ$, $E_{pulse} = 30 \mu\text{J}$, $\eta \approx 3000$, $t_{rad} \approx 20 \text{ min}$

3.2 Analysis

3.2.1 Topography

For the characterization of the specimen's surface, a confocal microscope was used. Its underlying operating principle shall be explained briefly in this section. The basic setup of the commercially available confocal microscope that was used in this work (*Sensofar PL μ 2300*) is presented in figure 3.8.

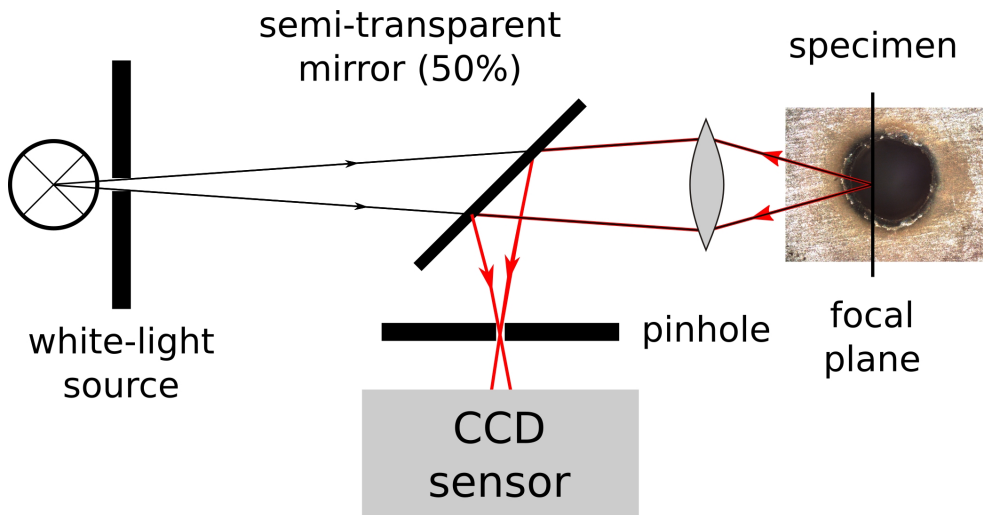


Figure 3.8: basic principle of confocal microscopy used for topography

A white-light source passes an aperture to approximate a point source. At a semi-transparent mirror, the beam is split into two equal parts: While the reflected half is lost, the transmitted beam is imaged onto the specimen. A pinhole is positioned before the image sensor (commonly a CCD). Light that originates from the focal plane will be focused within this pinhole, and hence pass it, while light from different planes will be focused somewhere else and

thus be mostly blocked. By parallel displacement of the focal plane, a height profile of the surface can be constructed.

For a complete 3D image, the surface has to be scanned, as well, i.e., this process has to be repeated over a raster. In combination with the fact that due to the pinholes, only a small fraction of the illumination can be used (small *light efficiency*), causing the need for long exposure times, this method is rather slow. To increase recording speed, one can use multiple pinholes (e.g. implemented in NIPKOW disks). On the pro-side, however, increased resolution and contrast can be achieved in consequence of the following two aspects: On the one hand, only a small volume of the specimen is illuminated (termed the *point spread function*). On the other hand, only light from near the focal plane can pass the pinhole and reach the image sensor.

The Sensofar PL μ 2300 in combination with a 10XEPI objective, which was used for the corresponding measurements in this work, feature a lateral resolution of 1.66 μm at a maximum slope of 14° as well as a repeatability of $< 50 \text{ nm}$.

One interesting characteristic feature of this method is that at no point in time, a whole image is created on the sensor, but only sections of it [29].

3.2.2 Schlieren Technique

In order to visualize the density distribution of the emitted gas pulse, the Schlieren technique was used during the experiments. It should be noted that those measurements are only evaluated on a qualitative level in order to learn about the correlation of density distribution and plasma shape. For a quantitative analysis, it shall be referred to sections 2.3.2 and 3.2.3.

3.2.2.1 Setup

The *Schlieren* technique is a method commonly used for the imaging and quantification of density gradients in fluids and gases. There are several variations, only one of which shall be presented here, depicted in figure 3.9.

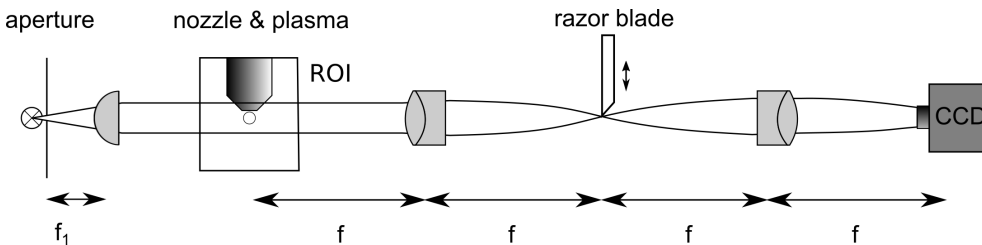


Figure 3.9: Schlieren setup based on a $4f$ -correlator

The basis of this variant is the $4f$ -correlator explained in section 2.3.1.

A light source radiates onto an aperture, approximating a point source. Principally, white light sources can be used for illumination just as well as laser systems, since coherence is no necessary matter. The exiting light is collimated by the first lens, after which the region of interest can be found, i.e. the escaping gas and the resulting plasma. A knife edge is positioned in the FOURIER plane, equal to the focal plane of the second lens, where it blocks some of the light focused on it. A CCD sensor (*Sony ICX285AL*, 1360×1024 active pixels, $6.45 \mu\text{m} \times 6.45 \mu\text{m}$ pixel size) is positioned in the image plane of the third lens to capture the data. While common sensors supply a fairly linear intensity-to-voltage transfer function within certain limits, it is important to prevent the sensor from reaching saturation, which would greatly distort the measurement data [20].

To make the results more available to the reader, a background is subtracted from the image such that only the differences caused by the gas flow are presented.

3.2.2.2 Adjustment

To obtain measurement data of high quality, the setup has to be well-adjusted. Apart from the usual alignments such as receiving a well-collimated illumination beam, and positioning the lenses according to their focal lengths, one vital aspect is the z -position of the knife edge. It needs to be carefully aligned such that the intensity distribution on the image plane changes homogeneously while moving the knife edge towards the focus on the xy -plane, as is the case in figure 3.10. In other words, careful adjustment in z reduces intensity drift to a minimum. Note that image details get lost while the knife edge is brought further into the focus. This explains the need for the second adjustment: Before measurement starts, the degree of blocking should be determined, i.e. the so-called *cut-off*. With this respect, one has to consider that too much cut-off leads to high-contrast results but few details in low-gradient regions, while too little cut-off causes poor contrast and hence little gain of information. In this work, it was decided that a reduction of intensity to about one half should be sufficient, as is illustrated in figure 3.10d. The round structures that can be seen result from impurities on the windows of the vacuum chamber, i.e. they are static and can be removed during post-processing of the image by subtraction of a background.

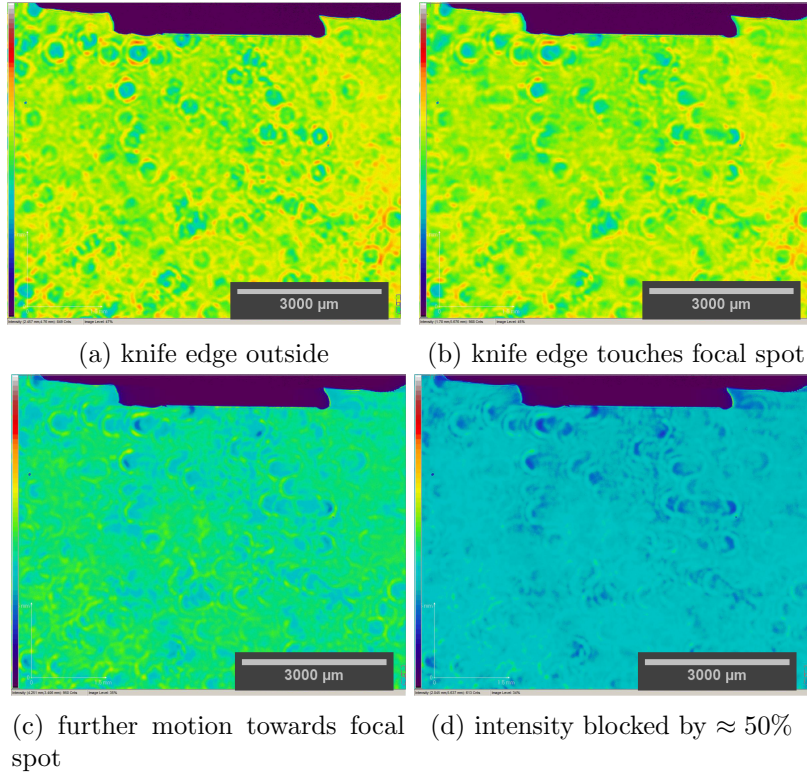


Figure 3.10: Schlieren image at different knife edge positions in x -direction demonstrating an increase in contrast and simultaneous blurring, $t_{exp} = 10$ ms, gain = 1, offset = 0 Cts

3.2.3 Wavefront Distortion Measurement

The experimental setup used for the wavefront distortion measurements depicted in figure 3.11 is very similar to the one described in the previous section so that both methods can be combined to support the results. Though the 4f-correlator does not introduce any benefits in this setup, it remains in place so that the results can be compared to a higher degree. The HARTMANN-SHACK sensor features a focal length $f_{HS} = 3.3$ mm and a pitch of $Pitch = 150 \mu\text{m}$ (distance between the centers of two adjacent microlenses).

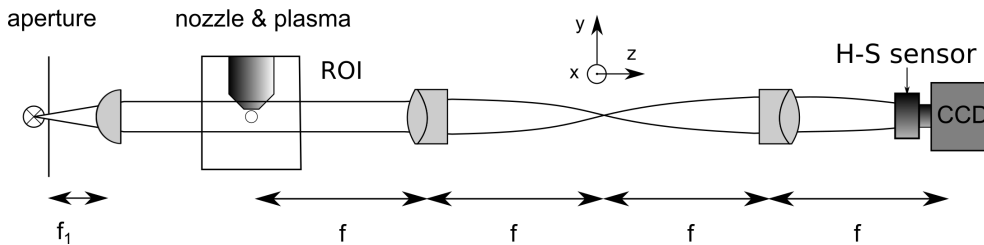


Figure 3.11: wavefront distortion measurement setup involving HARTMANN-SHACK sensor

As explained in section 2.3.2, knowledge of the wavefront deformation

can give information about the refractive index distribution $n(\vec{r})$, which in turn can be evaluated using equation (2.11) to yield the density distribution $\rho(\vec{r})$ within the region of interest. The magnitude of this deformation is given by w , which represents the peak-to-valley difference. Unfortunately, the Mathematica script provided for this calculation involved problems that have yet to be solved. This does, however, not pose a significant problem, since the wavefront analysis as well as direct plasma comparison provide sufficient data.

3.2.4 Plasma Characteristics

3.2.4.1 Setup

The setup used to analyze the plasma created below the wolfram nozzle is presented in figure 3.12, a photo thereof is available in figure A.14. An *InnoLas SpitLight Hybrid* supplies laser radiation at $\lambda = 1064$ nm, $E_{pulse} \approx 650$ mJ and $\tau \approx 9$ ns [30]. The laser beam is focused just below the wolfram nozzle which is connected via a high-pressure valve to a 50l gas cylinder filled with $p_N \approx 210$ bar nitrogen gas. A piezo actuator opens the valve following an electrical trigger signal so that a gas pulse flows through the nozzle just before the laser pulse ignites a plasma within. This plasma radially emits radiation as explained in section 2.2.3.⁶ A pinhole ($D = 50$ μ m) lets plasma emission within a small solid angle pass through a titanium filter with a thickness of 200 nm onto a CCD chip placed behind it (*Sony ICX285AL*, 1360×1024 active pixels, 6.45 μ m \times 6.45 μ m pixel size). The filter was produced at the faculty of physics in Göttingen. In order to detect the short-wavelength radiation, the sensor is covered with phosphor, acting as a wavelength converter (P43 produced by ProxiVision GmbH).

The transmission spectrum of the utilized filter is presented in figure 3.13, obtained in a calculation assuming pure titanium. It is commonly used as a bandpass filter [31], exhibiting high transmission in the range of the water window with a local transmission maximum at $\lambda \approx 2.88$ nm and blocking out significant parts of the visible range. Hence, the data thus produced demonstrate the ability of the induced plasma to provide radiation which can be used for water window microscopy. Examples are shown in section 4.2.3. Since the exposure time is generally longer than the duration of plasma emission, the plasma intensity is integrated over time to yield the radiated energy.

An exemplary nitrogen plasma emission spectrum after filtering with a Ti filter of 400 nm thickness is shown in figure 3.14. For reasons of security, a beam

⁶Note that in figure 3.12, only the fraction of the emission which reaches the detector is depicted.

trap is placed at the exit window of the vacuum chamber.

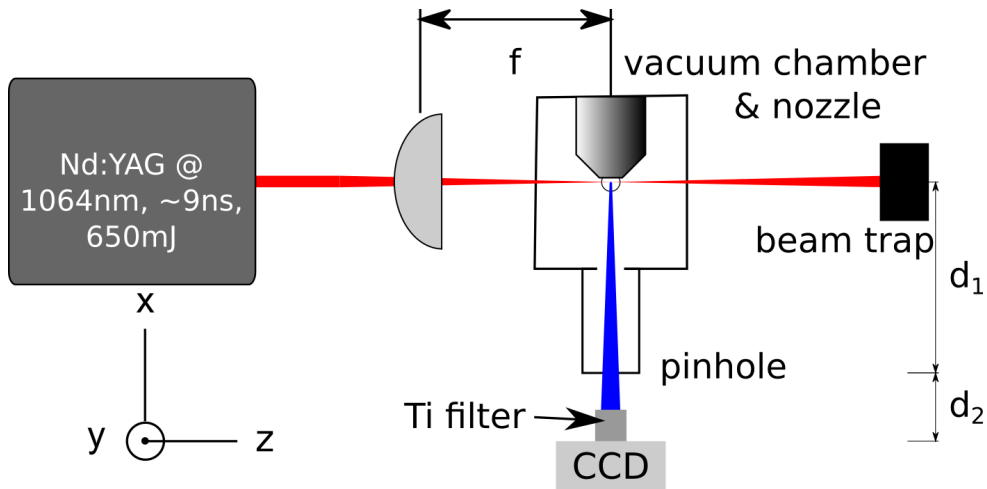


Figure 3.12: setup used for quantization of plasma emission (blue), $d_1 \approx 80$ mm, $d_2 \approx 130$ mm

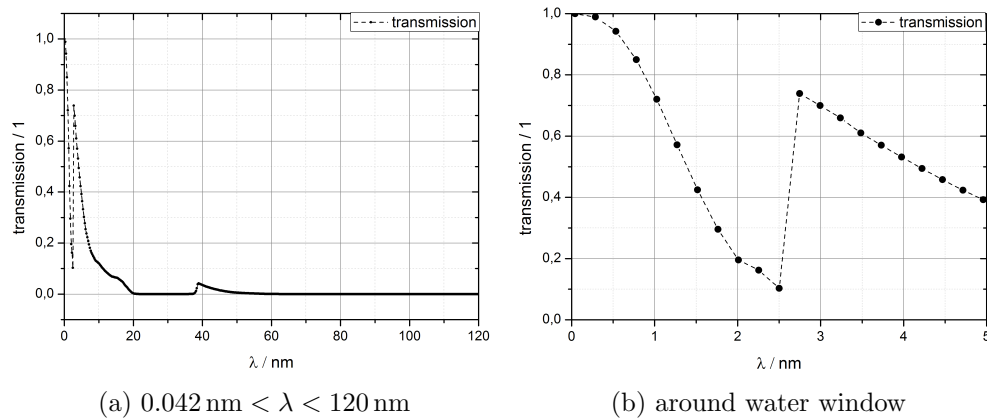


Figure 3.13: transmission spectrum of Ti filter, thickness: 200 nm, data obtained from [32]

3.2.4.2 Adjustment

In order to be able to compare the results obtained with this method, careful adjustments have to be carried out.

- After the laser beam is aligned properly, the N_2 pressure level needs to be noted and kept at the same value during each measurement.
- The timings of laser pulse, valve opening and camera exposure are synchronized via computer.

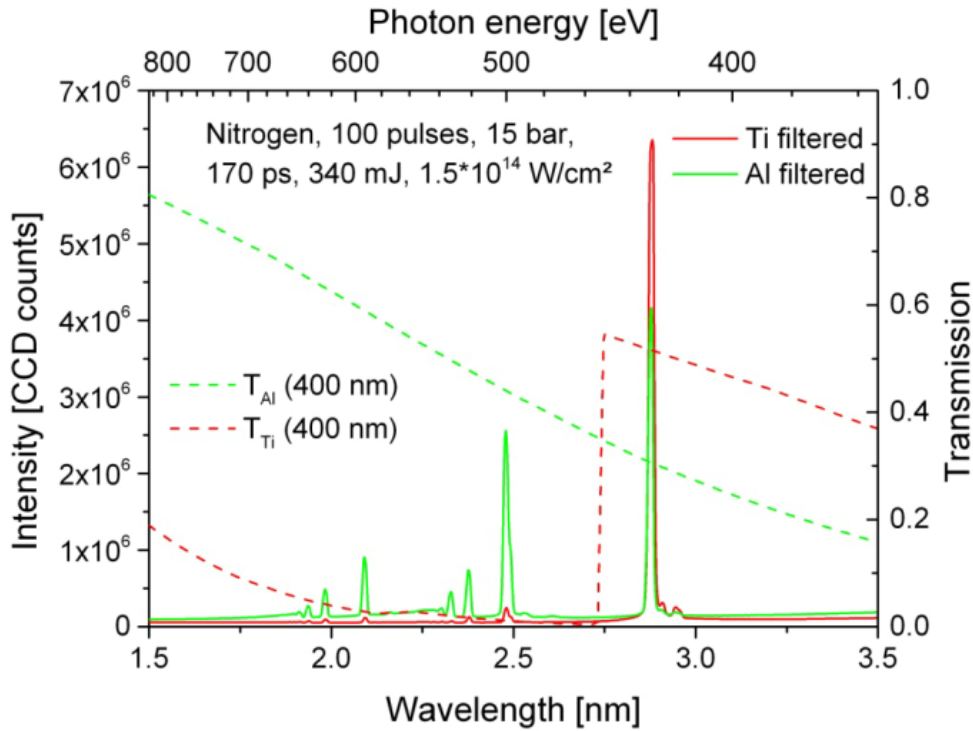


Figure 3.14: nitrogen plasma emission spectrum after filtering with (red) Ti filter and (green) Al filter as well as filter transmission spectra (dashed); 400 nm thickness each [33]

- As soon as those adjustments have been made, it is necessary to correctly position the focus by moving the focusing lens. In y direction (see figure 3.12), the plasma is always kept at a distance of $\approx 500 \mu\text{m}$ from the lower nozzle end, since the gas pulse expands with increasing distance to the nozzle. Afterwards, the position within the x - z plane is optimized with regard to the pixel count that the plasma induces on the CCD sensor.

4 Results

The results of the lab work that was carried out shall be presented within the following sections. First of all, the influence of several setup parameters is to be studied in section 4.1. Followed by that, the fabricated nozzle plates shall be characterized and compared, and their functionality shall be analyzed in section 4.2.

The complete datasets are included in an external file and in the lab book; this work contains only the relevant data.

4.1 Effects of Various Parameters on Bore Geometry

In this section, some findings about the influence of various experimental parameters on the observable bore geometries shall be presented. It has to be noted, however, that those data represent only the particular experimental setup that was used to obtain them, since they depend on very specific parameters such as the exact positioning of the components, room temperature, etc. Exchanging one lens, for example, would lead to different sets of data, and as such, the results can only be interpreted in a qualitative way.

4.1.1 Pulse Duration

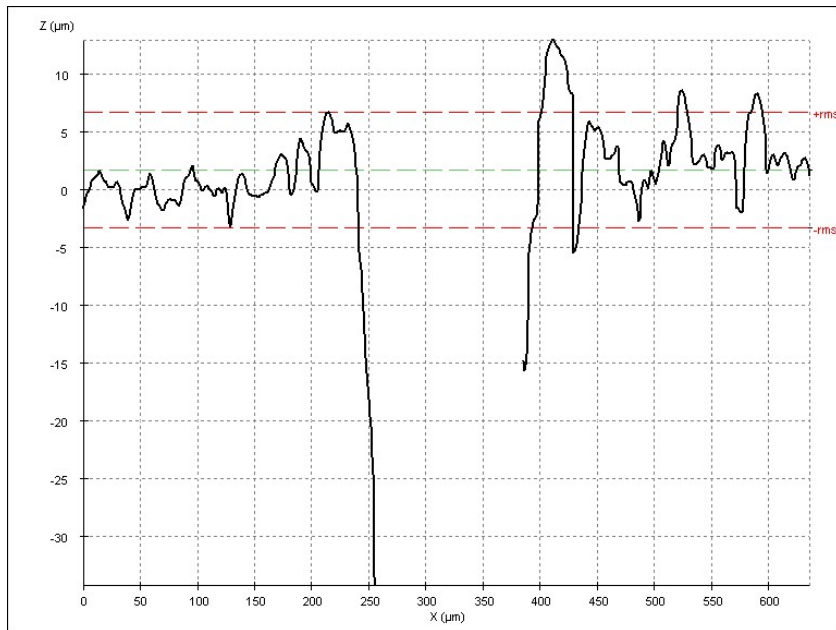
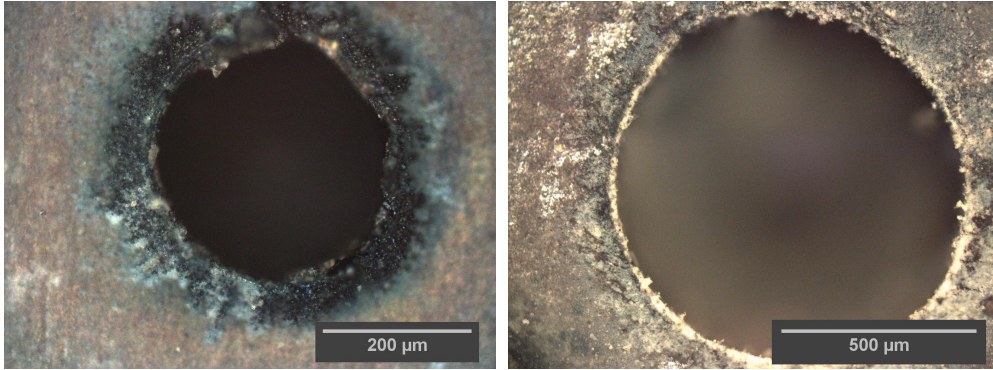


Figure 4.1: height profile through bore demonstrating crater at FS, focus placed on BS, $\tau = 9$ ns, $E_{pulse} = 30$ mJ, $\eta \approx 3000$, $f_{rep} = 100$ Hz, $N = 4000$

Since the *ps* laser specified in section 3.1.2 was available for only a short amount of time, the influence of the pulse duration could not be tested thoroughly. However, a qualitative difference could be made, which is smaller magnitude of any crater at the boundaries of the bores created by the *ps* laser, as evident from figure 4.2b. Based on the explanation in section 2.1.2, the pulse length does not allow for a significant dissipation of thermal energy, extremely limiting the size of the heat-affected zone. When considering *ns* pulse bores, however (figure 4.2a), one can clearly distinguish an area at the bore boundary that has been affected by the radiation, including some level of crystallization. A more quantitative view on a crater is enabled in figure 4.1, where at the hole boundary, a significant exaltation can be observed. When considering the flow properties of the nozzle, any rough surface includ-

ing crystallized areas and craters needs to be avoided to prevent turbulences. Nevertheless, the parameter set in the setup involving ns pulses was optimized to avoid those effects (mainly by reducing the pulse energy).

Additionally, it was found that smaller bores could be produced using the ps laser, though this might be caused by, e.g., a better beam quality, as well. Also, the parameter sets were quite different (cf. section 3.1.2), which one needs to consider when comparing the results.



(a) crater and crystallization visible at hole boundary; FS, $D_{FS} \approx 331.7 \mu\text{m}$, $\tau = 909.7 \mu\text{m}$, $\tau < 15 \text{ ps}$, $\delta = 250 \mu\text{m}$, $\alpha = 9^\circ$, $\delta = 110 \mu\text{m}$, $\alpha = 10^\circ$, $E_{pulse} \approx 10 \mu\text{J}$, $\eta \approx 8000$, $f_{rep} = 30 \text{ mJ}$, $\eta \approx 8000$, $f_{rep} = 100 \text{ Hz}$

(b) HAZ almost non-existent; FS, $D_{FS} \approx 331.7 \mu\text{m}$, $\tau = 909.7 \mu\text{m}$, $\tau < 15 \text{ ps}$, $\delta = 250 \mu\text{m}$, $\alpha = 9^\circ$, $\delta = 110 \mu\text{m}$, $\alpha = 10^\circ$, $E_{pulse} \approx 10 \mu\text{J}$, $\eta \approx 8000$, $f_{rep} = 30 \text{ mJ}$, $\eta \approx 8000$, $f_{rep} = 100 \text{ kHz}$

Figure 4.2: heat-affected zone for (a) ns - and (b) ps -pulse bores

4.1.2 Pulse Energy

As explained in section 2.1.3, the workpiece is only affected significantly once a certain power density threshold is exceeded. Exemplary beam intensity profiles are shown in figure 4.3, including a Gaussian and a top-hat profile. The used laser system outputs a top-hat profile [30], characterized by the flattened top.

While most of the pulse energy is contained within a small region around the center, a notable part is distributed along the outer ends, especially for the GAUSSIAN beam. Figure 4.3 b) illustrates the inherent advantage of top-hat beam profiles to induce a smaller HAZ. As can be guessed from figure 4.3 (a), an increase in pulse energy also increases the size of the pulse section being above the damage threshold. Hence, the affected workpiece area, respectively the bore, is larger. Although this effect is much smaller in the case of a top-hat profile, it is still significant, as can be seen in the following.

For determining the most suitable method for controlling bore diameter, the influence of pulse energy on the hole sizes on the back and front side is investigated (cf. figure 4.4). The number of pulses is chosen such that the

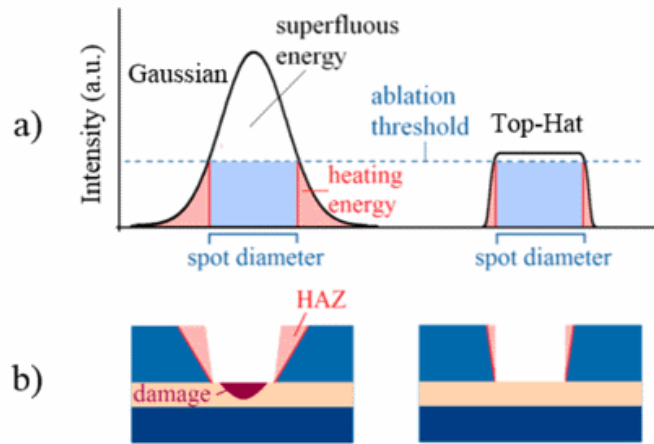


Figure 4.3: GAUSSIAN and top-hat beam profiles; a): interaction with ablation threshold, b): influence on ablation behavior, adapted from [34]

material is drilled through and the acoustically perceptible interaction of laser radiation and material ceases. Consistently, the diameter measurements represent the maximum measurable value, i.e. the major radius of an ellipse. The results confirm the previously mentioned thought that an increase in pulse energy leads to larger bore diameters. However, the observable bore diameter is subject to strong fluctuations, rendering this method unfit for regulating the diameter. Within this context, it was also investigated whether controlled defocussing could be used for bore diameter regulation. The corresponding results are depicted in figure 4.5, where a positive d corresponds to a larger distance to the target. A minimum at $d \approx 0.25$ mm can be observed, meaning that the focus is approximately at the target surface. Any motion of the lens away from this position hence leads to an increase in bore diameter. The diameter fluctuations, which may in part be caused by the strong astigmatism, do not render this method fit for application. Instead, regulation is done by varying δ , as explained in the following section.

4.1.3 Distance Between Focus and Rotational Axis

The distance δ between the laser focus on the work piece and the rotational axis, as represented in figure 3.4, is chosen as the method for diameter regulation. Keeping the other parameters constant at $\lambda = 532$ nm, $E_{pulse} = 27$ mJ, $\eta \approx 3000$, $\tau = 9$ ns, $f_{rep} = 100$ Hz, $\gamma = 7^\circ$, δ is varied from $\delta = 0$ to $\delta = 215$ μ m, and the resulting front and back diameters of the bore are recorded in figure 4.6. As can be deduced from the data points, the respective linear approximation can be used to estimate a value of δ to obtain a specified value of the frontal bore diameter. Contrarily, the back side (BS) diameter is

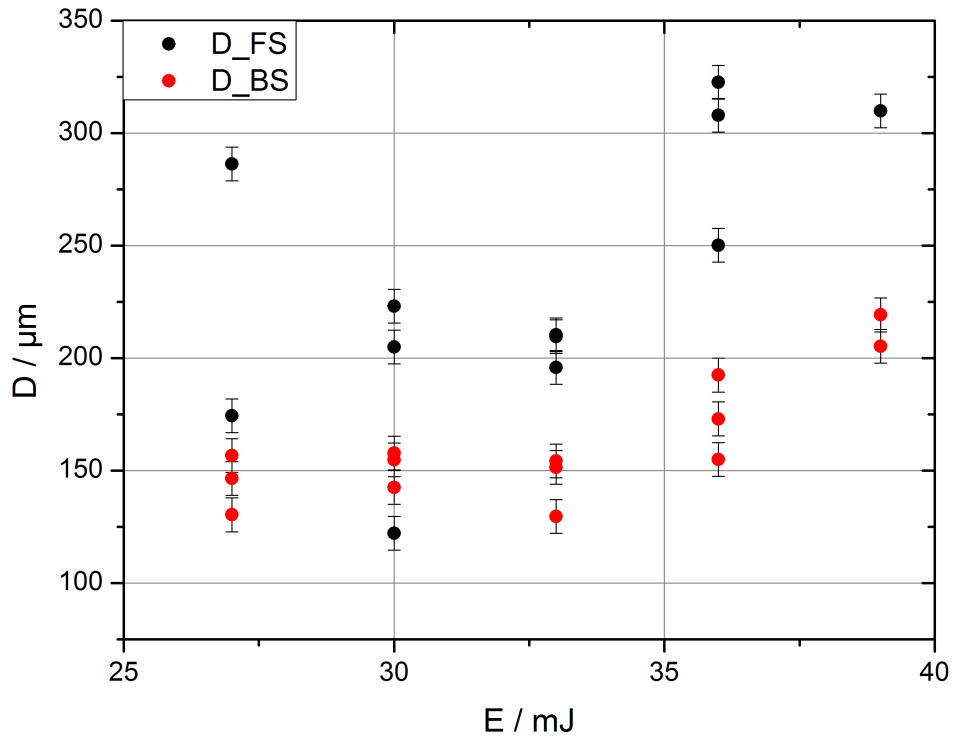
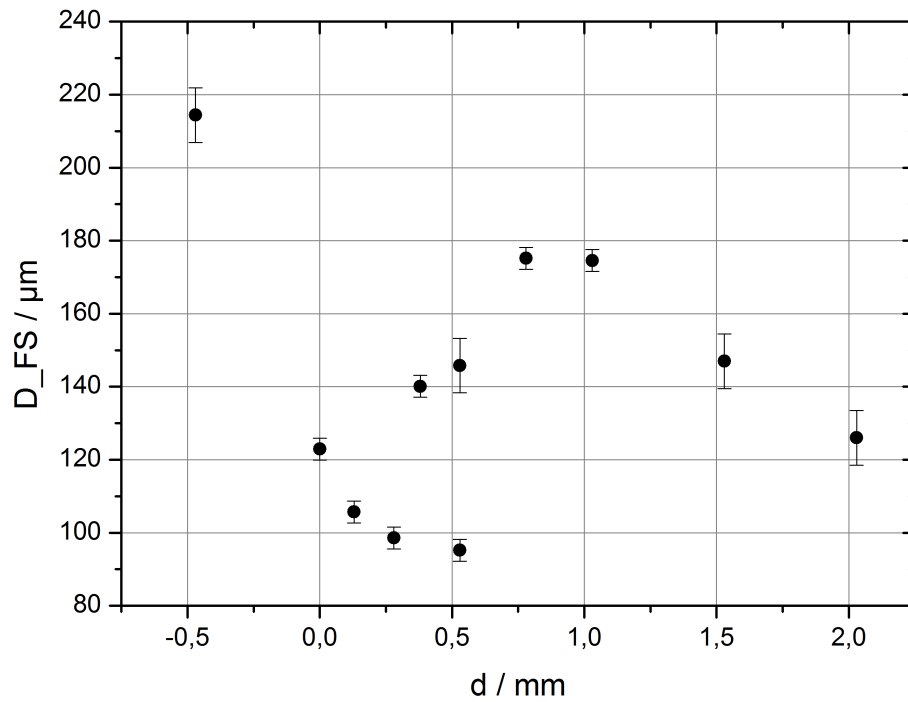


Figure 4.4: max. bore diameter (FS & BS) vs. pulse energy

Figure 4.5: max. bore diameter (FS) vs. depositioning d of the lens

subject to more heavy fluctuations, and thus cannot be determined in this way (see also the estimation of repeatability in section 3.1.2.1). One possible explanation of this is the fact that the pulse count was not controlled during this measurement due to a practical reason: The laser system enabled a controlled number of pulses only up to $N = 10^3$. Since some of the drilling processes require $N \approx 10^5 - 10^6$, many small interruptions would occur, resulting in irregular irradiation of the target. Instead, as explained in the previous section, radiation was stopped following acoustically noticeable interaction. It should be noted that the linear fit

$$D_{FS} = (2.05 \pm 0.08)\delta + (128.58 \pm 9.75) \mu\text{m} \quad (4.1)$$

describes only this specific trepanning configuration. Varying one of the other parameters, a different approximation would be necessary. However, the values presented in this case do make sense, since

- the deposition by δ inscribes a circle with radius δ around the rotational axis, thus leading to a diameter $D = 2\delta$ of this circle, manifesting in the slope of 2.05 ± 0.08 . Hence, this factor does not depend on the setup.
- the focus itself has a finite size, leading to the offset of about $129 \mu\text{m}$, even when $\delta = 0$. This size should, however, not be confused with the focal diameter, since it rather represents the HAZ, including transfer of heat to adjacent volumes.

4.1.4 Pulse Count

By increasing the amount of pulses allowed to affect the workpiece and keeping the residual parameters constant (including, especially, the beam diameter), the radiant fluence H_e and thus the energy deposited in the workpiece, is increased. However, this relation is not as trivial as it seems: If the energy (which is transferred from one laser pulse to the target) diffused before the next pulse reached the target and did not change it in any significant way, subsequent pulses would not increase the amount of energy contributing to the ablation process. In other words, consecutive pulses would not be interconnected. However, as the individual pulses cause a certain removal of material and hence change the target, they *do* affect the fluence.

In literature [35], an ablation threshold fluence $H_{thresh} \approx 0.2 \text{ Jcm}^{-2}$ is given (for a similar pulse length of $\tau_{pulse} = 20 \text{ ns}$). No fluence measurements are performed during this work, but an upper boundary can be given by taking the pulse energy E_{pulse} and the focus size $D \approx 80 \mu\text{m}$ into consideration. Hence, it is assumed that no optical energy is lost in the system, and that the focus

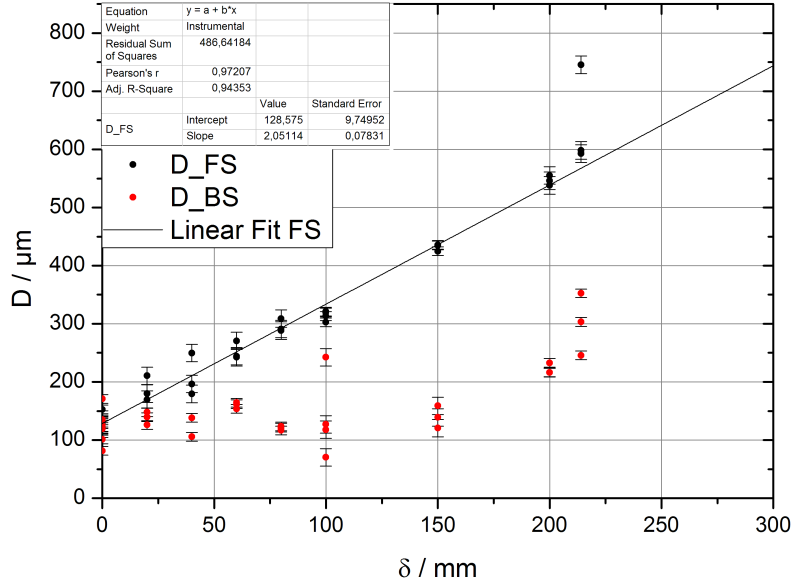


Figure 4.6: bore diameter vs. positioning of focus towards rotational axis

size does not vary. The ratio $H_e/H_{thresh} =: \eta$ is defined. In all cases, $\eta \gg 1$, meaning that every laser pulse reaching the target contributes to its ablation. In this context, it is interesting to look at the relationship between pulse count and bore depth.

One intuitively expects the depth to increase with pulse count, which it does. After a certain number of pulses depending on the process parameters, however, saturation is attained, which can be guessed from the results presented in figure 4.7. Hence, the asymptotic fits were chosen as guide for the eyes. Using the LAMBERT–BEER law, one can create a very simple ablation model which neglects many effects, but may provide adequate results in low-intensity cases. Say, ablation occurs at an intensity $I > I_S$. Equating (2.1) with I_S , one obtains the material depth after which the intensity has dropped below the threshold I_S , i.e. an estimate for the ablation depth Λ .

$$\begin{aligned}
 I_{abs}(t, z) &= I(t)(1 - R)e^{-\alpha z} \stackrel{!}{=} I_S \Leftrightarrow \\
 \frac{I_S}{I(t)(1 - R)} &= e^{-\alpha z} \Leftrightarrow \ln \frac{I_S}{I(t)(1 - R)} = -\alpha z \\
 \Rightarrow |z| &= \alpha^{-1} \ln \frac{I_S}{I(t)(1 - R)} =: \Lambda
 \end{aligned} \tag{4.2}$$

Equation (4.2) shows that the ablation depth decreases with the logarithm of the incident intensity.

Note that the saturation-effect shown in figure 4.7 appears rather weak be-

cause the plate thickness is limited, and thus the target may be drilled through before saturation is reached. Results for more pulses would show a stronger trend towards saturation, but at this time, the specimen would already be completely drilled through.

The explanation of this effect is rather simple. With increasing z -coordinate after the focus (say, $z = 0$ at the focus position), the beam diameter w' of a GAUSSIAN beam increases as follows [26]⁷:

$$w(z) = w_0 \sqrt{1 + \left(\frac{z}{z_R}\right)^2} = w_0 \sqrt{1 + \left(\frac{z\lambda M^2}{\pi w_0^2}\right)^2}. \quad (4.3)$$

Hence, the beam cross-section increases and the intensity decreases by a factor

$$\left(\frac{w(z)}{w_0}\right)^2 = \left(\sqrt{1 + \left(\frac{z\lambda M^2}{\pi w_0^2}\right)^2}\right)^2 = 1 + \left(\frac{z\lambda M^2}{\pi w_0^2}\right)^2. \quad (4.4)$$

Inserting values comparable to the experimental ones ($z = 0.5$ mm, $\lambda = 532$ nm, $w_0 = 80$ μ m, $M^2 \approx 1.7$ ([27])), the beam diameter increases from 80 μ m at the focus to 81.28 μ m after 1 mm of propagation, which may not seem like a lot, but leads to a reduction of intensity of ≈ 3.1 %. Hence, at a specific distance from the focus the threshold intensity is not overcome, the drilling process ceases functioning, and saturation is reached. This result is in accordance with those stated in literature (cf. e.g. source [36]).

Because the bore diameter is of vital importance in this work, it is also worth looking at the influence of the pulse count on said diameter. As evident from figure 4.8, also in this case a saturation limit exists. There are several possible explanations for this effect:

- Firstly, there may be a small degree of pointing instability due to irregularities in the laser system. This in turn leads to the energy being deposited over an extended area of influence, thus increasing the hole diameter.
- Intensity fluctuations may lead to varying ablation volumes per pulse.
- Furthermore, a fraction of the laser radiation may be scattered at the hole walls, randomly depositing energy.
- Energy contained in the margin of the beam profile (outer parts of figure 4.3 a), “heating energy”) additionally may stack up such that thermal effects become significant in the HAZ and increase the diameter.

⁷In practice, the beam has a top-hat profile, and hence the divergence is even larger, since for a GAUSSIAN beam it is at a minimum.

- These statistical variations add up and after a number of pulses, an asymptotic diameter is approached.

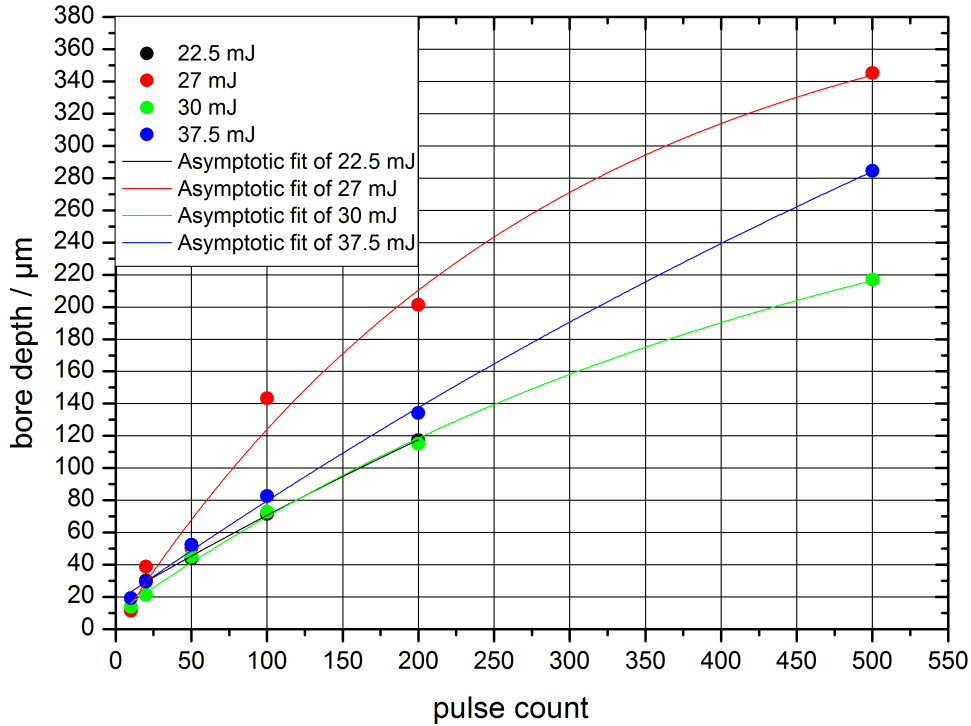


Figure 4.7: bore depth vs. pulse count at different pulse energies, asymptotic fit ($f(x) = a - bc^x$), taken with *Sensofar PLμ 2300* described in section 3.2.1

4.1.5 Goniometer Table

Although the goniometer table (see figure 3.5) has a crucial influence on the bore geometry, it is quite difficult to determine the nature of it. This is caused by the fact that for each angle setting of the table, the workpiece moves to a small degree in z -direction. Consequently, the position of the focusing lens needs to be corrected to have the focus on the target surface. Since the depth of focus is in the range of the target length (cf. section 3.1.2) and hence the beam waist does not vary heavily along the target, it is virtually impossible to recreate the situation from before the angle change. This represents a shift within the parameter space in many dimensions, making measurements at different angle positions incomparable. Furthermore, the resulting opening angle depends not only on γ , but also on the diameter of the bore. Thus, it is virtually impossible to determine the goniometer table angle γ necessary for a specific opening angle θ . Instead, it needs to be determined experimentally for each desired nozzle geometry. The values in accordance with the nozzles produced in this work can be used as a guideline for this setup.

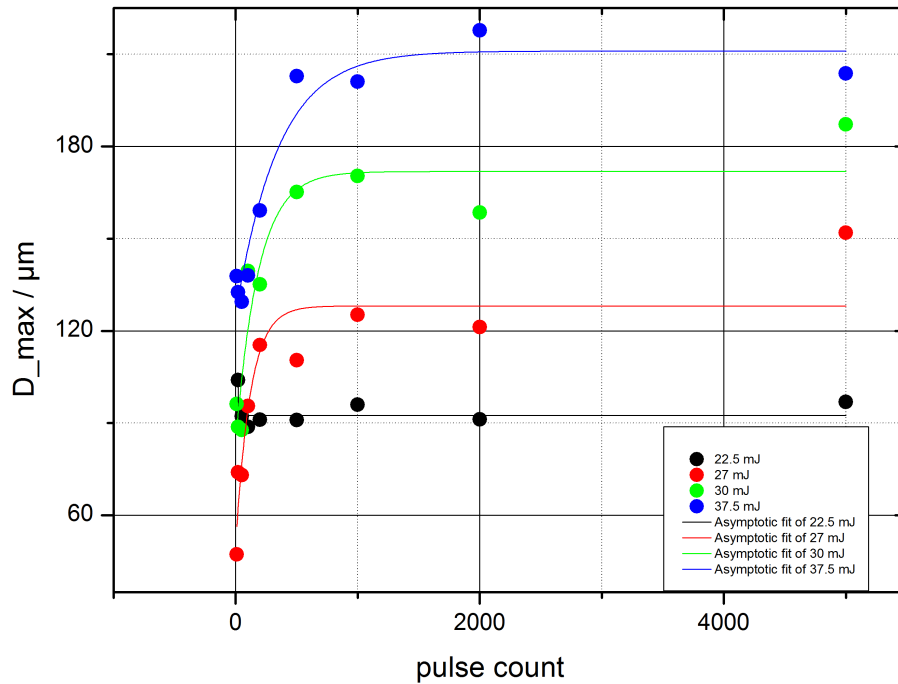


Figure 4.8: maximum measurable hole diameter vs. pulse count at different pulse energies, asymptotic fit, taken with *Sensofar PLμ 2300*

4.2 Quality Assessment

Within this section, the quality of the fabricated nozzles is discussed in respect to several aspects, starting with the superficial visual quality, continuing with a look at gas flow properties, and finishing with the actual produced plasmas. An overview in this respect is given in figure 4.15 and table 2. For a more detailed view on the nozzle data, see the data disc.

4.2.1 Visual Bore Quality

First of all, the nozzles are compared on a visual level, i.e. using topographies and microscope images (*Carl Zeiss Axioskop2*). Obviously, only a small selection of bores can be displayed in this work, each representing the general character. For full disclosure, it is referred to the data disc.

4.2.1.1 Percussion Drilling

Most bores produced using percussion drilling were investigated utilizing confocal topography measurements described in section 3.2.1. One inherent disadvantage is this method's maximum scanning depth of $300\ \mu\text{m}$, which does not allow for the correct acquisition of surfaces comprising height differences of more than this value (these areas are depicted black).

The theoretical disadvantages of percussion drilling stated in section 3.1.1 become obvious when looking at figure 4.9. The appearance of the focus determines the shape of the bore, which points to a high degree of astigmatism, possibly caused by misalignments in the setup. Quite interestingly, the bores feature outer rings following the structure of the focus. Those may indicate additional transversal modes radiated by the laser (i.e., multiple radial mode orders), posing an additional source of imprecision. Furthermore, a method to regulate the opening angle of the bores is not available with percussion drilling. Although it can be influenced by controlledly defocussing the beam to some extent, this extent is nowhere near large enough.

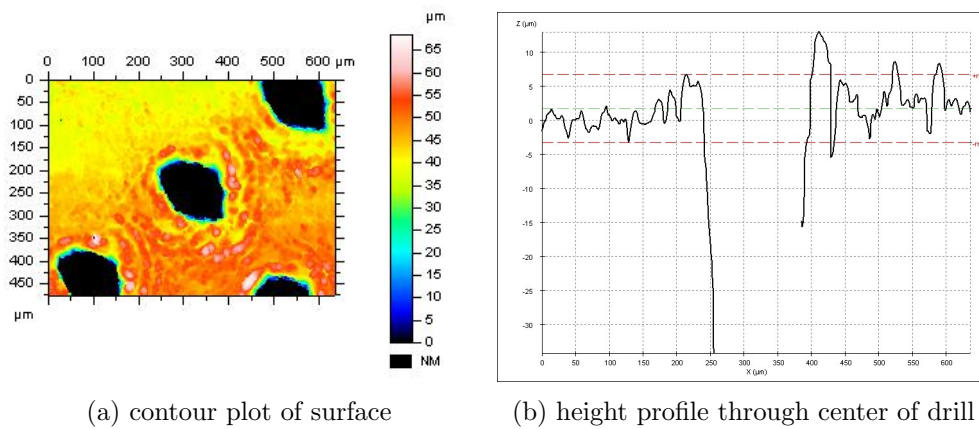
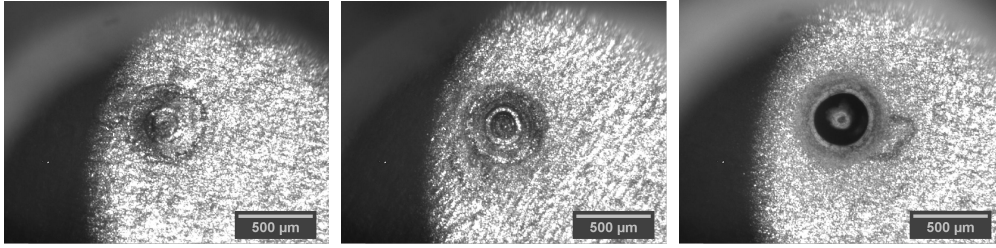


Figure 4.9: percussion sample surface, FS, focus placed on BS, $\tau = 9$ ns, $E_{pulse} = 30$ mJ, $\eta \approx 3000$, $f_{rep} = 100$ Hz, $N = 4000$

4.2.1.2 Trepanning

Since it became obvious immediately that for the completion of the tasks, a more sophisticated approach would be necessary, the major part of the time was spent studying trepanning. The rotational motion reduces the impact of the focus shape, as anticipated in section 3.1.2.

The three process steps involved, which are discussed in section 3.1.2, are depicted in figure 4.10, from which the much more circular geometry can already be guessed.



(a) phases 1 & 2: determination of D_{HAZ} after lining up of rotational and optical axis
 (b) phase 3: trepanning, after five revolutions
 (c) still phase 3: trepanning, after many revolutions, cone not fully cut out yet

Figure 4.10: trepanning process as seen in-line, $\tau = 9$ ns, $E_{pulse} = 30$ mJ, $\eta \approx 3000$, $f_{rep} = 100$ Hz, $\alpha = 11^\circ$, $\delta = 50$ μ m

The first two phases summarized in figure 4.10a are preparatory. First, the optical and rotational axes have to be aligned so that $\delta \approx 0$ μ m. Afterwards, the minimal diameter of the HAZ can be determined by irradiating the target with a small number of pulses and measuring the diameter of the affected area. The trepanning can then be initiated (phase 3) by detaching the optical from the rotational axis (as described by δ) and irradiating the rotating target. Figures 4.10b and 4.10c show the target after 5 and a few hundred rotations, respectively. Take into account the “island” in the middle of the bore in the progressed state, illustrating that trepanning indeed is a cutting and not a drilling process. This island can be used to help characterize the bore walls, as explained further below.

Figure 4.11 shows an exemplary trepanning bore with a high level of roundness. Its dependence on the goniometer table γ was identified at a late stage of the work: It seems that after a certain threshold angle γ_{thresh} , bore roundness is reduced by the introduction of irregularities at the margin. A possible explanation for this is the reflection of incident radiation (especially of transversal modes) at the walls near the beginning of the bore. This explanation is supported by the fact that those irregularities predominantly occur on the front sides of the respective bores. An example is given in figure 4.12. Possible influences of this aspect are discussed in the following two sections 4.2.2 and 4.2.3.

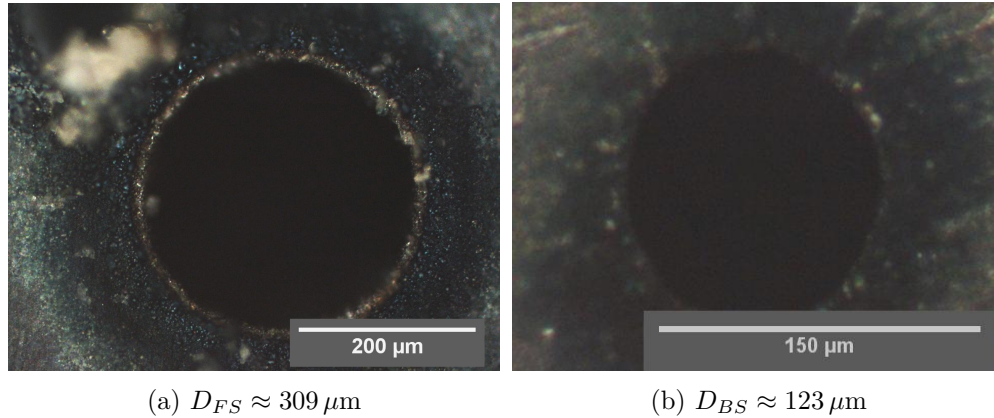


Figure 4.11: example of drill from FS and BS, $\tau = 9 \text{ ns}$, $E_{pulse} = 27 \text{ mJ}$, $\eta \approx 3000$, $f_{rep} = 100 \text{ Hz}$, $\gamma = 7^\circ$, $\delta = 80 \mu\text{m}$, $\theta \approx 5.3^\circ$

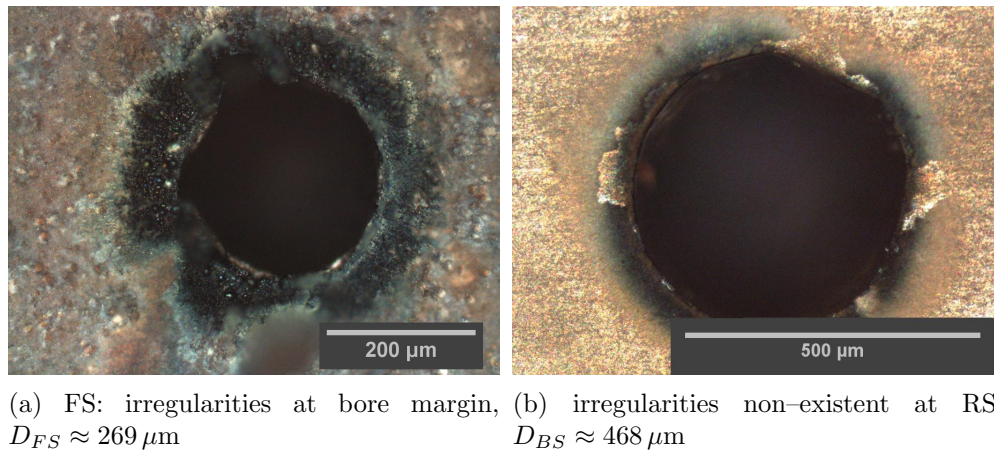


Figure 4.12: example of impaired bore margin, $\tau = 9 \text{ ns}$, $E_{pulse} = 30 \text{ mJ}$, $\eta \approx 3000$, $f_{rep} = 100 \text{ Hz}$, $\gamma = 14^\circ$, $\delta = 80 \mu\text{m}$, $\theta \approx 11.3^\circ$

Since trepanning represents a cutting process, each bore exhibiting a sufficient diameter has a corresponding cut-out cone. Reflections at this cone may add to the previously discussed irregularities at the margin. The cone can be used to investigate the structure of the bore walls. The example given in figure 4.13 is representative of the trepanning bores. As can be identified, the cone has a mostly flat surface imprinted with longitudinal lines. Since the number of pulses has the order of magnitude $N \approx 10^4$, it is improbable that the individual lines originate from single pulses. Instead, they may be caused by an uneven spatial energy distribution analogous to ripple formation due to interference effects (cf. section 4.2.1.3), or they may reflect inhomogeneities of the wolfram target.

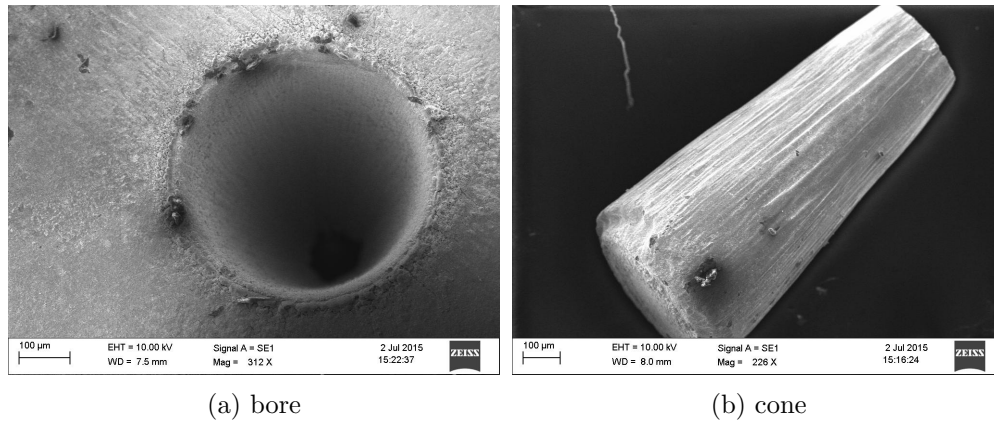


Figure 4.13: scanning electron microscope image of bore (a) and associated cut-out cone (b), $D_{FS} \approx 501 \mu\text{m}$, $D_{BS} \approx 110 \mu\text{m}$, $E_{pulse} \approx 52.5 \text{ mJ}$, $\eta \approx 5000$, $f_{rep} = 100 \text{ Hz}$, $\delta = 214 \mu\text{m}$, taken with Zeiss EVO MA10

4.2.1.3 Plate-Cutting

To demonstrate the possibility of doing all necessary process steps with the trepanning setup, it is shown that wolfram plates can be cut from raw material. In the attempt shown in figure 4.14, a plate with half the diameter of the desired nozzles was produced, demonstrating the capability to fulfill this task. However, as a relatively large amount of time is necessary to cut even a plate as small as this one, it is decided that this process is outsourced to an external company.

On the front side of the plate, the HAZ can clearly be identified, involving a small degree of crystallization (cf. figure 4.14b). This inhomogeneity can be removed without a lot of effort by merely scraping it off with, e.g., a screwdriver, thus posing no serious problem.

Ripple formation is discernible on the back side of the plate (figure 4.14d), exhibiting a regular pattern with a periodicity of about $50 \mu\text{m}$. In literature, this is a well-known effect occurring at the workpiece surface, caused by the interference of incident radiation and light scattered at the specimen surface, inducing an uneven distribution of energy deposition [5]. In this case, however, it occurs on the back side of the specimen. A possible explanation is interference of sections of the light beam being reflected at different hole surface areas, leading to some path difference. Definitive explanation of this effect requires computer simulation. It has no influence on the quality of the nozzle plates, since the gas jet does not come into contact with the outer margin in the scope of the experiment (as can be seen in figure A.15).

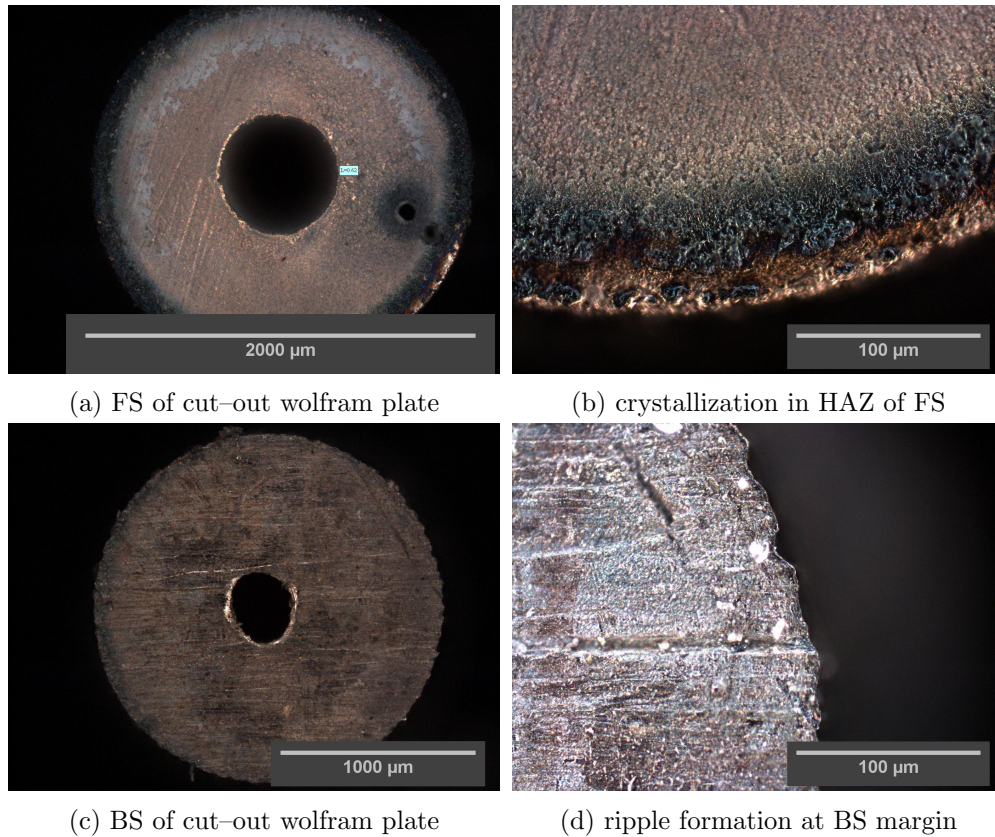


Figure 4.14: plate cut out from raw material, $\tau = 9$ ns, $E_{pulse} = 27$ mJ, $\eta \approx 3000$, $f_{rep} = 100$ Hz, $\gamma = 7^\circ$, $\delta = 1$ mm

4.2.2 Gas Flow Quality

The quality of the gas flow in this work is qualitatively defined by

- the widening
- the maximum density
- the overall gas quantity

of the exiting gas jets. Those are quantified utilizing the methods described in sections 3.2.2 and 3.2.3. An overview of the Schlieren measurements is given in figure 4.15. In this section, a small collection of striking examples is examined in more detail. The larger one of both nozzle openings always points towards the plasma, i.e. into the direction of the gas flow.

See table 2 and figure 4.15 for an overview of all significant nozzle plates (ranked by their corresponding plasma emission); for a more detailed view on all the measured nozzles, see section A.2. The first column shows the measurement of the radiated energy within the water window in terms of triggered CCD counts. Notice that the bore photographs depicted in the

third and fourth column are not scaled equally, i.e. they cannot be used for size comparison.

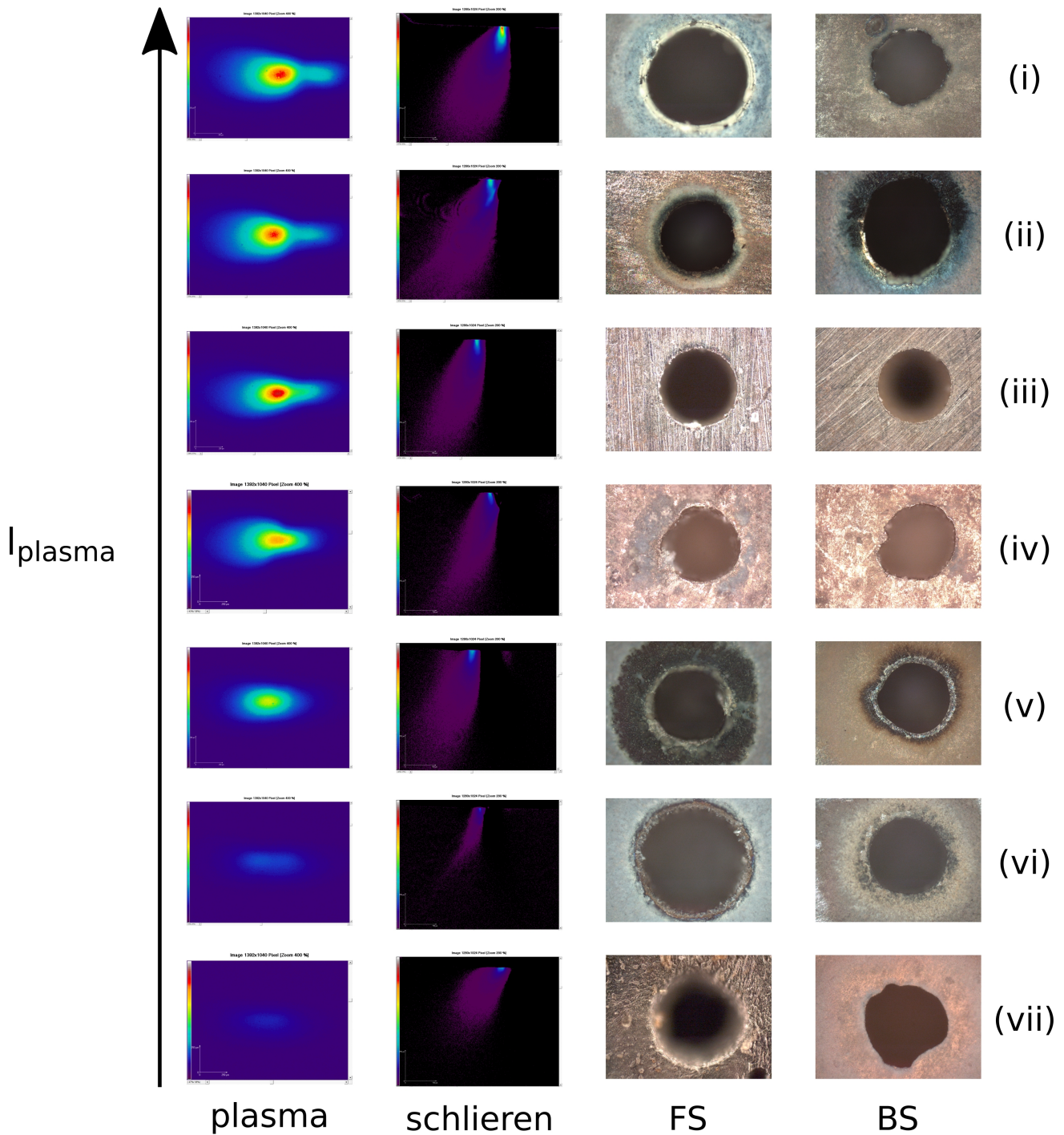


Figure 4.15: overview of significant nozzles (i)–(vii), rows ranked by plasma emission, more details in table 2 and section A.2

Nozzle	(i)	(ii)	(iii)	(iv)	(v)	(vi)	(vii)
l/mm	1	0.5	1	1	1	0.5	1
$D_{FS}/\mu m$	400	380	314	302	281	309	346
$D_{BS}/\mu m$	555	556	567	555	541	441	386
A_{FS}/mm^2	0.128	0.239	0.077	0.068	0.076	0.075	0.075
A_{BS}/mm^2	0.241	0.106	0.252	0.265	0.256	0.086	0.081
$\theta/^\circ$	4.4	9.9	7.2	7.2	7.4	7.5	1.2
$I / MCts$	56.47	55.59	49.48	47.42	31.87	13.61	8.99
$FWHM_x/\mu m$	378.9	364.7	368	465.4	391.6	689.8	591.6
$FWHM_y/\mu m$	230.7	229.9	192.6	205.5	220.3	238.5	268.1

Table 2: data corresponding to the nozzles presented in figure 4.15⁸

Nozzle	(i)	(ii)	(iii)	(iv)	(v)	(vi)	(vii)
$\Delta D_{FS}/D_{FS,(iii)}$	27.4	21.0	0	-3.8	-10.5	-1.6	10.2
$\Delta D_{BS}/D_{BS,(iii)}$	-2.1	-1.9	0	-2.1	-4.6	-22.2	-31.9
$\Delta A/\max(A_{FS}, A_{BS})$	46.8	55.8	69.4	74.5	70.3	13.1	7.6
$\Delta\theta/\theta_{(iii)}$	-38.9	37.5	0	0	2.8	4.2	-83.3
$\Delta I/I_{(iii)}$	14.1	12.3	0	-4.2	-35.6	-72.5	-81.8
$\Delta FWHM_x/FWHM_{x,(iii)}$	3.0	-0.9	0	26.5	6.4	87.4	60.8
$\Delta FWHM_y/FWHM_{y,(iii)}$	19.8	19.4	0	6.7	14.4	23.8	39.2

Table 3: relative differences of values contained in table 2 when compared to reference nozzle (iii); all values are given in %

First of all, a reference nozzle (iii) is characterized, acting as a standard against which the lab-made nozzles need to compete. This nozzle was produced using wire erosion. To obtain comparable measurements, it has not been used in a plasma-generating setup before, avoiding potential damages caused by any plasmas in the close proximity.

Wavefront distortions and a Schlieren image caused by gas pulses through this nozzle are represented in figure 4.16. The Schlieren image provides information merely on a qualitative level. The optical path length is influenced by the refractive index $n(\rho)$ — a function of gas density — as well as the gas pulse extension. As such, no statement can be made about the absolute values of $n(\hat{r})$, but only about a combination of $n(\hat{r})$ and the gas pulse volume.

The wavefront distortion measurement can be used to obtain a density distribution, as explained in section 3.2.3. Within the available time, the provided Mathematica script could not be modified to work. Hence, no density distribution could be calculated such that the measurements provide only qualitative information. Nevertheless, sufficient data can be obtained from the plasma

⁸CCD Cts acquired within area of interest (AOI) of size 2.91 mm²; FWHM determined with software “MrBeam”; bore areas estimated by counting the corresponding pixels and multiplying that number with the object area that is represented by one pixel

analysis in section 3.2.4.

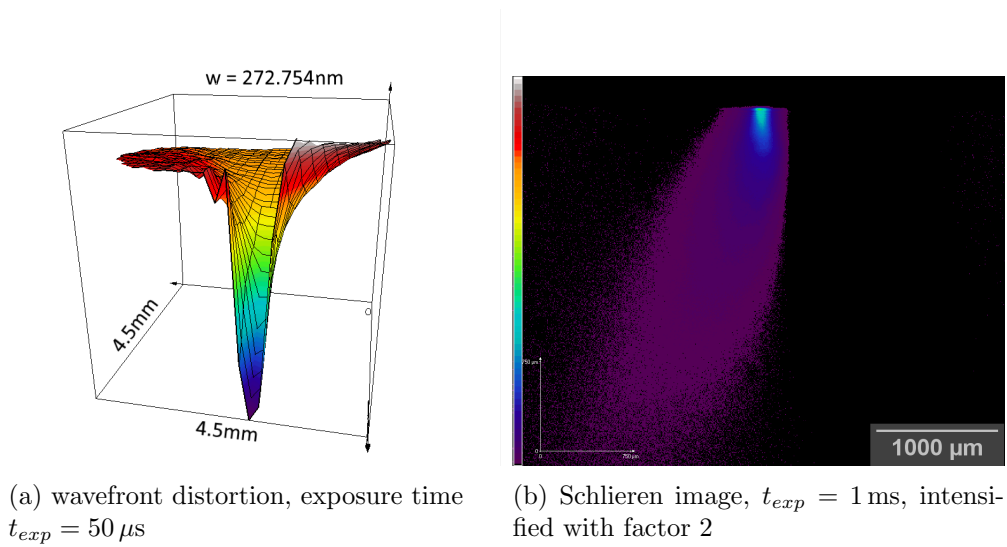


Figure 4.16: reference nozzle (iii) gas flow, $p_{N_2} \approx 19 \text{ bar}$

The shape of the gas flow produced by nozzle (i), i.e. the one producing the highest signal in the plasma measurement, looks rather similar, with the difference of possessing a larger opening angle, as can be seen in figure 4.17. Additionally, the image is significantly brighter especially at the nozzle exit, hinting at greater gas density. The wavefront analysis can, in this case, only be considered a qualitative comparison, since the measurements were conducted using different cameras and hence, the absolute values of the wavefront distortion indicated by w may deviate.

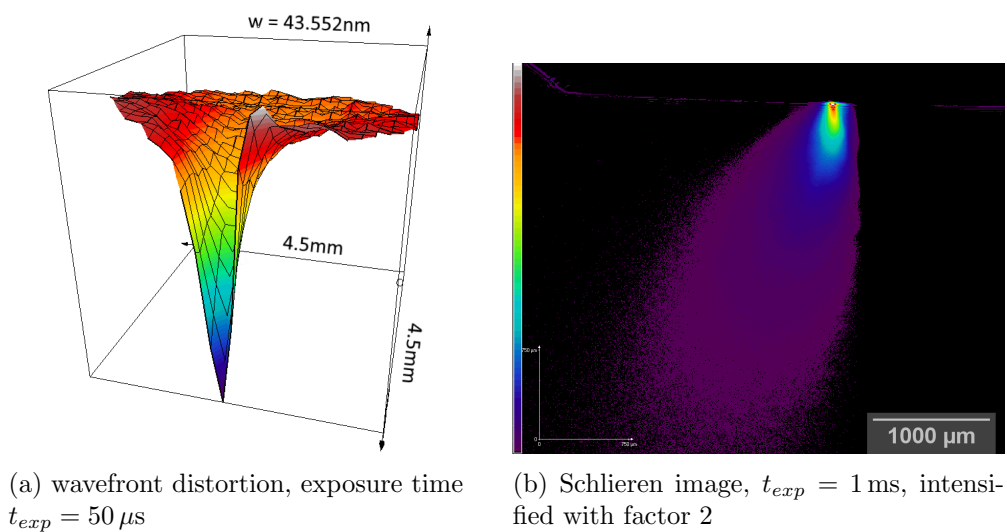


Figure 4.17: nozzle (i) gas flow, $p_{N_2} \approx 19 \text{ bar}$

In the Schlieren image corresponding to nozzle (ii) (see figure 4.18), the shape is not as homogeneous, and a small disturbance can be observed close to the nozzle exit (at the top of the image). Since no significant geometrical anomalies (e.g. craters, elevations) are visible at the nozzle surface (see microscope images 4.18c and 4.18d), a possible explanation for this are irregularities at the inner nozzle surface causing turbulences.

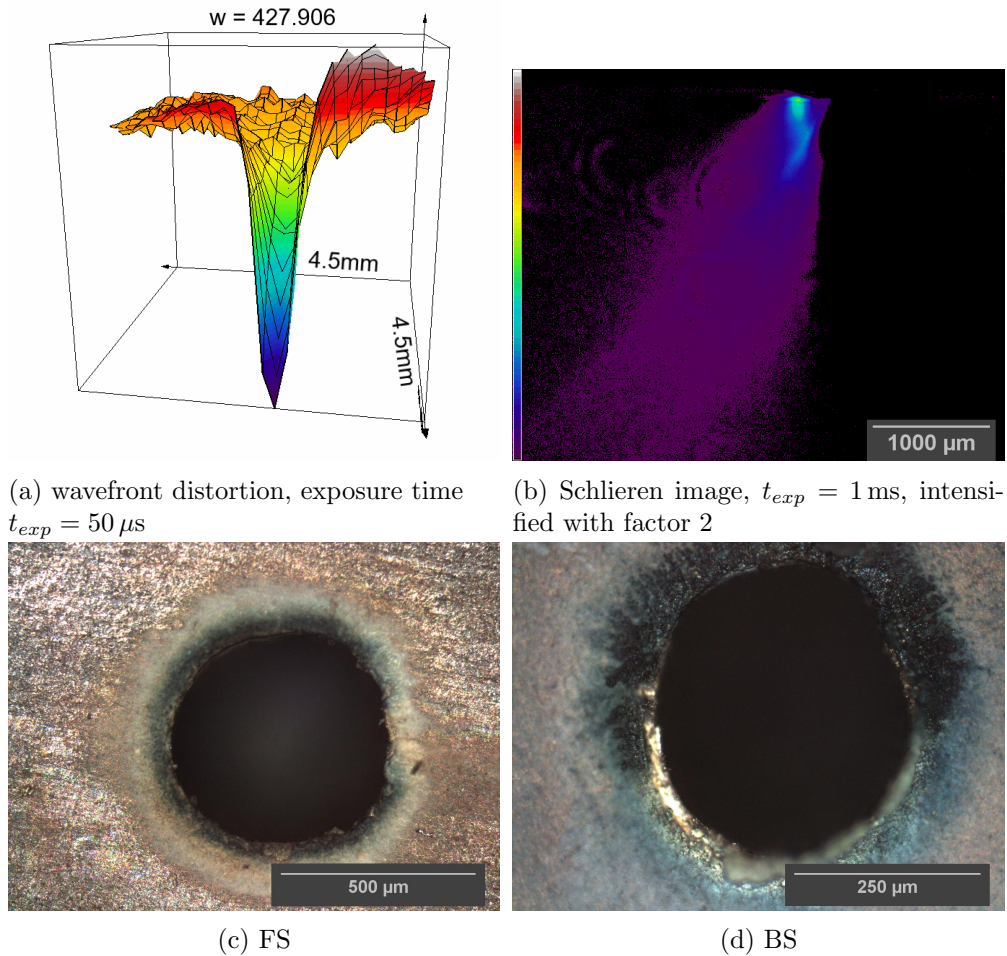


Figure 4.18: nozzle (ii) gas flow and surface images, $p_{N_2} \approx 19 bar$

Nozzle (iv), which features geometric properties very similar to the reference nozzle, produces a gas flow that shows similarity, as well, concerning its opening angle as well as the Schlieren image brightness. There is, however, an anomaly that can be seen at the top right hand part of the gas pulse. This may be caused by the irregularity that is observable at the left hand side in figure 4.19d, inducing a reflection of a part of the gas pulse, resulting in this specific shape. The matching wavefront deformation measurement (figure 4.19a) did not produce any reasonable result, presumably due to an error in measurement, e.g. wrong trigger timing. The deformation recognizable at the

front is merely evoked by the nozzle itself. However, since the measurement is of no vital importance and it was recognized as being flawed only at the end of the work, it was not repeated.

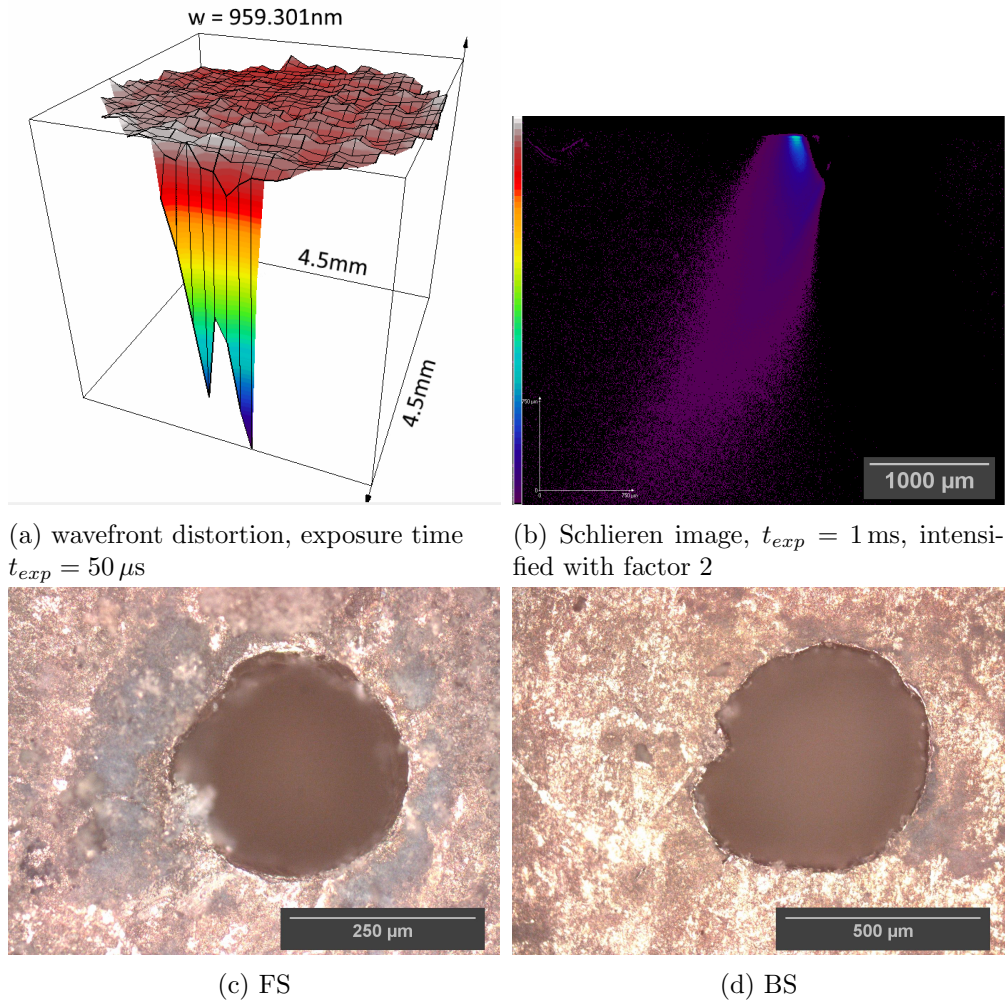


Figure 4.19: nozzle (iv) gas flow and surface images, $p_{N_2} \approx 19 bar$

Nozzle (v) comprises smaller diameters at a comparable angle, as compared to the reference nozzle. A look at both, the wavefront and the gas flow, does not show any significant differences apart from the slightly smaller brightness in the Schlieren image, indicating a plasma with less emitted radiation.

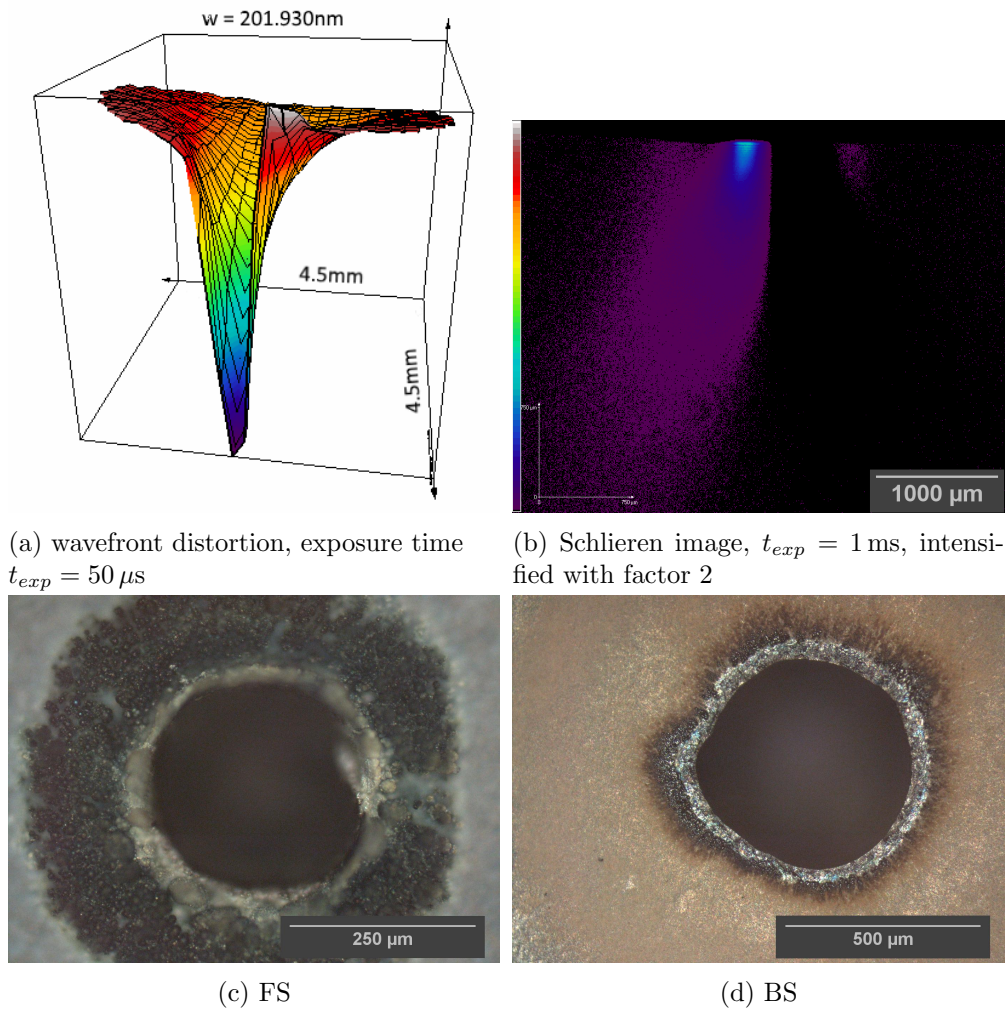


Figure 4.20: nozzle (v) gas flow and surface images, $p_{N_2} \approx 19 \text{ bar}$

Nozzle (vi) demonstrates the necessity of a sufficiently large exit diameter. The gas flow is quite directed, as figure 4.21b demonstrates, but it is assumed that the gas flow is not adequate for a bright plasma (within the water window) to be induced. Hence, also including the other results, it can be estimated that the exit diameter should not fall below $500 \mu m$ to enable sufficient gas discharge.

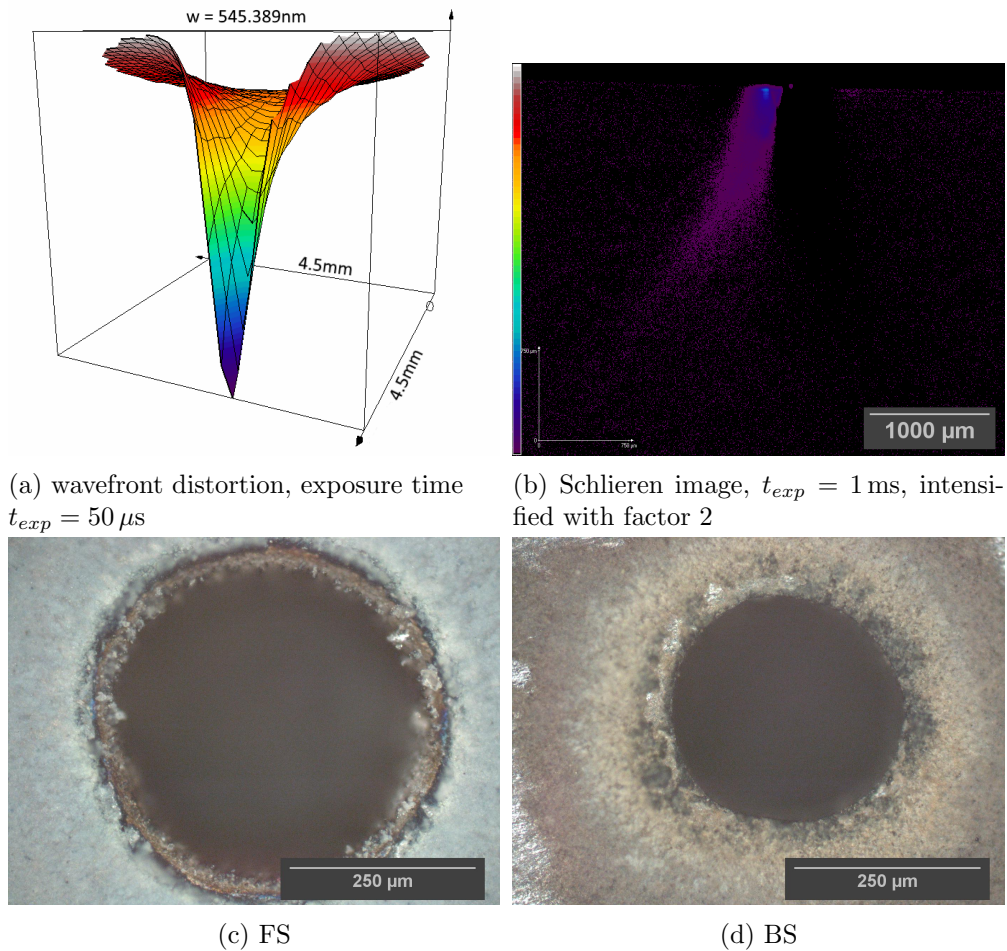


Figure 4.21: nozzle (vi) gas flow and surface images, $p_{N_2} \approx 19 \text{ bar}$

Last, the behavior of nozzle (vii), which has a quasi-cylindrical geometry and thus a small opening angle, is presented (figure 4.22), where also the gas flow is compared to that of the best-performing nozzle (i). It is surprising to see that the broadness of the corresponding gas flow is comparable to the other instances, since one would expect a more directed flow, as can be seen for nozzle (vi). In this context, notice the geometrical irregularity at the back side of the nozzle (figure 4.22d). One distinction can, however, be made to the other examples. When looking at the region of the nozzle exit, a much wider emission can be observed, i.e. the gas flow originates from a much larger area, caused by the small opening angle. The effect this has on the plasma is to be determined in the following chapter.

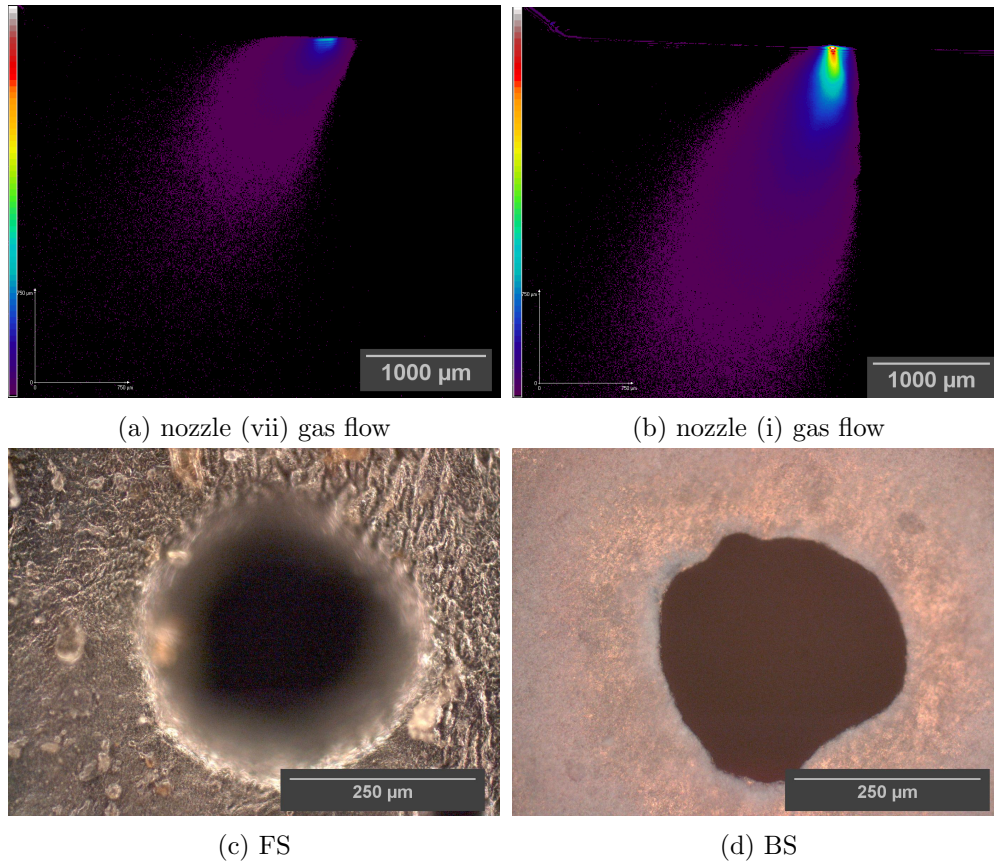


Figure 4.22: nozzle (vii) gas flow as compared to nozzle (i), surface images of (vii), $p_{N_2} \approx 19$ bar

4.2.3 Plasma Quality

The quality of the plasmas created when various nozzles are applied is object of this section. The plasma is qualitatively defined through its shape, size and, here most important, emitted energy. Measurements are conducted using the setup explained in section 3.2.4.1. Note that each presented plasma image is an average over 100 measurements such that the nozzle characteristics can be obtained with smaller dependence on fluctuations. See table 2 and figure 4.15 for an overview of all significant nozzle plates (ranked by their corresponding plasma emission); for a more detailed view on all the measured nozzles, see section A.2.

A closer look is taken at the reference nozzle (iii). The emission is spread over a rather large area and exhibits a trail towards the left hand side. The margin is rather diffuse, indicating significant expansion of the plasma during exposure. The total count gathered within an area of interest (AOI) of size $A_{AOI} = 2.91 \text{ mm}^2$ is $I_{(iii)} = 49.48 \text{ MCts}$. This size was chosen for all measurements of this type so that significant plasma emission (where the CCD counts exceed the noise) is included, and comparison between the different nozzles

is enabled. This value is obtained using the software “MrBeam”, which integrates over the gray values of the corresponding pixels.

Nozzle (iv) possesses rather similar geometric properties. Although neither the CCD count nor the general shape of the produced plasma exhibits any significant differences, the radiated energy within the center of the plasma is slightly smaller. This is supported by the measured *FWHM*: As can be seen in table 3 — containing the relative differences to the reference nozzle — the *FWHM* in x -direction is about 26.5% larger. Since it would be ideal to have the plasma as a point source, i.e. all the energy radiated from a volume as small as possible, a larger *FWHM* leads to a lower performance. This difference might be insignificant in practice, which still needs to be tested. One important deduction that can be made here is the insignificance of small deviations from a circular hole geometry, as exhibited by this nozzle (see the small indentation at the BS of nozzle (iv), figure 4.15).

Next in line is nozzle (v), which, again, shows a similar geometry as the reference nozzle, with both holes being slightly smaller. However, this slight decrease seems to have a large effect on the plasma emission, which drops by more than a third.

Nozzle (vi), the first treated nozzle plate with length $l = 0.5$ mm, is aimed at having the same opening angle θ and entrance hole diameter as the reference nozzle, which is fulfilled with small deviation. Probably caused by the much smaller exit hole, the plasma emission is reduced by about 72.5%.

A quasi-cylindrical nozzle (vii) gives the worst plasma emission in this comparison and points at the necessity of a sufficiently large opening angle. Taking a look at the *FWHM* in both directions x and y also shows a surprising increase in the size of the radiating volume. One would expect to have a more directed gas flow, and hence a more concentrated plasma emission, since the cylindrical nozzle shape restricts the widening of the flow. Obviously, this is not the case. For the corresponding gas flow analysis, see the previous section. The plasma-sided opening of the next nozzle, (ii), is kept at the same level as the reference. At the same time, both the opening angle and the entrance hole are larger, at a length of $l = 0.5$ mm, ultimately leading to a more intense plasma. Nevertheless, a look at the plasma *FWHM* exposes some increase in plasma spread, the significance of which has yet to be determined.

The most promising results are provided by nozzle (i), which shows a similar increase of plasma spread as the one before, but in exchange, an increase in CCD counts of 14.1% is supplied. This broadening fits the result of the Schlieren analysis in the previous section, where the gas flow is qualitatively shown to be wider than for the reference nozzle.

In general, the shape of the produced plasmas is very similar to the reference plasma for nozzles (iv) to (i).

5 Conclusion

In the present work, it is shown that wolfram nozzle plates used for the production of radiation in the water window ($2.3 \text{ nm} < \lambda < 4.4 \text{ nm}$) can be produced with a simple optical setup involving a pulsed Nd:YAG laser source. With this respect, it is determined that trepanning is by far a more suitable production method than percussion drilling. Furthermore, the influence of various setup parameters such as pulse duration, pulse energy and the number of pulses are studied to enable production of nozzle plates with the desired geometrical properties. The quality of those plates is examined with several regards: An optical microscope and a confocal surface profiler are used to assess the nozzle surface geometry. With a Schlieren setup as well as a wavefront distortion measurement setup involving a HARTMANN–SHACK sensor, the gas flow properties of the nozzle plates are measured. Finally, the nozzles are characterized in relation to the shape and the radiated energy within the water window of the plasmas that are induced in gas pulses passing the nozzles. The findings are briefly reported below.

- The constructed optical setup is capable of producing wolfram nozzles of a large variety of geometries, some of which perform better in producing bright plasmas than the reference nozzles. However, due to the dependence on a whole set of parameters, the problems described in section 3.1.2.1, as well as material inhomogeneities, large deviations on the hole diameter on the back side of the nozzle, i.e. the bigger hole, occur. Hence, to obtain one desired geometry it is necessary to try more than one to get better statistics.
- While the Schlieren technique is able to provide a basis for qualitative estimations of nozzle performances (especially estimating the width of the plasma emission) and thus can be used for preliminary rejection of poor nozzles, the plasma itself needs to be analyzed more carefully to enable detailed comparison.
- One very important realization is that the shape of the nozzle holes and the deviations from a perfectly circular geometry caused by the optical setup, do not significantly decrease the resulting plasma brightness (radiated energy within the water window measured within $t_{exp} = 10 \text{ ms}$).

- A condition that indeed has a distinct influence on plasma brightness is the exit hole diameter, which should not be smaller than an estimated value of about $500\ \mu\text{m}$.
- Cylindrical nozzles incorporating opening angles $\theta \approx 0^\circ$ perform poorly, hinting at the condition that there exists an optimal angle. However, no exact value for this angle can currently be given.
- There are well-performing nozzles with both lengths $l = 0.5\ \text{mm}$ and $1\ \text{mm}$, indicating that, within some region, the length plays an insignificant role as compared to opening angle and hole diameters. It is, however, difficult to compare nozzles of different lengths, since it is not clear which parameters need to be equal to allow comparison. An indication is given by the relatively bad performance of nozzle (vi), assigning the size of the hole diameters a more important meaning than the opening angle. It can be assumed that, to some extent, a shorter nozzle may prove to be better, since there is less wall-flow-interaction, reducing the chance of turbulences.

6 Outlook

Although no optimal nozzle parameters were found, this work is able to provide good insight and point into the right direction. In this context, further analysis needs to be carried out, e.g. increasing the entry hole size, or testing other nozzle shapes (such as DE LAVAL nozzles). A reduction of workload could be achieved by simulating the gas flow through different nozzle types with suitable software suits, and thus choosing the geometry more systematically.

The trepanning setup can be optimized in several ways. First of all, the laser system could be exchanged. With this respect, a combination of better beam quality (smaller M^2) and a smaller wavelength (e.g. in the UV range as provided by some excimer lasers) may improve precision. Utilizing ultrashort pulses might also prove beneficial, though the size of the HAZ does not seem to be the limiting factor in this work range.

The largest and most practical enhancement could be achieved by further improving the involved mechanics. With this regard, both the system enabling workpiece rotation as well as the mounting device need to be modified to enable trepanning in a more stable way. Especially, one needs to be mindful of constructing the mounting device in a way that renders processing with large goniometer table angles possible without cutting off a section of the beam.

Another point of investigation is the optical setup itself. The telescope could be exchanged by a more complex, more efficient variant. Also, one could improve beam quality by use of a pinhole as a low-pass filter to cut off higher-order transversal modes in order to achieve a smaller and more homogeneous focus. The resulting reduction of beam power reaching the workpiece would not be a major problem, since only small pulse energies have been harnessed, anyway.

7 Acknowledgement

At this point, I want to express my utmost gratitude to everyone who supported me during this work. First and foremost, this is directed to my supervisors

Dr. Klaus Mann, who enabled working at the Laser-Laboratorium Göttingen and provided profound ideas,

Prof. Dr. Ulrich Teubner, who put me in contact with the LLG and acted as the facilitator between Oldenburg/Emden and Göttingen, as well as

Matthias Müller, who motivated me and pushed me further as well as spending a lot of time proofreading this thesis.

Also, I am grateful to the research group Optik/Kurze Wellenlängen, who extended a warm welcome to me. Last but not least, I owe my parents thanks, since this operation would obviously not have come about without their impact.

References

- [1] Carolyn A. Larabell and Mark A. Le Gros. X-ray tomography generates 3-D reconstructions of the yeast, *saccharomyces cerevisiae*, at 60-nm resolution. *Molecular biology of the cell*, 15(3):957–962, 2004.
- [2] W. Meyer-Ilse, D. Hamamoto, A. Nair, S. A. Lelievre, G. Denbeaux, L. Johnson, A. L. Pearson, D. Yager, M. A. Legros, and C. A. Larabell. High resolution protein localization using soft X-ray microscopy. *Journal of Microscopy*, 201(3):395–403, 2001.
- [3] Matthias Müller, Tobias Mey, Jürgen Niemeyer, and Klaus Mann. Table-top soft x-ray microscope using laser-induced plasma from a pulsed gas jet. *Optics express*, 22(19):23489–23495, 2014.
- [4] E. Carpene. Ultrafast laser irradiation of metals: Beyond the two-temperature model. *Physical Review B*, 74(2):24301, 2006.
- [5] Koji Sugioka, Michel Meunier, and Alberto Piqué. *Laser precision micro-fabrication*, volume 135 of *Springer series in materials science*. Springer, Berlin, 2010.
- [6] Sergio Musazzi and Umberto Perini, editors. *Laser-induced breakdown spectroscopy: Theory and applications*, volume 182 of *Springer series in optical sciences*. Springer, Berlin, 2014.
- [7] Dietmar Mende and Günther Simon. *Physik: Gleichungen und Tabellen*. Hanser, München, 16., aktualisierte Aufl. edition, 2013.
- [8] Jyotsna Majumdar Dutta and Indranil Manna. *Laser-assisted fabrication of materials*, volume v. 161 of *Springer series in materials science, 0933-033X*. Springer, Heidelberg, 2013.
- [9] S. I. Anisimov and Viktor A. Khokhlov. *Instabilities in laser-matter interaction*. CRC Press, Boca Raton and London, 1995.
- [10] Peter Schaaf, editor. *Laser processing of materials: Fundamentals, applications and developments*, volume 139 of *Springer series in materials science, 0933-033X*. Springer, Berlin and London, 2010.
- [11] Alexander Piel. *Plasma physics: An introduction to laboratory, space, and fusion plasmas*. Springer, Heidelberg, 2010.
- [12] Standard Atomic Weights — Commission on Isotopic Abundances and Atomic Weights, 24.08.2015.

- [13] W. W. Coblenz and W. B. Emerson. The reflecting power of tungsten and stellite. *Journal of the Franklin Institute*, 184(2):307, 1917.
- [14] John Michael Dowden, editor. *The theory of laser materials processing: Heat and mass transfer in modern technology*, volume 119 of *Springer series in materials science, 1860-0832*. Springer and Bristol: Canopus Academic Pub, Dordrecht, 2009.
- [15] Wolfgang Demtröder. *Experimentalphysik 3: Atome, Moleküle und Festkörper*. Springer-Verlag Berlin Heidelberg, Berlin, Heidelberg, 2009.
- [16] Christian Peth, Anton Kalinin, Frank Barkusky, Klaus Mann, J. Peter Toennies, and Lev Yu Rusin. XUV laser-plasma source based on solid Ar filament. *Review of Scientific Instruments*, 78(10):103509, 2007.
- [17] Wolfgang Demtröder. *Experimentalphysik 2*. Springer, Berlin and Heidelberg, 5., überarb. und erw. aufl. edition, 2009.
- [18] Germain Chartier. *Introduction to optics*. Advanced texts in physics. Springer, New York, 2005.
- [19] G. S. Settles. *Schlieren and Shadowgraph Techniques: Visualizing Phenomena in Transparent Media*. Experimental Fluid Mechanics. Springer Berlin Heidelberg, Berlin, Heidelberg, 2001.
- [20] Pradipta Kumar Panigrahi and Krishnamurthy Muralidhar. *Schlieren and shadowgraph methods in heat and mass transfer*. SpringerBriefs in applied sciences and technology, Thermal engineering and applied science, 2191-530X. Springer, New York, NY, 2012.
- [21] Johannes Franz Hartmann. Bemerkungen über den Bau und die Justirung von Spektrographen. *Zeitschrift für Instrumentenkunde*, 20:17–27,47–58, 1900.
- [22] Roland V. Shack and B. C. Platt. Production and use of a lenticular Hartmann screen. In *Journal of the Optical Society of America*, volume 61, page 656, 1971.
- [23] B. Schäfer, M. Lübbecke, and K. Mann. Hartmann-Shack wave front measurements for real time determination of laser beam propagation parameters. *Review of Scientific Instruments*, 77(5):53103, 2006.
- [24] InnoLas Laser: SpitLight DPSS OPO.
- [25] Rüdiger Paschotta. *Encyclopedia of laser physics and technology*. Wiley-VCH, Weinheim, 2008.

- [26] Bahaa E. A. Saleh and Malvin Carl Teich. *Fundamentals of photonics*. Wiley series in pure and applied optics. Wiley, New York, 1991.
- [27] Andreas Fix and Christian Stöckl. Investigations on the beam pointing stability of a pulsed optical parametric oscillator. *Optics Express*, 21(9):10720–10730, 2013.
- [28] Lumera. HYPER RAPID 50 Datasheet. 2014.
- [29] Richard Leach. *Optical measurement of surface topography*. Springer, Berlin and Heidelberg, 2011.
- [30] InnoLas. SpitLight Hybrid Datasheet. 2014.
- [31] Przemyslaw W. Wachulak, Marcin Skorupka, Andrzej Bartnik, Jerzy Kostecki, Roman Jarocki, Mirosław Szczurek, Lukasz Wegrzynski, Tomasz Fok, and Henryk Fiedorowicz. Water-window microscopy using compact, laser-plasma source based on Ar/He double stream gas-puff target. In Libor Juha, Saša Bajt, Richard London, René Hudec, and Ladislav Pina, editors, *SPIE Optics + Optoelectronics*, SPIE Proceedings, page 877719. SPIE, 2013.
- [32] B. L. Henke, E. M. Gullikson, and J. C. Davis. X-Ray Interactions: Photoabsorption, Scattering, Transmission, and Reflection at $E = 50$ – $30,000$ eV, $Z = 1$ – 92 . *Atomic Data and Nuclear Data Tables*, 54(2):181–342, 1993.
- [33] Matthias Müller, Frank-Christian Kühnl, Peter Großmann, Pavel Vrba, and Klaus Mann. Emission properties of ns and ps laser-induced soft x-ray sources using pulsed gas jets. *Optics express*, 21(10):12831–12842, 2013.
- [34] Stefan Rung, Johannes Barth, and Ralf Hellmann. Characterization of Laser Beam Shaping Optics Based on Their Ablation Geometry of Thin Films. *Micromachines*, 5(4):943–953, 2014.
- [35] M. R. H. Knowles, G. Rutterford, D. Karnakis, and A. Ferguson. Micro-machining of metals, ceramics and polymers using nanosecond lasers. *The International Journal of Advanced Manufacturing Technology*, 33(1-2):95–102, 2007.
- [36] S. Döring, S. Richter, A. Tünnermann, and S. Nolte. Evolution of hole depth and shape in ultrashort pulse deep drilling in silicon. *Applied Physics A*, 105(1):69–74, 2011.
- [37] Sony. ICX285AL Datasheet.

A Appendix

A.1 Sony ICX285AL

Since the above mentioned chip was used for a large portion of the measurements, some characteristics shall be given within the following.

SONY

ICX285AL

Diagonal 11 mm (Type 2/3) Progressive Scan CCD Image Sensor with Square Pixel for B/W Cameras

Description

The ICX285AL is a diagonal 11 mm (Type 2/3) interline CCD solid-state image sensor with a square pixel array. High sensitivity and low smear are achieved through the adoption of EXview HAD CCD technology. Progressive scan allows all pixel's signals to be output independently within approximately 1/15 second. Also, the adoption of high frame rate readout mode supports 60 frames per second. This chip features an electronic shutter with variable charge-storage time which makes it possible to realize full-frame still images without a mechanical shutter.

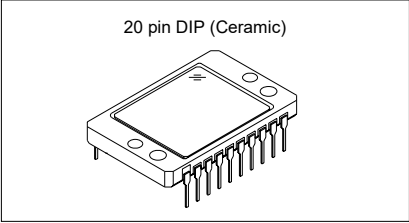
This chip is suitable for image input applications such as still cameras which require high resolution, etc.

Features

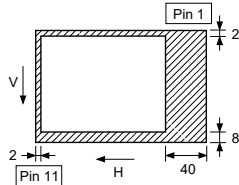
- Progressive scan allows individual readout of the image signals from all pixels.
- High horizontal and vertical resolution (both approximately 1024 TV-lines) still images without a mechanical shutter
- Supports high frame rate readout mode (effective 256 lines output, 60 frame/s)
- Square pixel
- Aspect ratio: 4:3
- Horizontal drive frequency: 28.64 MHz
- High sensitivity, low smear
- Low dark current, excellent anti-blooming characteristics
- Continuous variable-speed shutter
- Horizontal register: 5.0 V drive

Device Structure

- Interline CCD image sensor
- Image size: Diagonal 11 mm (Type 2/3)
- Total number of pixels: 1434 (H) × 1050 (V) approx. 1.50M pixels
- Number of effective pixels: 1392 (H) × 1040 (V) approx. 1.45M pixels
- Number of active pixels: 1360 (H) × 1024 (V) approx. 1.40M pixels
- Chip size: 10.2 mm (H) × 8.3 mm (V)
- Unit cell size: 6.45 μm (H) × 6.45 μm (V)
- Optical black:
 - Horizontal (H) direction: Front 2 pixels, rear 40 pixels
 - Vertical (V) direction: Front 8 pixels, rear 2 pixels
- Number of dummy bits:
 - Horizontal 20
 - Vertical 3
- Substrate material: Silicon



20 pin DIP (Ceramic)



**Optical black position
(Top View)**

EXview HAD CCD™

* EXview HAD CCD is a trademark of Sony Corporation.
EXview HAD CCD is a CCD that drastically improves light efficiency by including near infrared light region as a basic structure of HAD (Hole-Accumulation-Diode) sensor.

Sony reserves the right to change products and specifications without prior notice. This information does not convey any license by any implication or otherwise under any patents or other right. Application circuits shown, if any, are typical examples illustrating the operation of the devices. Sony cannot assume responsibility for any problems arising out of the use of these circuits.

Figure A.1: data sheet of ICX285AL, from [37]

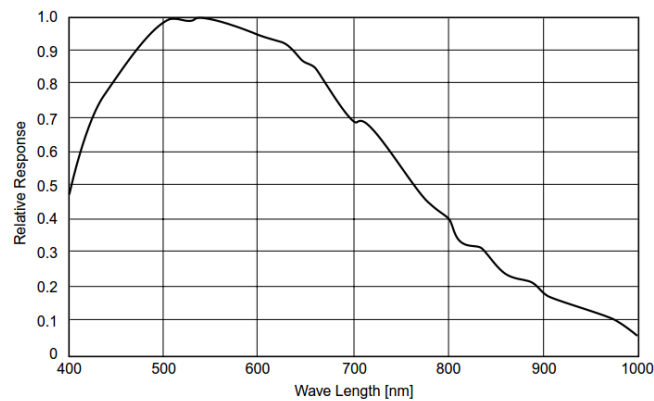
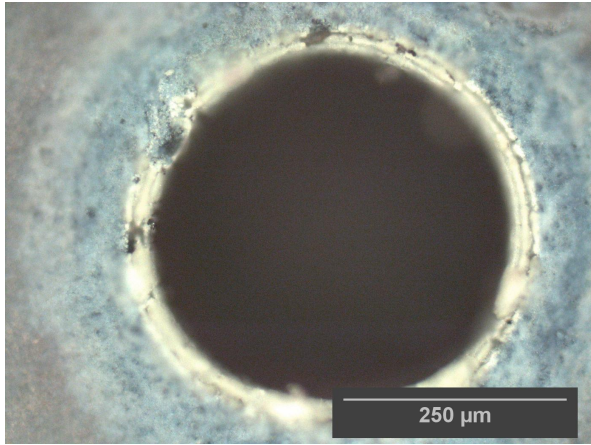


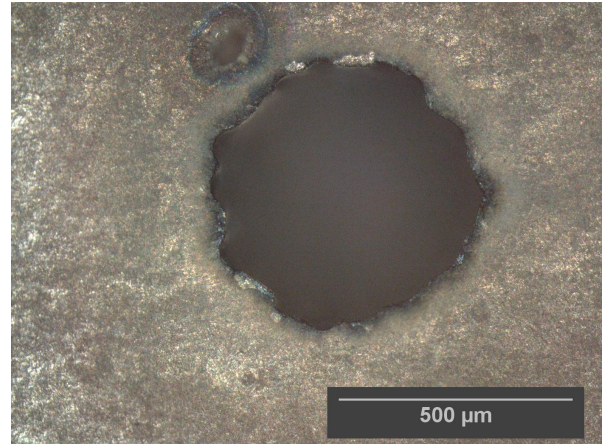
Figure A.2: spectral sensitivity of ICX285AL, from [37]

A.2 Nozzle Data

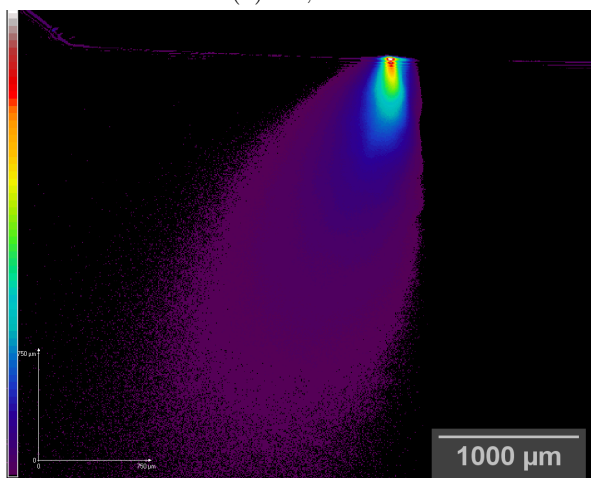
In this chapter, the measured nozzle data presented in the overview in figure 4.15 are displayed larger to enable closer inspection. The full data set also comprising the wavefront deformations is included on the data disk. The plasma profiles contain colors that represent the corresponding CCD count, where blue is associated with the minimum and red with the maximum value.



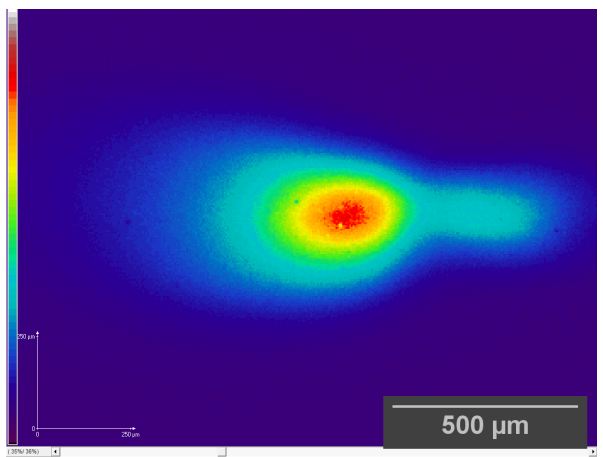
(a) FS, 20x



(b) BS, 10x



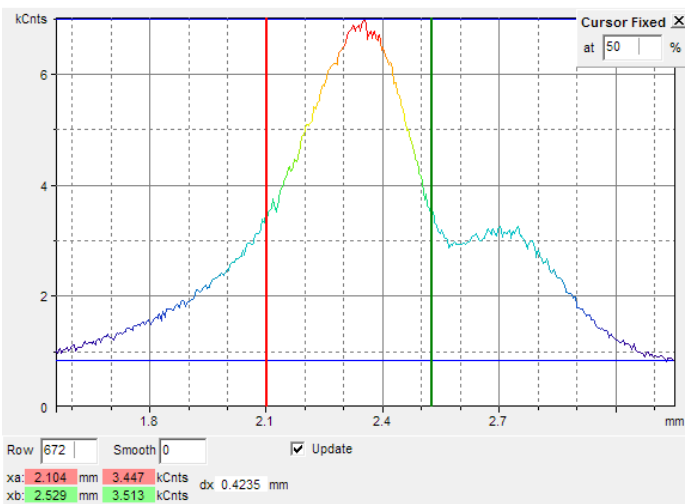
(c) Schlieren, intensified with 2



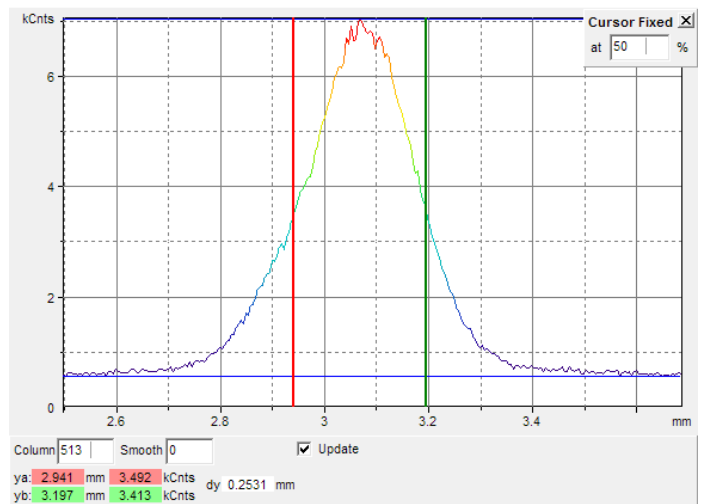
(d) plasma, intensified with 8

Horizontal Cross Section

Vertical Cross Section

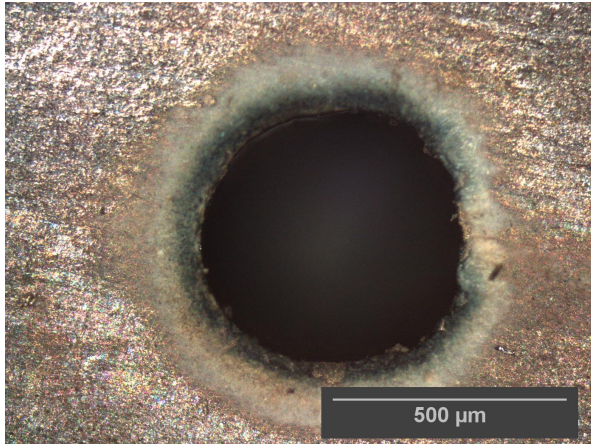


(e) horizontal plasma profile

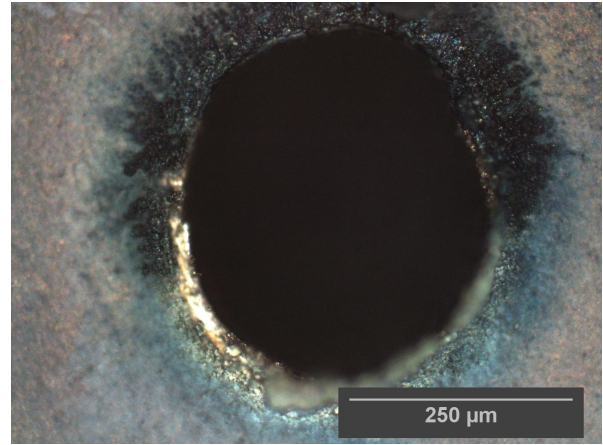


(f) vertical plasma profile

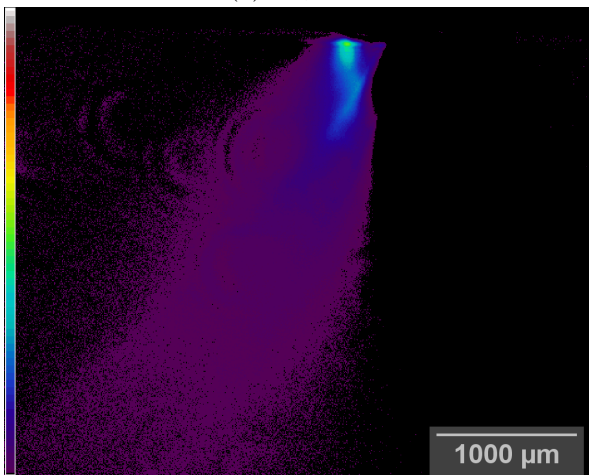
Figure A.3: nozzle (i)



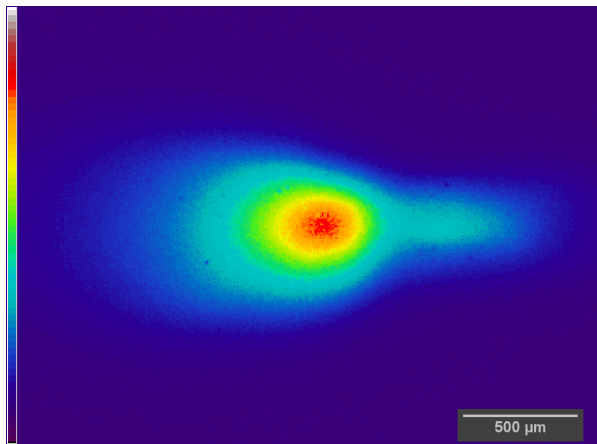
(a) FS, 10x



(b) BS, 20x



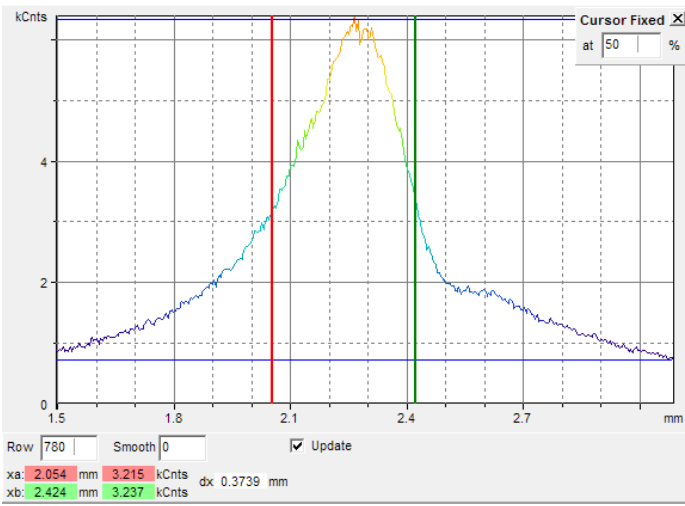
(c) Schlieren, intensified with 2



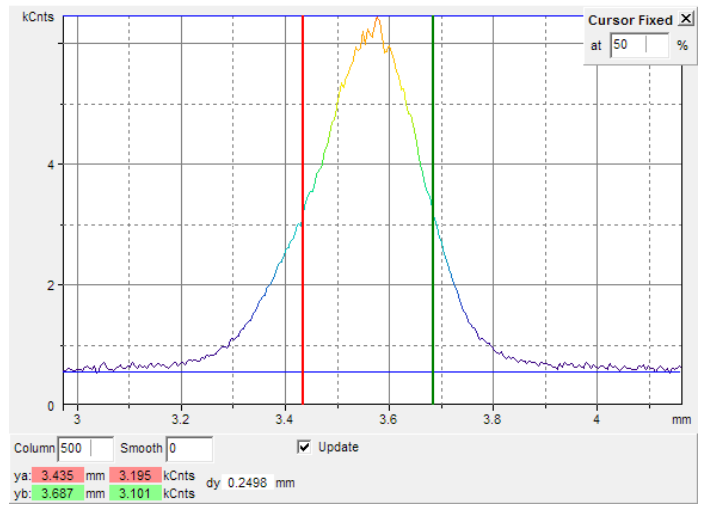
(d) plasma, intensified with 8

Horizontal Cross Section

Vertical Cross Section

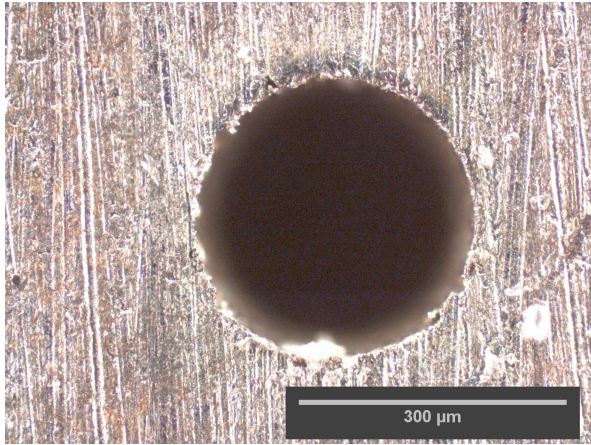


(e) horizontal plasma profile

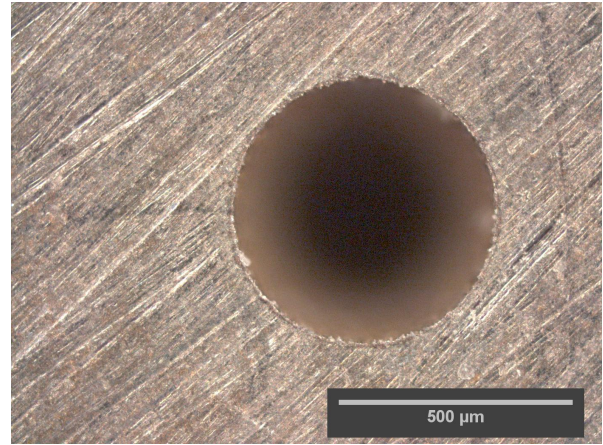


(f) vertical plasma profile

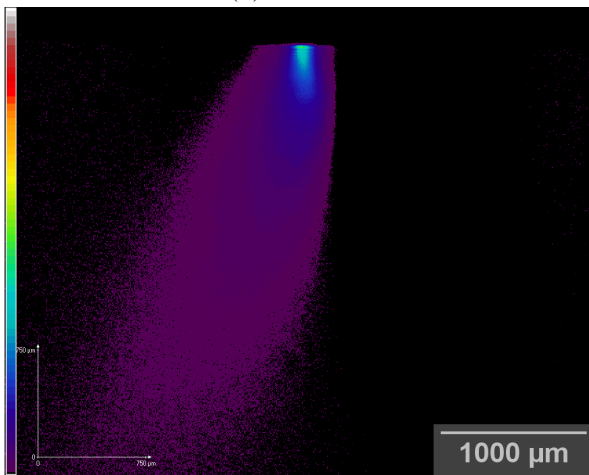
Figure A.4: nozzle (ii)



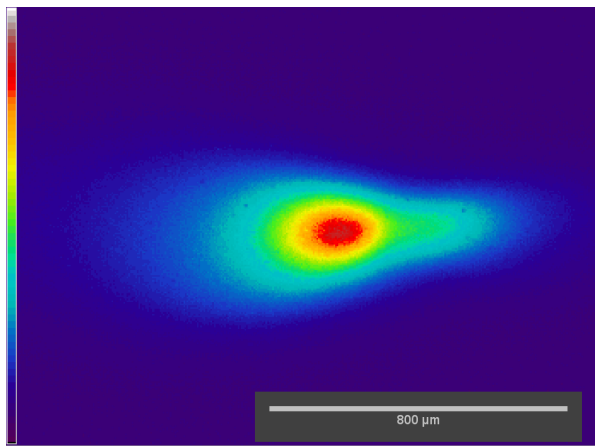
(a) FS, 20x



(b) BS, 10x



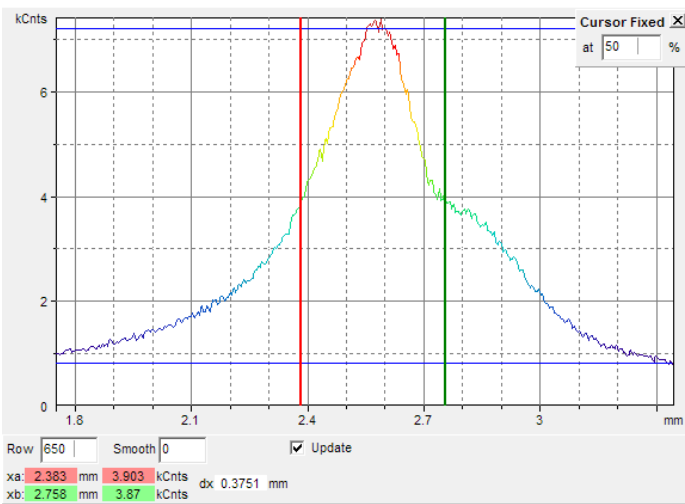
(c) Schlieren, intensified with 2



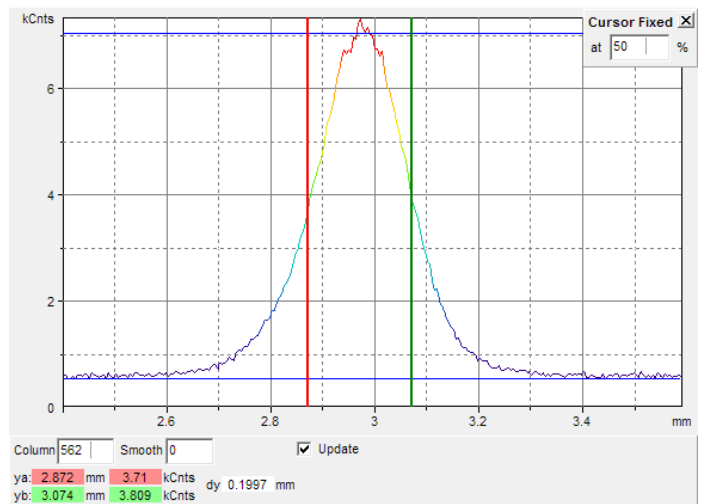
(d) plasma, intensified with 8

Horizontal Cross Section

Vertical Cross Section

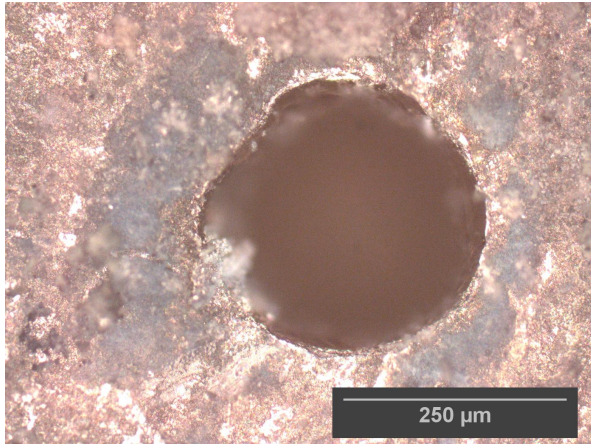


(e) horizontal plasma profile

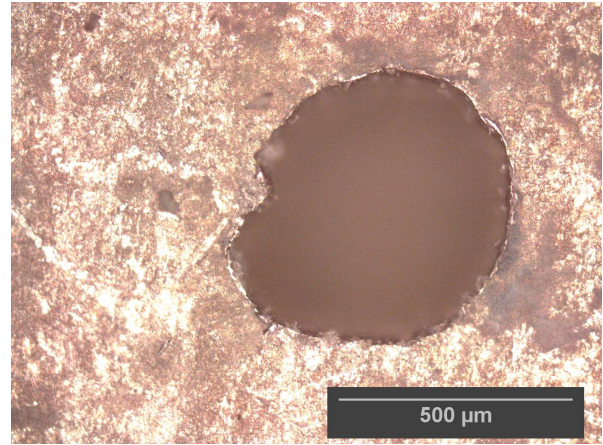


(f) vertical plasma profile

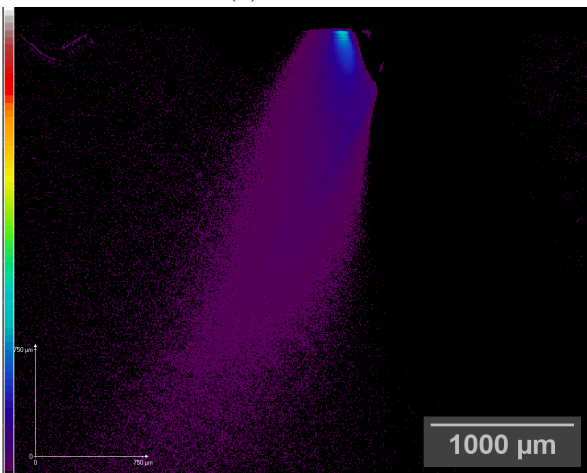
Figure A.5: nozzle (iii)



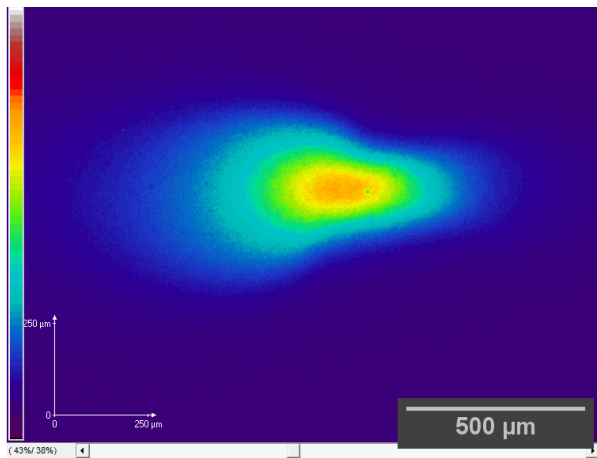
(a) FS, 20x



(b) BS, 10x



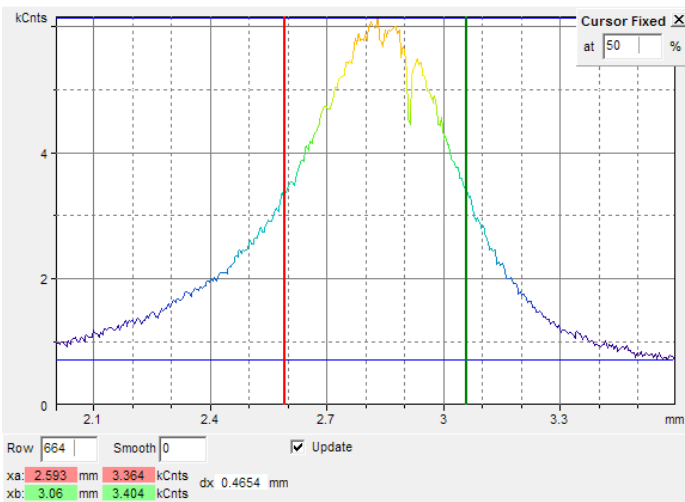
(c) Schlieren, intensified with 2



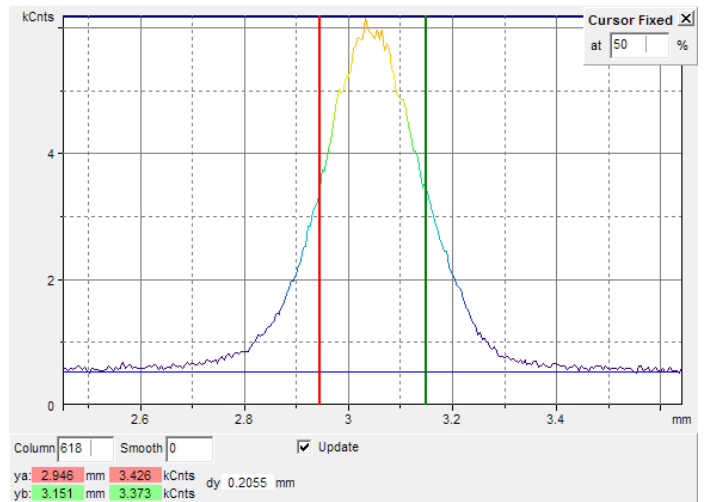
(d) plasma, intensified with 8

Horizontal Cross Section

Vertical Cross Section

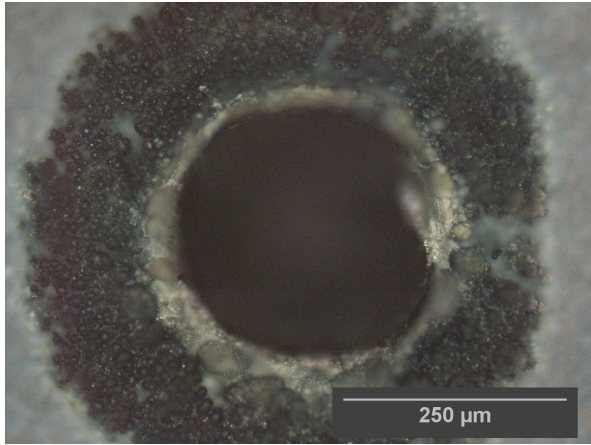


(e) horizontal plasma profile

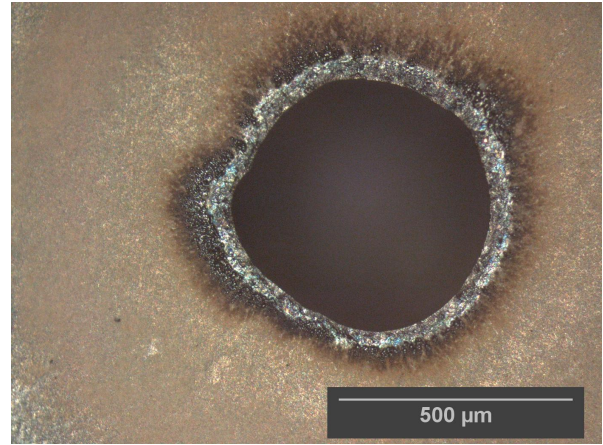


(f) vertical plasma profile

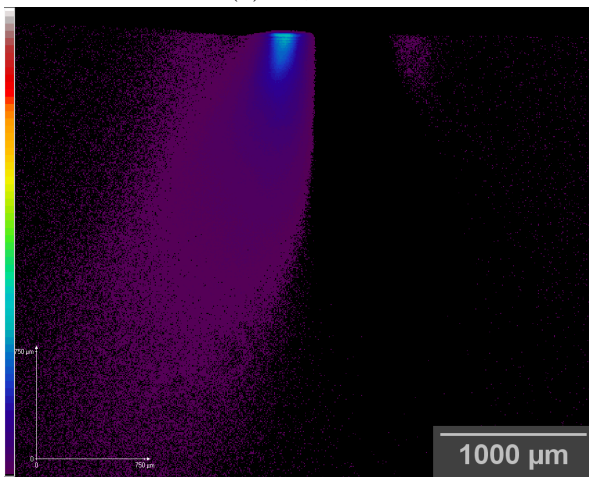
Figure A.6: nozzle (iv)



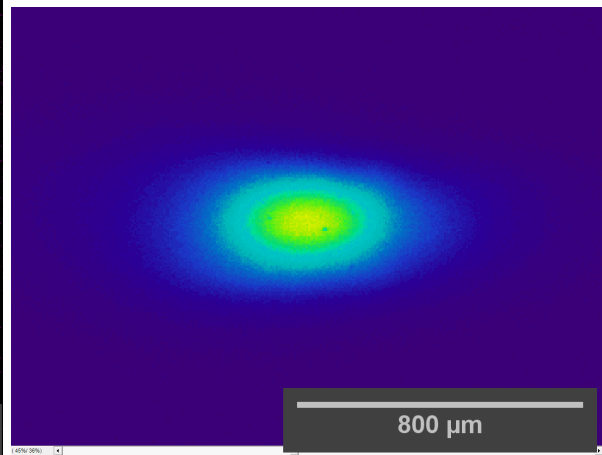
(a) FS, 20x



(b) BS, 10x



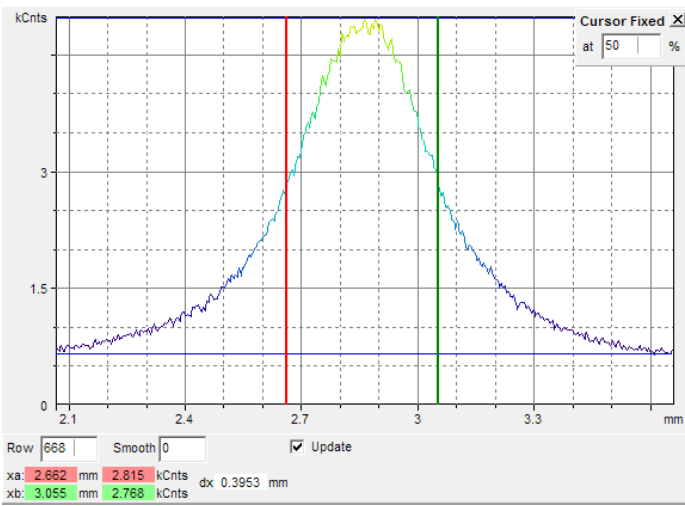
(c) Schlieren, intensified with 2



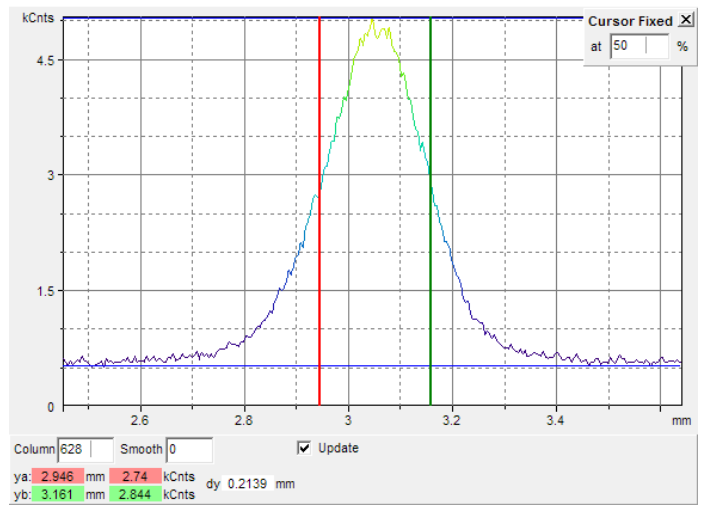
(d) plasma, intensified with 8

Horizontal Cross Section

Vertical Cross Section

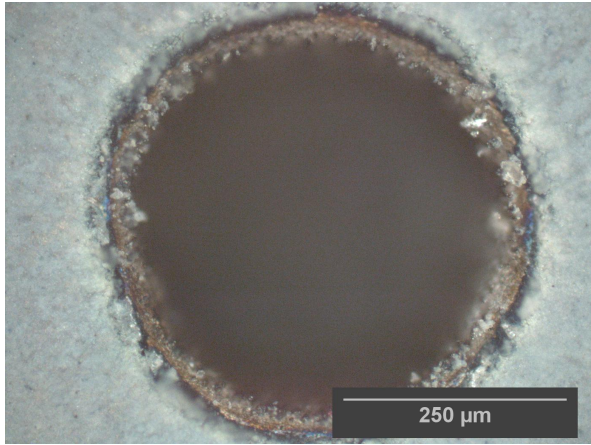


(e) horizontal plasma profile

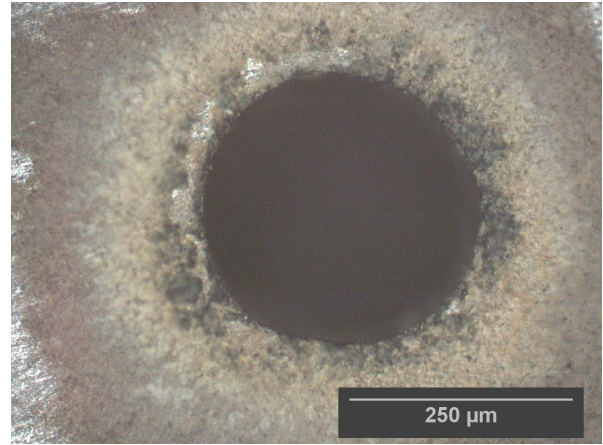


(f) vertical plasma profile

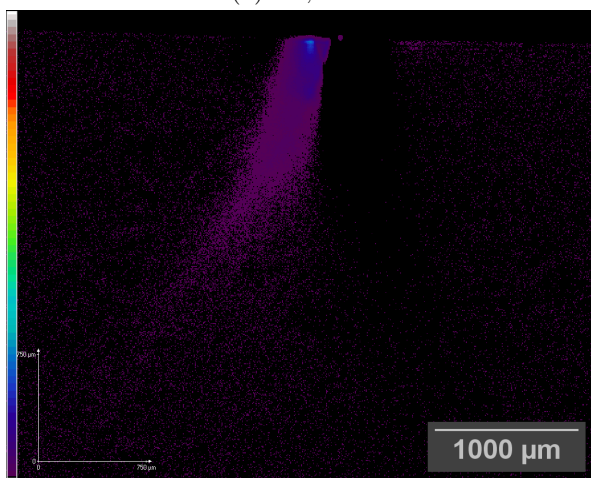
Figure A.7: nozzle (v)



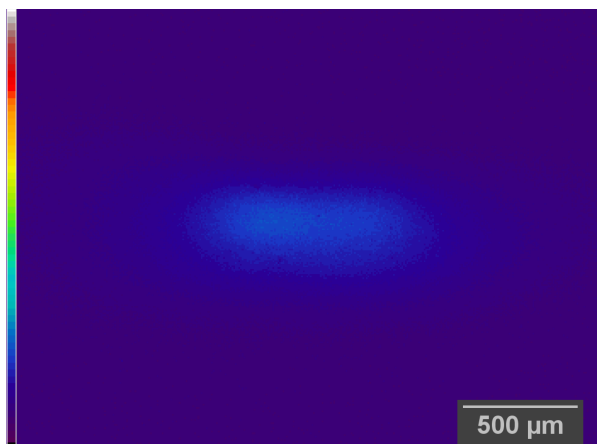
(a) FS, 20x



(b) BS, 20x



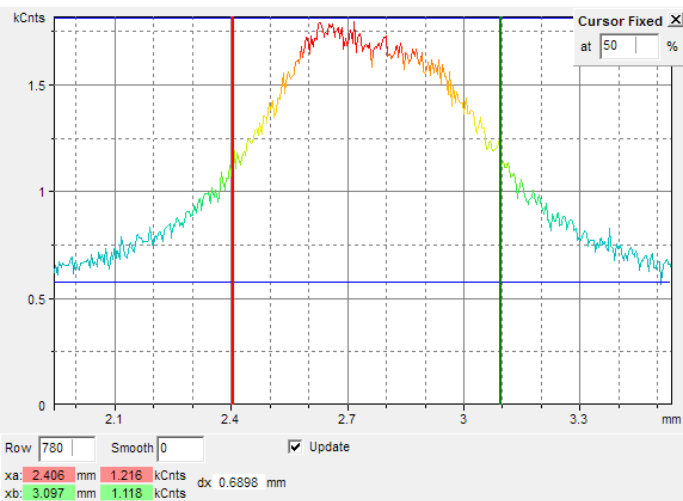
(c) Schlieren, intensified with 2



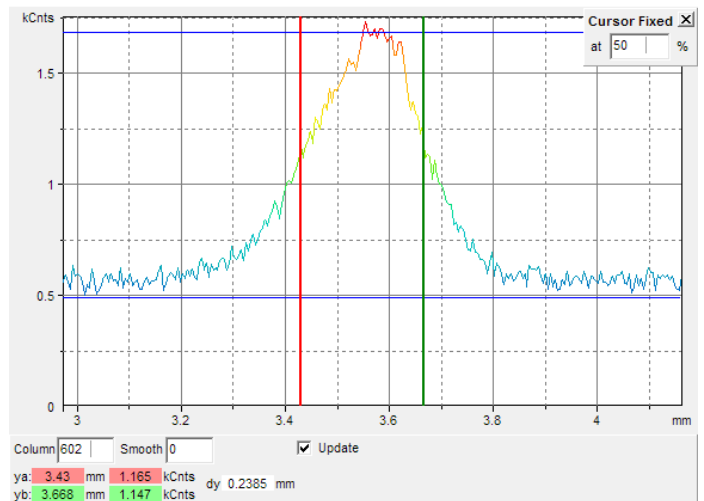
(d) plasma, intensified with 8

Horizontal Cross Section

Vertical Cross Section

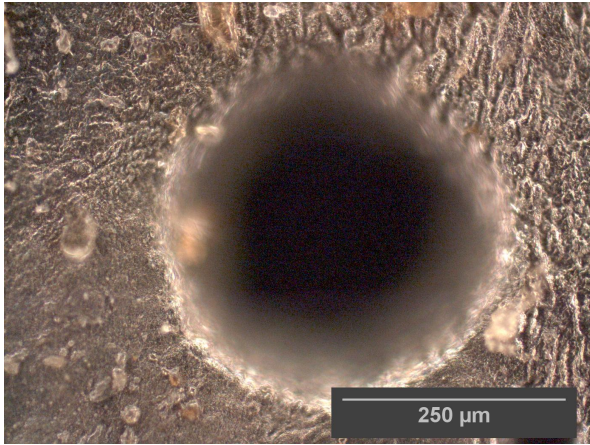


(e) horizontal plasma profile

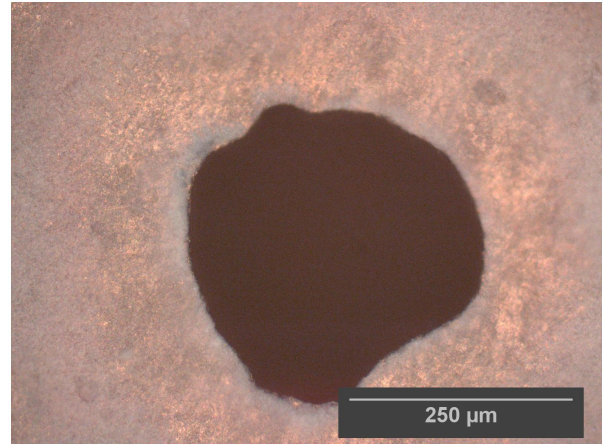


(f) vertical plasma profile

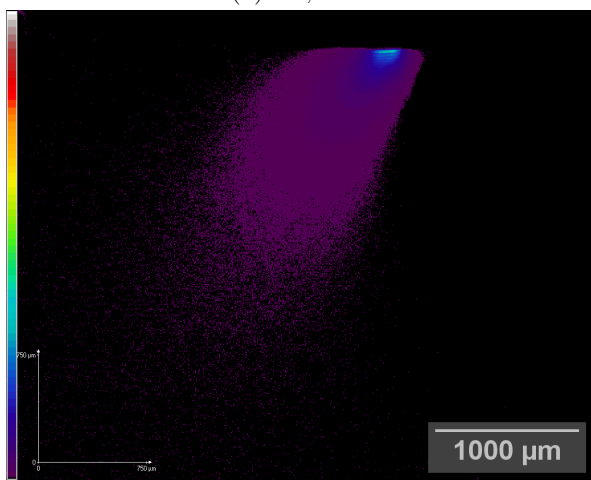
Figure A.8: nozzle (vi)



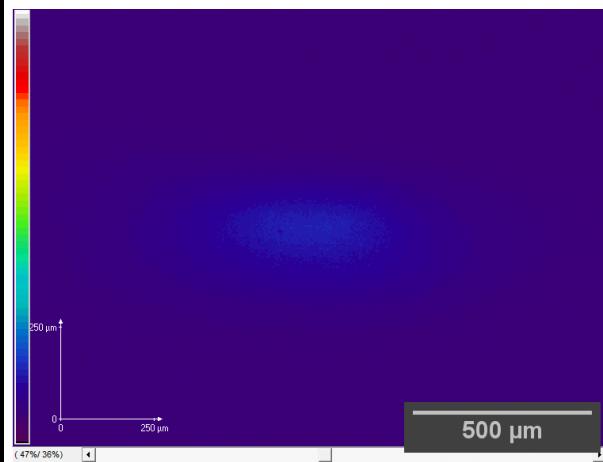
(a) FS, 20x



(b) BS, 20x



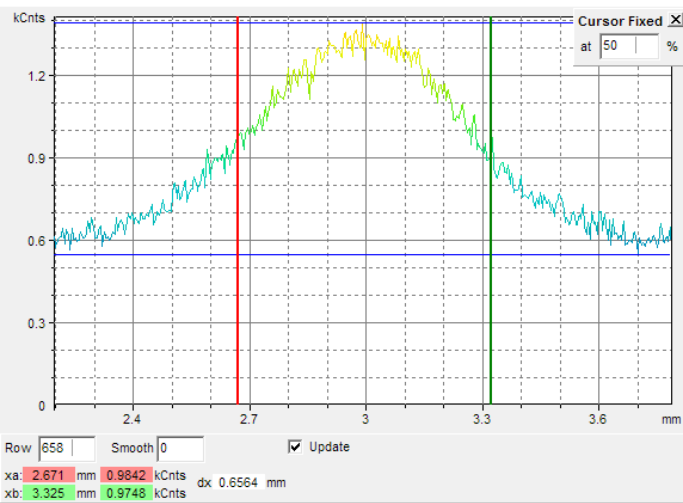
(c) Schlieren, intensified with 2



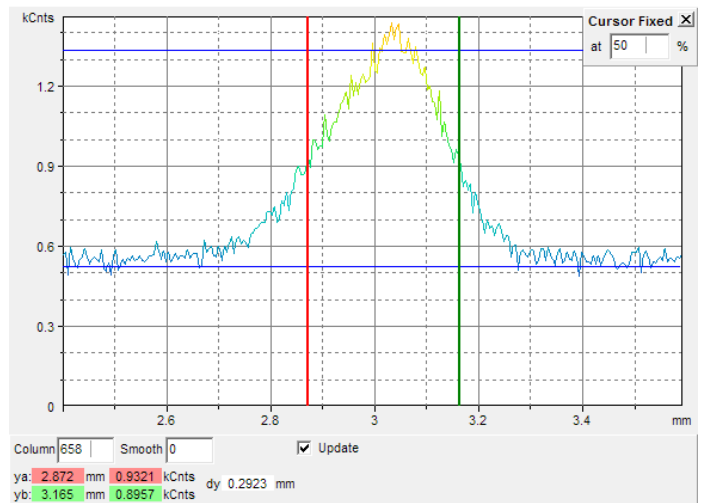
(d) plasma, intensified with 8

Horizontal Cross Section

Vertical Cross Section



(e) horizontal plasma profile



(f) vertical plasma profile

Figure A.9: nozzle (vii)

A.3 Setup Photographs

To give the reader an idea of what the setups discussed in the main part actually look like, the current chapter presents photographs of the lab work at different states of progression.

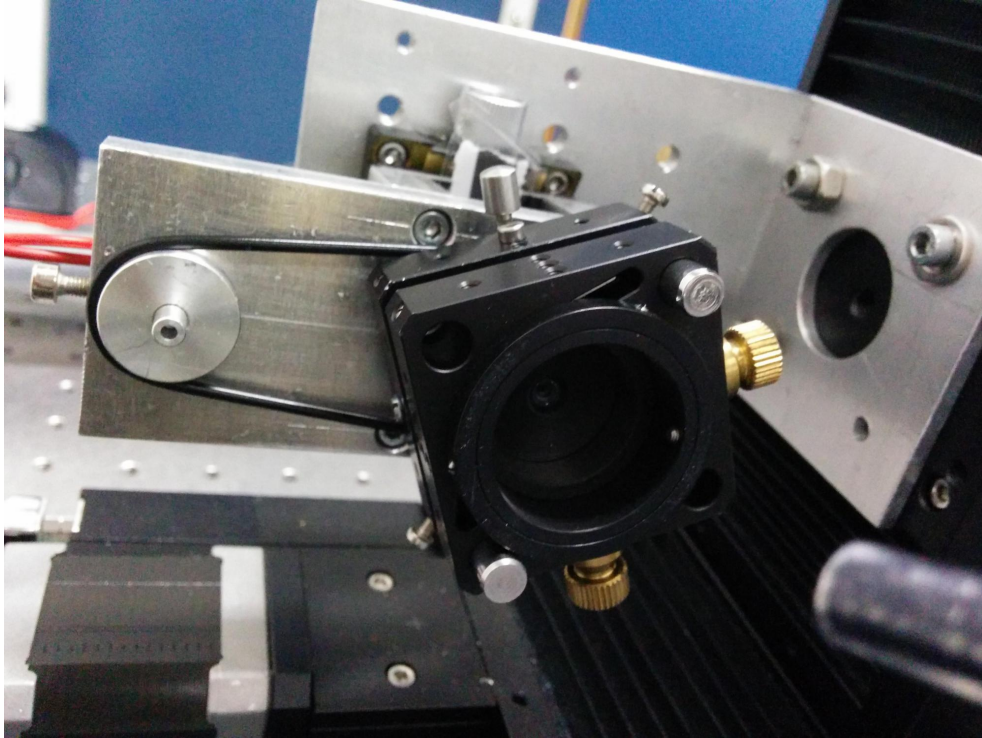


Figure A.10: device used to mount and rotate the workpiece (early stage) which is adhered to a pinhole; small DC motor on the left side, goniometer table in the background

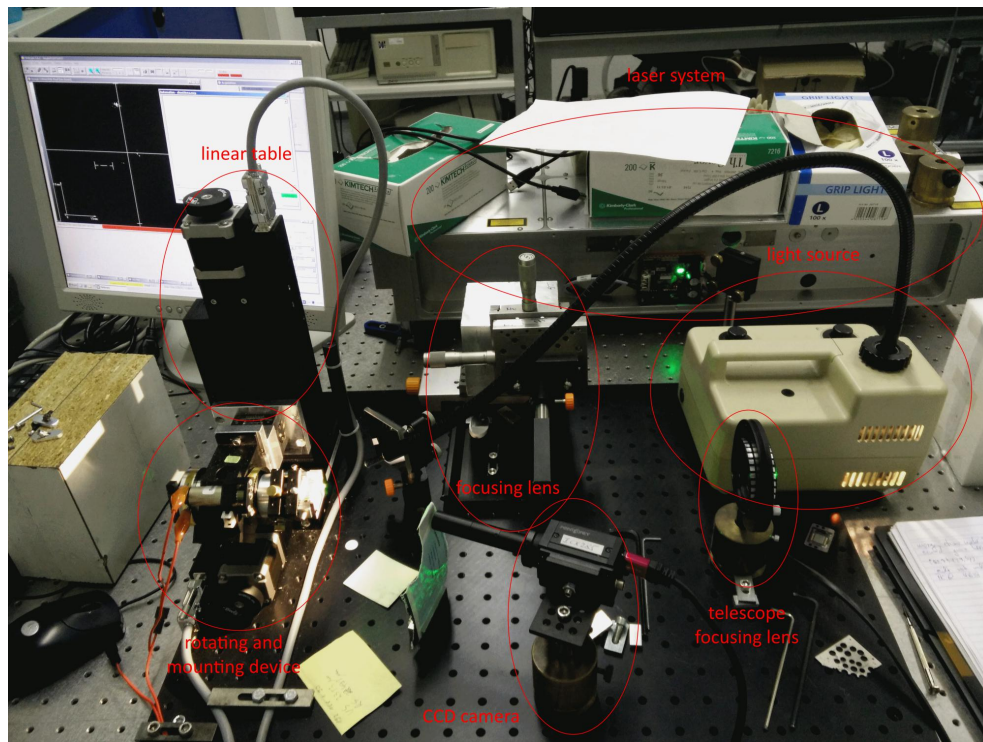


Figure A.11: photo of the trepanning setup

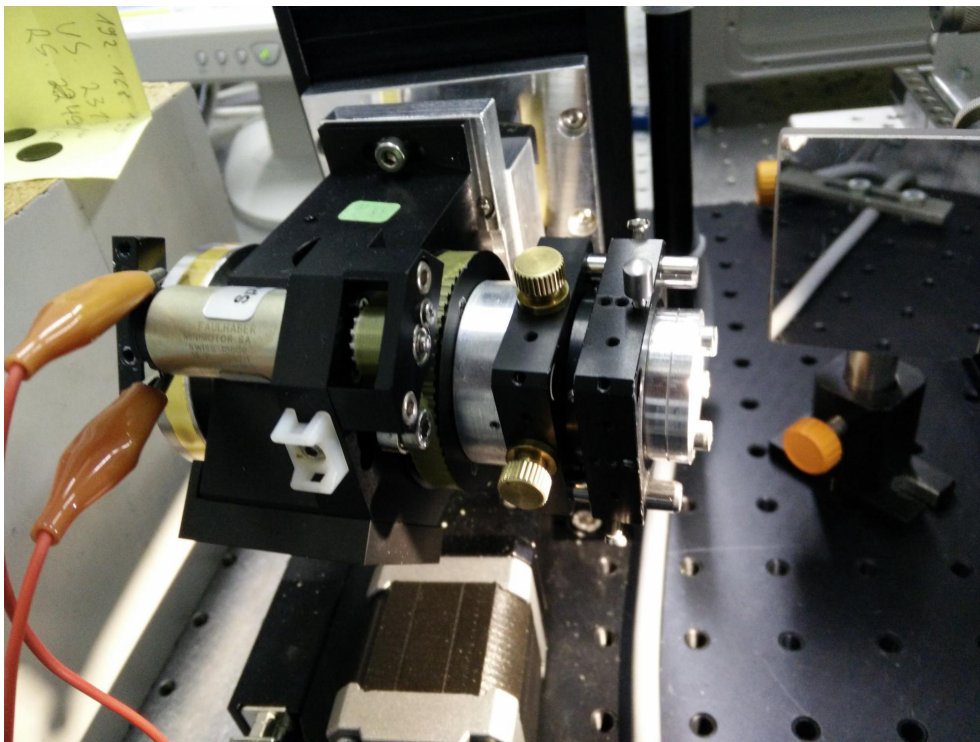


Figure A.12: photo of the improved device used for rotation

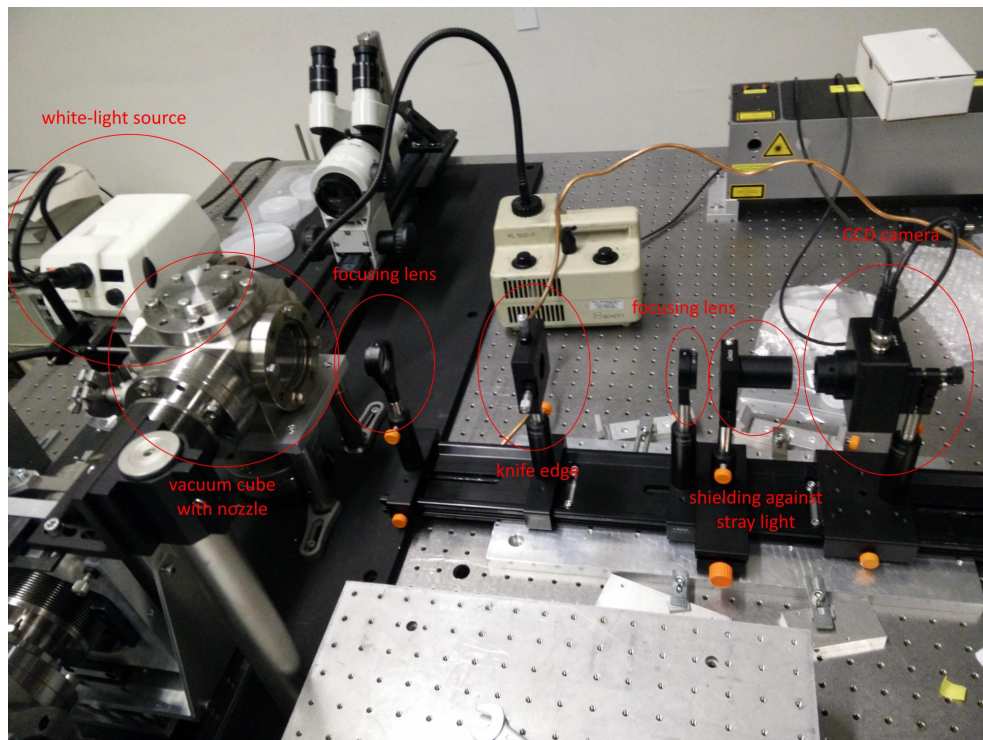


Figure A.13: photo of the setup used for Schlieren images and wavefront distortion measurements; left: white-light source and vacuum chamber; center: 4f-correlator

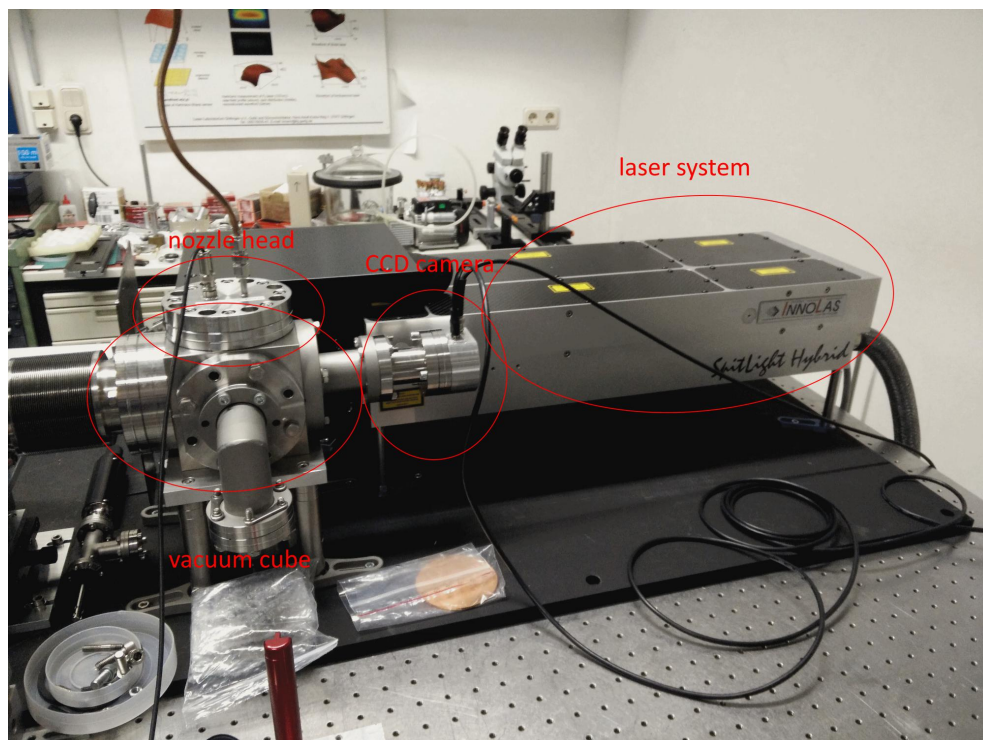


Figure A.14: photo of the plasma analysis setup

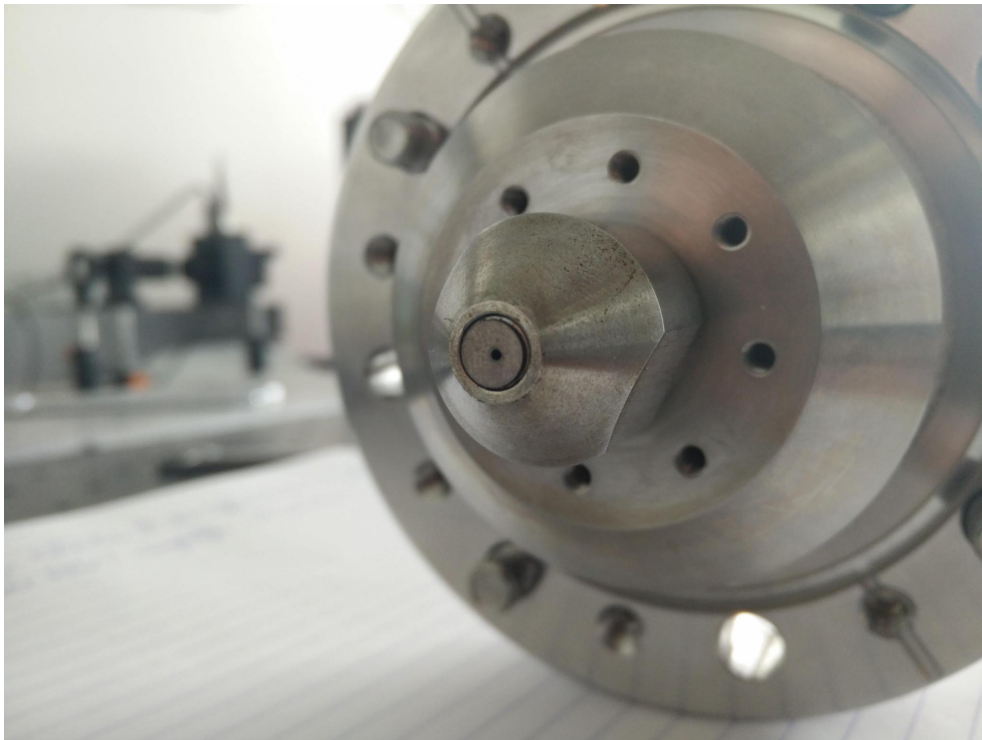


Figure A.15: photo of the nozzle head used for fixing the nozzle plate (using adhesive); implemented in plasma analysis and later experimental setup; nozzle plate is aligned such that holes of both nozzle head and nozzle itself overlap

A.4 Fabricated Part

To enable a reasonable mounting of the rather small workpiece, a holdfast needed to be constructed, which is depicted in figures A.12, A.16 and A.17. The implied requirements include

- (i) no possibility of relative motion between holdfast and workpiece
- (ii) a geometry such that the mounting device fits into the rotating device with play as small as possible
- (iii) the ability to work with plates of different thicknesses
- (iv) the capability of letting radiation pass onto the workpiece even under a large goniometer angle γ

At a late stage of the work it became clear that the constructed device does not fulfill condition (iv) to a satisfying extent, since under goniometer angles $\gamma > 14^\circ$ a fraction of the radiation is blocked, resulting in hole geometries as depicted in figure 3.7. Hence, enabling larger opening angles of the nozzles requires a modification of said mounting device.

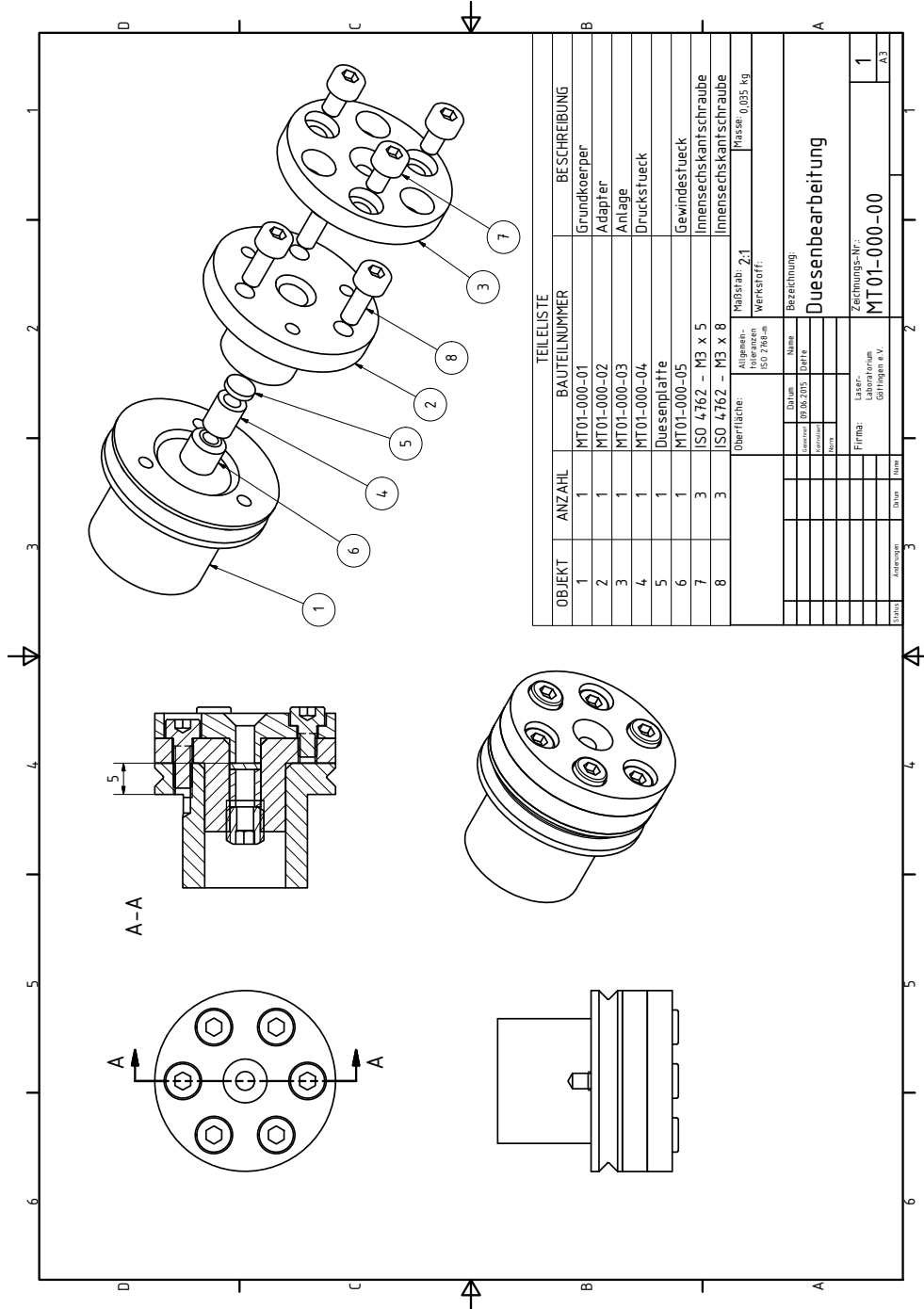


Figure A.16: sketch of device for mounting the wolfram plates

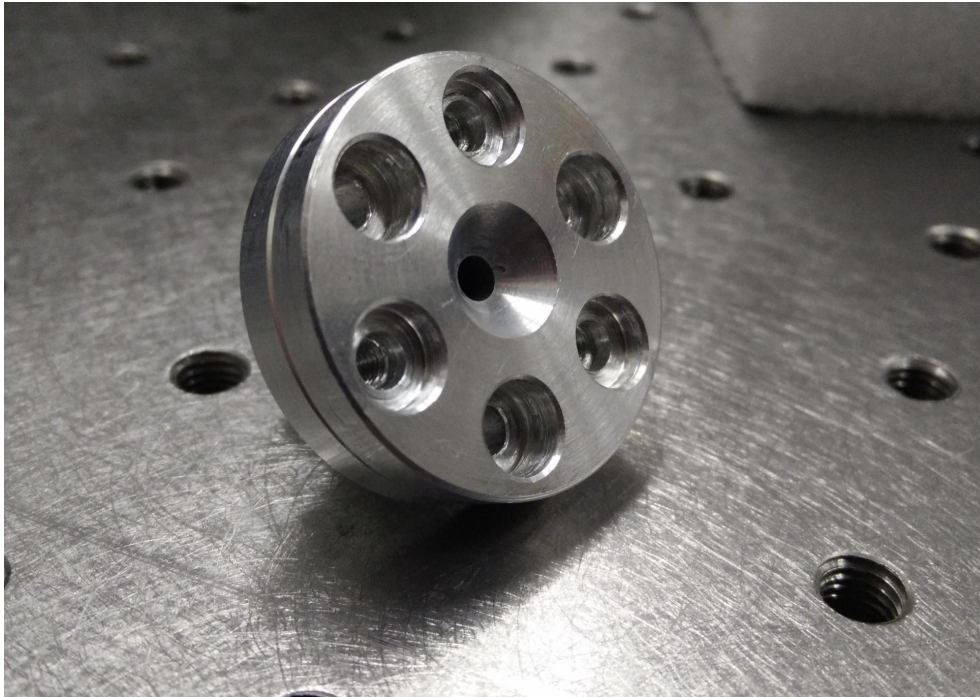


Figure A.17: photo of device for mounting the wolfram plates

A.5 Statement of Authorship

Hiermit versichere ich, dass ich diese Arbeit selbständig verfasst und keine anderen als die angegebenen Quellen und Hilfsmittel benutzt habe. Außerdem versichere ich, dass ich die allgemeinen Prinzipien wissenschaftlicher Arbeit und Veröffentlichung, wie sie in den Leitlinien guter wissenschaftlicher Praxis der Carl von Ossietzky Universität Oldenburg sowie der Hochschule Emden/Leer festgelegt sind, befolgt habe.